

Coolant Solubility of Burnable Neutron Absorbing Material:  
A Thermodynamic Treatment in Support of Advanced CANDU® Reactor Fuel

Solubilité d'un Matériel Absorbeur de Neutrons Brûlable dans le Caloporteur:  
Un Modèle Thermodynamique Utilisé pour le Combustible du Réacteur CANDU®  
Avancé.

A Thesis Submitted

to the Division of Graduate Studies of the Royal Military College of Canada

by

Adam Steven Blackier  
Second-Lieutenant

In Partial Fulfillment of the Requirements for the Degree of Masters of Applied Science  
in  
Nuclear Engineering

March 2010

©This thesis may be used within the Department of National Defence but copyright for  
open publication remains the property of the author.



Library and Archives  
Canada

Published Heritage  
Branch

395 Wellington Street  
Ottawa ON K1A 0N4  
Canada

Bibliothèque et  
Archives Canada

Direction du  
Patrimoine de l'édition

395, rue Wellington  
Ottawa ON K1A 0N4  
Canada

*Your file* *Votre référence*  
ISBN: 978-0-494-64553-6  
*Our file* *Notre référence*  
ISBN: 978-0-494-64553-6

**NOTICE:**

The author has granted a non-exclusive license allowing Library and Archives Canada to reproduce, publish, archive, preserve, conserve, communicate to the public by telecommunication or on the Internet, loan, distribute and sell theses worldwide, for commercial or non-commercial purposes, in microform, paper, electronic and/or any other formats.

The author retains copyright ownership and moral rights in this thesis. Neither the thesis nor substantial extracts from it may be printed or otherwise reproduced without the author's permission.

---

In compliance with the Canadian Privacy Act some supporting forms may have been removed from this thesis.

While these forms may be included in the document page count, their removal does not represent any loss of content from the thesis.

**AVIS:**

L'auteur a accordé une licence non exclusive permettant à la Bibliothèque et Archives Canada de reproduire, publier, archiver, sauvegarder, conserver, transmettre au public par télécommunication ou par l'Internet, prêter, distribuer et vendre des thèses partout dans le monde, à des fins commerciales ou autres, sur support microforme, papier, électronique et/ou autres formats.

L'auteur conserve la propriété du droit d'auteur et des droits moraux qui protègent cette thèse. Ni la thèse ni des extraits substantiels de celle-ci ne doivent être imprimés ou autrement reproduits sans son autorisation.

---

Conformément à la loi canadienne sur la protection de la vie privée, quelques formulaires secondaires ont été enlevés de cette thèse.

Bien que ces formulaires aient inclus dans la pagination, il n'y aura aucun contenu manquant.

  
**Canada**

## ACKNOWLEDGEMENTS

The completion of this research was made possible by the assistance of many people. I would like to thank my parents Jack and Assunta Blackier as well as my brother Michael for their unwavering support through out my time in the Canadian Forces. I would like to thank my supervisors Dr. William Thompson and Dr. Emily Corcoran for their continued support during my years as an undergraduate as well as giving me the opportunity to continue graduate work under their guidance. I would like to acknowledge the efforts made by many of the technical staff within the chemistry and chemical engineering department as well as the support shown by the Department of National Defence, for giving me the unique opportunity to further my education.

## ABSTRACT

Advanced CANDU<sup>®</sup> Reactors (ACR-1000) are expected to be the next generation of Canadian nuclear power technology. The ACR-1000 will employ a newly designed fuel bundle similar in appearance to those used in current CANDU<sup>®</sup> reactors. Isotopically enriched uranium dioxide fuel and a Burnable Neutron Absorbing (BNA) central element composed of stabilized zirconia ( $ZrO_{2,s}$ ) doped with gadolinia ( $Gd_2O_{3,s}$ ) and dysprosia ( $Dy_2O_{3,s}$ ) will be used. As the BNA material contains elements with high neutron absorption cross sections, there is a safety concern with the possible leaching of these elements into the light water coolant, in the unlikely event of a breach in the Zircaloy sheath.

To address this concern, solubility measurements in water over a range of pH values have been conducted on pure dysprosium and gadolinium oxide to determine the extent of dissolution in relation to the possible presence of complex ions involving OH<sup>-</sup>. Experimentation has led to estimated thermodynamic properties for aqueous ions and complex ions, and revised Pourbaix diagrams and, in general, a framework to connect BNA solubility with other thermochemical fuel treatments. The conclusion is reached that negligible concentrations of dissolved dysprosium and gadolinium species are expected to develop in the alkaline aqueous coolant, characteristic of the ACR-1000.

## RÉSUMÉ

Le réacteur nucléaire avancé CANDU<sup>®</sup> (ACR-1000) représente la prochaine génération de la technologie canadienne en énergie nucléaire. Le réacteur ACR-1000 utilisera une nouvelle grappe de combustible semblable en apparence à celle présentement utilisée pour les réacteurs CANDU<sup>®</sup> actuels. On prévoit utiliser du combustible fait de dioxyde d'uranium enrichi isotopiquement et pourvu d'un élément central contenant un absorbeur de neutrons brûlable fait de dioxyde de zirconium ( $ZrO_{2,s}$ ) stabilisé et dopé avec du gadolinia ( $Gd_2O_{3,s}$ ) et du dysprosia ( $Dy_2O_{3,s}$ ). Comme le matériel absorbeur de neutrons contient des éléments avec des sections efficaces d'absorption de neutrons élevées, il existe une crainte reliée à la sûreté à cause du lessivage possible de ces éléments dans le caloporteur fait d'eau ordinaire, lors de rares occurrences de défaillances de la gaine en Zircaloy.

Afin de répondre à cette crainte, on a effectué des mesures de solubilité dans l'eau pour un domaine de valeurs du pH pour des oxydes purs de dysprosium et de gadolinium pour déterminer l'importance de la dissolution en relation avec la présence possible d'ions complexes impliquant le radical OH<sup>-</sup>. Le programme expérimental a mené à une estimation des propriétés thermodynamiques des ions aqueux et des ions complexes, à la révision de diagrammes de Pourbaix et, de façon plus générale, à une méthodologie permettant de relier la solubilité des absorbeurs de neutrons brûlables avec d'autres traitements thermochimiques du combustible. La conclusion permet d'affirmer que l'on peut s'attendre à n'obtenir que des concentrations négligeables d'espèces de gadolinium

et de dysprosium dissoutes qui pourraient se développer dans le caloporteur aqueux et alcalin typique du réacteur ACR-1000.

# TABLE OF CONTENTS

<b>ACKNOWLEDGEMENTS</b>	<b>iii</b>
<b>ABSTRACT</b>	<b>iv</b>
<b>RÉSUMÉ</b>	<b>v</b>
<b>TABLE OF CONTENTS</b>	<b>vii</b>
<b>LIST OF FIGURES</b>	<b>ix</b>
<b>LIST OF TABLES</b>	<b>xiii</b>
<b>CHAPTER 1 Introduction</b>	<b>1</b>
1.1 Canadian Nuclear Power Production	1
1.2 Fission and CANDU® Reactor Technology	3
1.3 Advanced CANDU® Reactor (ACR-1000)	5
1.3.1 Safety Improvements	5
1.3.2 Economic Improvements	6
1.3.3 ACR-1000 Fuel	7
1.4 Technical Concern	9
1.5 BNA Solubility in Aqueous Solutions	10
1.6 Research Objectives	14
<b>CHAPTER 2 Background Chemistry</b>	<b>15</b>
2.1 General Aqueous Solubility of Dysprosium Oxide	17
2.2 Complex Ions	18
2.3 Thermodynamic Modelling	23
2.3.1 Precision and Accuracy in Recording Thermodynamic Properties	26
2.4 Pourbaix Diagrams	27
<b>CHAPTER 3 Experimental Procedures</b>	<b>34</b>
3.1 Measurement of pH	34
3.2 Determination of Solubility Product	39
3.3 Thermogravimetric Analysis (TGA)	39
3.4 Solubility in Highly Alkaline Solutions	40
<b>CHAPTER 4 Experimental Results</b>	<b>42</b>
4.1 Precipitation Experiments	42
4.2 Thermogravimetric Analysis (TGA) Results	44
4.3 High Alkaline Solubility Results	47
<b>CHAPTER 5 Thermodynamic Modelling of Solubility</b>	<b>52</b>
5.1 Dysprosium Trihydroxide	52
5.2 Dysprosium Monohydrate	60
5.3 Complex Ions	63
5.4 Dysprosia Additions to Pure Water	71
5.5 Computed Pourbaix Diagrams for Dysprosium at 298 K	74
5.6 Solubility Model for Gadolinia	76
<b>CHAPTER 6 Discussion</b>	<b>78</b>
6.1 Behaviour of Zirconia in Aqueous Solution	78
6.2 Temperature Effect on pH Scale	80
6.3 Pourbaix Diagrams Projected to High Temperature	83
6.4 Coexistence of Dysprosium and Gadolinium	86
<b>CHAPTER 7 Summary and Conclusion</b>	<b>94</b>

<b>CHAPTER 8 Recommendations</b>	<b>96</b>
<b>REFERENCES</b>	<b>97</b>
<b>APPENDICES</b>	<b>101</b>
<b>APPENDIX A. Dysprosium Oxide (Dy<sub>2</sub>O<sub>3</sub>) Particle Size</b>	<b>102</b>
<b>APPENDIX B. Neutron Activation Analysis Reports</b>	<b>104</b>
<b>APPENDIX C. Solubility Product Calculation for Dysprosium Hydroxide</b>	<b>106</b>
<b>APPENDIX D. Modeled TGA Solid Dy Precipitate Phase Boundary</b>	<b>108</b>
<b>APPENDIX E. Gadolinium Solubility Product Sample Calculation</b>	<b>109</b>
<b>APPENDIX F. Thermodynamic Computations of Gadolinium</b>	<b>111</b>
<b>APPENDIX G. Thermodynamic Data of Species</b>	<b>112</b>
<b>CURRICULUM VITAE</b>	<b>119</b>



## LIST OF FIGURES

Figure 1.	Contribution to electrical energy production in Canada for 2007. Total electricity generated in 2007 was 613 billion kWh .	2
Figure 2.	Nuclear fission of Uranium-235.	3
Figure 3.	Schematic of a conventional CANDU <sup>®</sup> power generation plant currently in operation [10].	4
Figure 4.	Approximate lattice pitch and size comparison of ACR-1000 with other CANDU <sup>®</sup> Reactors [9].	7
Figure 5.	Cross sectional view of ACR-1000 CANFLEX fuel bundle [9,12].	8
Figure 6.	Neutron absorption and Beta ( $\beta^-$ ) decay.	9
Figure 7.	Periodic table. Elements involved in the Burnable Neutron Absorbing central element of the ACR-1000 fuel bundle are indicated in solid blue. The Lanthanide series of elements are outlined in dashed red.	15
Figure 8.	Ionic radii of lanthanide (Rare Earth) trivalent ions given in relation to the comparable radii of trivalent yttrium and tetravalent zirconium ions.	16
Figure 9.	Solubility of $Dy(OH)_3$ as influenced by changes in pH. The vertical scale is the logarithm of the molality of dissolved dysprosium.	22
Figure 10.	Pourbaix diagram of the europium – water system from the Atlas of Electrochemical Equilibria in Aqueous Solutions [18].	28
Figure 11.	General Pourbaix diagram of water.	31
Figure 12.	Pourbaix diagram of dysprosium – water (A) and gadolinium – water (B) from the Atlas of Electrochemical Equilibria in Aqueous Solutions [18].	32
Figure 13.	Experimental Setup to measure pH using a $Pt / H_2g$ and SCE.	38
Figure 14.	Precipitation of $Dy(OH)_3$ providing data to determine the solubility product.	42
Figure 15.	Precipitation of $Gd(OH)_3$ providing data to determine the solubility product.	43
Figure 16.	$Dy(OH)_3$ dehydration profile.	45

Figure 17.	$Gd(OH)_3$ dehydration profile.	47
Figure 18.	Measurements of pH in Lithium hydroxide solution at 21°C.	49
Figure 19.	Measured concentrations (molality) of dissolved dysprosium in highly alkaline solutions. Sloped line is the expectation when $Dy(OH)_3$ dissociates to $Dy_{aq}^{3+}$ and $OH$ .	51
Figure 20.	Gibbs energy minimization computation at 297.15 K for a value of $\alpha = 0.033$ offered as evidence that the thermodynamic properties introduced for $Dy(OH)_3$ replicate the measurements recorded in Figure 23.	56
Figure 21.	Gibbs energy minimization computation at 297.15 K for a value of $\alpha = 0.034$ offered as evidence that the thermodynamic properties introduced for $Dy(OH)_3$ replicate the measurements recorded in Figure 23.	58
Figure 22.	Gibbs energy minimization computation at 297.15 K for a value of $\alpha = 0.038$ offered as evidence that the thermodynamic properties introduced for $Dy(OH)_3$ replicate the measurements recorded in Figure 23.	59
Figure 23.	Modelling comparison to solubility product experiment offered as evidence in support of the thermodynamic properties for dysprosium hydroxide given in Table 6.	60
Figure 24.	Proposed phase diagram for the stability of dysprosium oxide hydrates qualitatively consistent with thermogravimetric experiments.	62
Figure 25.	First attempt at modelling solubility in highly alkaline solutions based upon the estimated thermodynamic properties of complex ions given in Table 9.	66
Figure 26.	Second attempt at modelling solubility in highly alkaline solutions based upon the estimated thermodynamic properties of complex ions given in Table 10.	67
Figure 27.	Final attempt at modelling solubility in highly alkaline solutions based upon the estimated thermodynamic properties of complex ions given in Table 11.	68
Figure 28.	Linear enthalpy trends for final estimations made for complex ions.	69
Figure 29.	Computed equilibrium at 298 K representative of position marked in Figure 27.	70

Figure 30.	Aqueous equilibrium in the supposition that $Dy_2O_{3,s}$ coexists with aqueous solution.	72
Figure 31.	Aqueous equilibrium in the supposition that $DyO(OH)_s$ coexists with aqueous solution.	72
Figure 32.	Aqueous equilibrium in the supposition that $Dy(OH)_3$ coexists with aqueous solution.	73
Figure 33.	Calculated Pourbaix diagram for dysprosium at 298 K, for aqueous concentrations of 1, $10^{-2}$ , $10^{-4}$ , and $10^{-5}$ molal.	75
Figure 34.	Calculated Pourbaix diagram for dysprosium at 298 K, for an aqueous concentration of $10^{-6}$ molal	75
Figure 35.	The Pourbaix diagram for gadolinium at 298 K, for aqueous concentrations of 1, $10^{-2}$ , $10^{-4}$ , and $10^{-5}$ molal.	77
Figure 36.	The Pourbaix diagram for gadolinium at 298 K, for an aqueous concentration of $10^{-6}$ molal.	77
Figure 37.	The Pourbaix diagram for Zr at 298 K, showing aqueous concentrations at 1, $10^{-2}$ , $10^{-4}$ , and $10^{-6}$ molal. The pressure is understood to be sufficient to suppress boiling [19].	79
Figure 38.	The Pourbaix diagram for Zr at 550 K, showing aqueous concentrations at 1, $10^{-2}$ , $10^{-4}$ , and $10^{-6}$ molal. The pressure is understood to be sufficient to suppress boiling [19].	79
Figure 39.	Temperature effect on aqueous solutions. Approximate water partial pressure (atm) shown on right.	81
Figure 40.	Sample calculation depicting the effect of temperature on alkaline lithium hydroxide solution typical of reactor coolant. Points are indicated on Figure 39.	82
Figure 41.	The Pourbaix diagram for dysprosium at 550 K, for aqueous concentrations of 1, $10^{-2}$ , and $10^{-4}$ molal.	83
Figure 42.	The Pourbaix diagram for dysprosium at 550 K, for an aqueous concentration of $10^{-6}$ molal.	84
Figure 43.	The Pourbaix diagram for gadolinium at 550 K, for aqueous concentrations of 1, $10^{-2}$ , and $10^{-4}$ , molal.	85

Figure 44.	The Pourbaix diagram for gadolinium at 550 K, for an aqueous concentration of $10^{-6}$ molal.	85
Figure 45.	Binary phase diagram of zirconia-gadolinia [12].	87
Figure 46.	Binary phase diagram of zirconia-dysprosia [12].	87
Figure 47.	Solubility computation of an arbitrarily chosen BNA composition at 550 K .	90
Figure 48.	Solubility computation of an arbitrarily chosen BNA concentration at 298 K.	91

## LIST OF TABLES

Table 1. Cross sections of elements in the BNA central element [5].	9
Table 2. Typical complex ions or neutral dissolved species involving hydroxide.	19
Table 3. Aqueous species of dysprosium.	20
Table 4. Measurements of pH in concentrated lithium hydroxide solutions.	48
Table 5. Entropy and heat capacity comparison of various solid hydroxides.	54
Table 6. Thermodynamic properties for dysprosium and related species.	55
Table 7. Thermodynamic data for dysprosium oxides and hydrates.	61
Table 8. Comparison of trending entropy as a function of hydroxide group addition.	65
Table 9. First estimate for dysprosium aqueous complex ions.	65
Table 10. Second estimate for dysprosium aqueous complex ions.	67
Table 11. Final estimate for dysprosium aqueous complex ions.	68
Table 12. Final estimate for gadolinium aqueous complex ions and solid phases.	76

## LIST OF SYMBOLS AND ABBREVIATIONS

ACR-1000	Advanced CANDU <sup>®</sup> Reactor
AECL	Atomic Energy of Canada Limited
atm	Atmosphere (unit of pressure)
at %	Atomic percent
BNA	Burnable Neutron Absorber
CANDU <sup>®</sup>	CANada Deuterium Uranium
CANFLEX	CANDU FLEXible fuelling
$C_p$	Heat Capacity
CRL	Chalk River Laboratory
$e^-$	Conceptual electron involved in aqueous equilibria
EMF	Electromotive Force
eV	Electron Volts
G	Gibbs free Energy
H	Enthalpy
ICPMS	Inductively Coupled Plasma Mass Spectrometry
$K_{sp}$	Solubility Product
kWh	Kilowatt Hours
LEU	Low Enriched Uranium
Ln	Collective Symbol for Lanthanide Elements
$Ln(OH)_3$ or $Ln_2O_3 \cdot 3H_2O$	Lanthanide Tri-Hydroxide
$Ln_2O_3$	Lanthanide Sesquioxide
$M_2O_3$	Sesquioxide General Form

MW	Megawatt
MeV	Mega Electron Volt
NAA	Neutron Activation Analysis
PHWR	Pressurized Heavy Water Reactor
S	Entropy
SCE	Saturated Calomel Electrode
SEM	Scanning Electron Microscope
SHE	Standard Hydrogen Electrode
T	Temperature (Absolute, K)
TGA	Thermogravimetric Analysis
XPS	X-Ray Photoelectron Spectroscopy
XRD	X-Ray Diffraction
$\alpha$	Addition of Lithium Hydroxide Solution
$\bar{\nu}$	Antineutrino

## CHAPTER 1 Introduction

In the past half century, the success of Canadian nuclear technology applied to electrical power production, both domestically and abroad, has been achieved using CANDU<sup>®</sup> (CANadian Deuterium Uranium)\* reactors. These reactors employ a design that capitalizes on readily available Canadian natural resources of uranium ore found principally in Saskatchewan [1]. Given the age of the in-service reactors, refurbishment projects have been undertaken to maintain safety and productivity. While refurbishment will allow Canada to address short term needs, an advanced design to meet future domestic electricity requirements is under development. Atomic Energy of Canada Limited (AECL) is well-along in designing the Advanced CANDU<sup>®</sup> Reactor (ACR-1000) that builds on existing CANDU<sup>®</sup> technology and operational experience. It is anticipated that the ACR-1000 will enter service in the next decade, signalling the long awaited resurgence in Canadian nuclear technology.

### 1.1 Canadian Nuclear Power Production

In Canada, nuclear power is generated in Ontario, Quebec and New Brunswick. Future expansion into Alberta is under discussion. The nuclear power reactors in Canada produce approximately fifteen percent of the total electrical generating capability, as illustrated in Figure 1. In Ontario, approximately fifty percent of the electrical energy is generated by CANDU<sup>®</sup> reactors [2].

---

\* CANDU<sup>®</sup> is a registered trademark of Atomic Energy of Canada Limited (AECL)



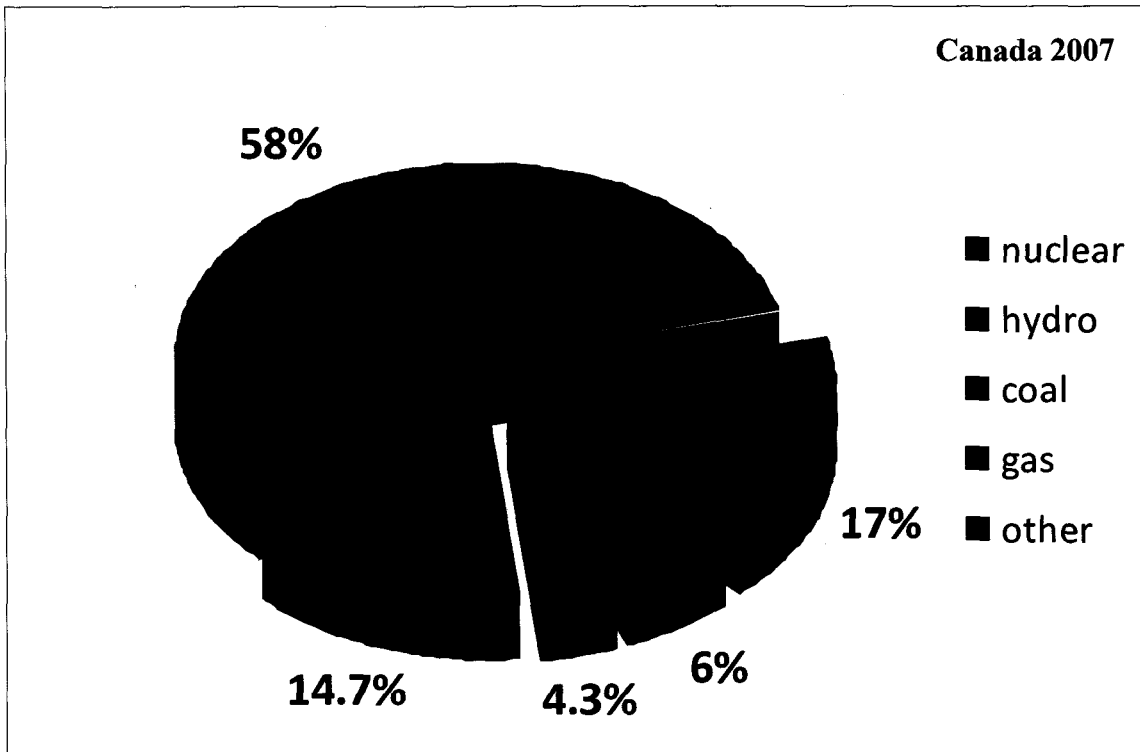


Figure 1. Contribution to electrical energy production in Canada for 2007. Total electricity generated in 2007 was 613 billion kWh [3].

Increased demand for electricity, anticipated from population and economic growth, is projected to create a shortfall of 24,000 MW<sub>e</sub><sup>†</sup> by 2025. This shortfall is equivalent to eighty percent of the current electrical power generation capacity in Ontario [4]. With this concern in mind, and the desire to limit green-house gas emissions, it will be necessary to commission new nuclear power production facilities in support of other energy generating systems (e.g. wind turbines). This would be particularly true if electrically powered motor vehicles were to enter widespread use as the public is expecting.

<sup>†</sup> MW<sub>e</sub> is a term which refers to megawatts of electrical power.

## 1.2 Fission and CANDU<sup>®</sup> Reactor Technology

The CANDU<sup>®</sup> reactor is a Pressurized Heavy Water Reactor (PHWR), which produces electricity by utilizing the heat produced by nuclear fission. The fission process involves neutron bombardment of a fissile nucleus, such as  $^{235}\text{U}$  or  $^{239}\text{Pu}$ . Two fission fragments and 2-3 energetic (fast) neutrons are produced along with approximately 200 MeV of recoverable heat in the form of kinetic energy [5]. The fission process is depicted in Figure 2.

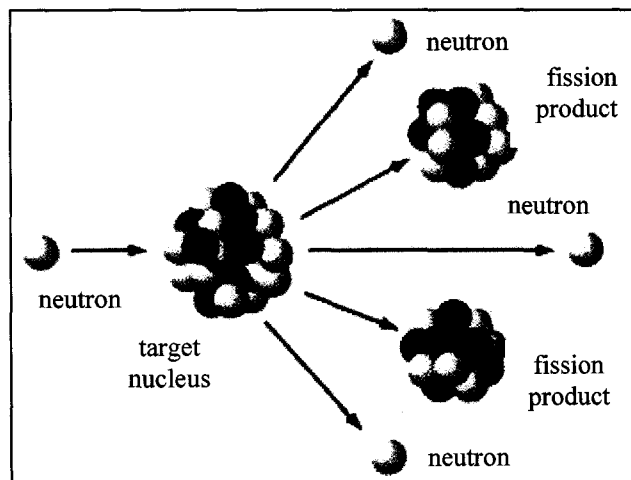


Figure 2. Nuclear fission of Uranium-235 [6].

In-service CANDU reactors use natural uranium dioxide ( $\text{UO}_2$ ) fuel. Natural uranium is composed of 99.3 at%  $^{238}\text{U}$  and 0.7 at%  $^{235}\text{U}$  [7]. Purified  $\text{UO}_2$  is pressed and sintered into cylindrical-shaped pellets. The small percentage of  $^{235}\text{U}$  initially undergoes fission in the reactor environment, producing more neutrons to induce other fission reactions and concurrently transmute  $^{238}\text{U}$  to  $^{239}\text{Pu}$  by neutron absorption and subsequent beta decay.

The sintered  $\text{UO}_2$  pellets are sealed within Zircaloy tubes [8]. These tubes are approximately 0.5 m in length and approximately 1.3 cm in diameter. This constitutes a fuel element in CANDU<sup>®</sup> terminology that is sometimes also described (in other nuclear technologies) as a rod or fuel pin. In CANDU<sup>®</sup> reactors, the fuel elements are combined into groupings of 28, 37 or 43 to create a fuel bundle. Depending on the type of CANDU<sup>®</sup> reactor, 12 or 13 fuel bundles are loaded into horizontal fuel channels [9]. Each fuel channel consists of an inner pressure tube and an outer calandria tube separated by an annular  $\text{CO}_2$ -filled gap. In the conventional CANDU<sup>®</sup> reactor, the pressure tube contains heavy water ( $\text{D}_2\text{O}$ , where  $^2\text{H}\equiv\text{D}$ ) coolant at 9-12 MPa to prevent boiling, as the coolant temperature is typically about  $300^\circ\text{C}$  [9]. The calandria tube separates the pressure tube from the heavy water moderator in the calandria vessel. Figure 3 below depicts a generic CANDU<sup>®</sup> reactor arrangement.

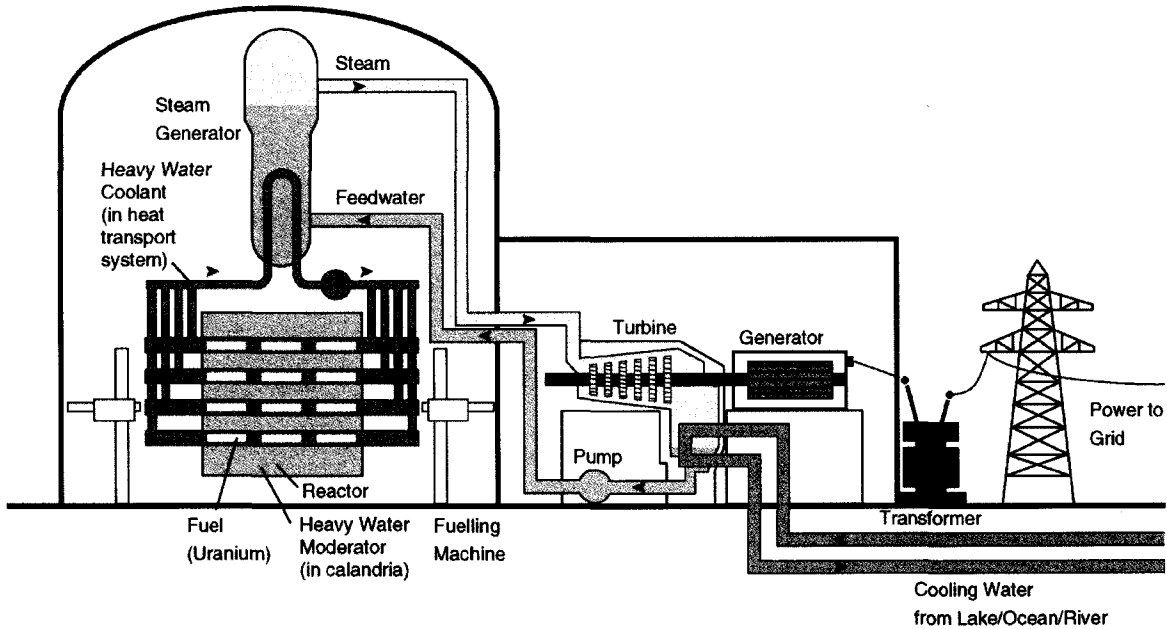


Figure 3. Schematic of a conventional CANDU<sup>®</sup> power generation plant currently in operation [10].

The high pressure heavy water coolant removes the heat produced by the fissioning fuel. The coolant transfers heat to the steam generator. The steam is used to generate electricity using a conventional steam power cycle [10].

### 1.3 Advanced CANDU<sup>®</sup> Reactor (ACR-1000)

The Advanced CANDU<sup>®</sup> Reactor<sup>‡</sup> (ACR-1000) is planned to be the next generation in AECL electrical power reactor designs. The ACR-1000 incorporates the proven strengths of the existing CANDU<sup>®</sup> reactors while improving reactor safety and economics [9].

#### 1.3.1 Safety Improvements

The enhanced safety of the ACR-1000 design is attributed mainly to addressing the positive void coefficient associated with the current design. Void coefficient is a term used to describe the effect on reactivity (and consequent heat generation) caused by voids (or bubbles) in the coolant when the vapour pressure of the coolant exceeds the hydrostatic pressure. A positive void coefficient leads to an undesirable increase in reactivity or an increase in the rate of fission. A negative void coefficient implies a decrease in the rate of fission when voids form in the coolant. Therefore, a negative void coefficient introduces a measure of safety. Although the possibility of coolant voiding in a CANDU<sup>®</sup> reactor is extremely low, and is in constant control, the design and operating

---

<sup>‡</sup> 1000 MW<sub>e</sub> output

aspects, in consideration of safety and licensing matters, make a negative void coefficient necessary for purposes of technology sales in some countries.

In the event of a severe loss of coolant or pressure drop in the primary heat transfer system (coolant), a positive void coefficient may contribute to the fuel temperature rising toward the fuel melting point. In current CANDU<sup>®</sup> designs, the effect of the positive void coefficient is counter-balanced by the reactor control and safety systems. A negative void coefficient acts with the opposite effect and thereby contributes to the overall slightly-improved safety of the ACR-1000.

### 1.3.2 Economic Improvements

To reduce initial capital cost, the ACR-1000 will incorporate a more compact core design and a reduction in heavy water inventory by replacing the heavy water coolant with conventional light water. Heavy water is expensive (approximately \$350 per kg [11]). The substitution of light water for heavy water will decrease the total heavy water inventory (coolant and moderator) by approximately 50 percent in comparison to CANDU<sup>®</sup>-6 reactors [9]. The expected diameter of the ACR-1000 calandria will be 7.5 meters with 540 fuel channels. The noticeable reduction in size of the ACR-1000 calandria may be judged by examining Figure 4 below [9].

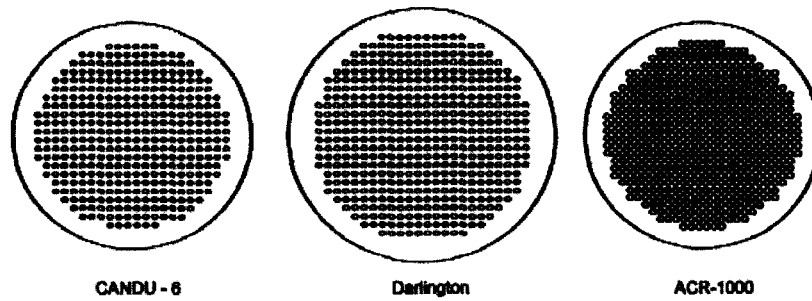


Figure 4. Approximate lattice pitch and size comparison of ACR-1000 with other CANDU<sup>®</sup> Reactors [9].

The reduction in size along with the saving resultant from lower quantities of heavy water will improve the overall economics of the ACR-1000.

### 1.3.3 ACR-1000 Fuel

The unique enabling technology of the ACR-1000 is the fuel bundle design. The ACR-1000 fuel bundle is based on the CANFLEX (43 element) design. In the central element, the UO<sub>2</sub> fuel is replaced by a Burnable Neutron Absorber (BNA) material. The three outer rings of fuel elements (42 elements) contain low enriched uranium (LEU) dioxide fuel (approximately 2 at% <sup>235</sup>U). The use of isotopically enriched uranium is a departure from the CANDU<sup>®</sup> design of the last forty years. A depiction of the ACR-1000 fuel bundle (end view) is shown in Figure 5.

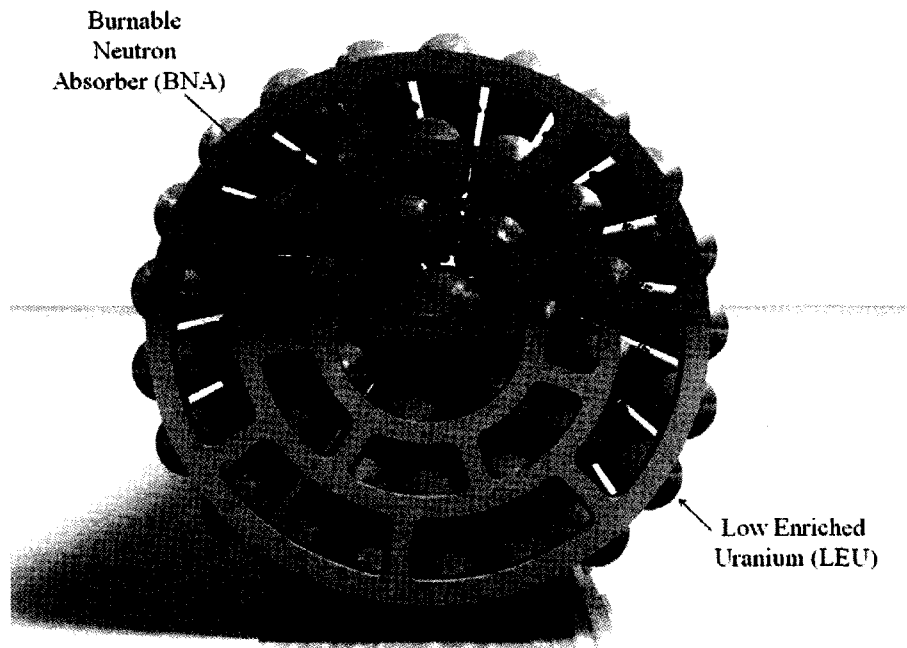


Figure 5. Cross sectional view of ACR-1000 CANFLEX fuel bundle [9,12].

The BNA contributes to a negative void coefficient by decreasing the thermal neutron flux at the centre of the fuel bundle in the event of coolant voiding [13,14]. The BNA is a sintered oxide material of dysprosia ( $Dy_2O_{3,s}$ ) and gadolinia ( $Gd_2O_{3,s}$ ) in a matrix of cubic yttria ( $Y_2O_{3,s}$ ) and stabilized zirconia ( $ZrO_{2,s}$ ). The active elements with respect to neutron absorption are dysprosium ( $Dy$ ) and gadolinium ( $Gd$ ). Both elements have a large neutron absorption cross section, as shown in Table 1. In absorbing neutrons, dysprosium and gadolinium transmute (illustrated in Figure 6) to holmium ( $Ho$ ) and terbium ( $Tb$ ), respectively [5,15]. Since  $Ho$  and  $Tb$  have relatively low neutron absorption cross sections, the ability of the BNA material to consume neutrons decreases slowly as irradiation progresses, hence the name “Burnable” Neutron Absorber.

Table 1. Cross sections of elements in the BNA central element [5].

Element	Neutron Absorption Cross Section $\sigma_{ao}$ (barns)*		Element	Neutron Absorption Cross Section $\sigma_{ao}$ (barns)*
Dy	930	→	Ho	66.5
Gd	49000		Tb	25.5

\*Normalized for isotopic abundance,  $\sigma_{ao}$  denotes the absorption cross section for 0.025 eV.

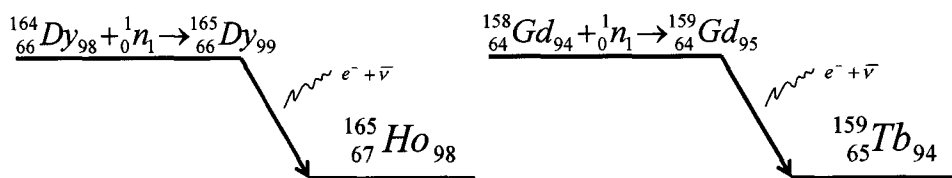


Figure 6. Neutron absorption and Beta ( $\beta^-$ ) decay.

#### 1.4 Technical Concern

If the protective sheathing of the central BNA element were to fail while in operation, the BNA material would come into contact with the coolant. Depending on the solubility of the BNA for the conditions of pH involved, dysprosium and gadolinium could dissolve into the coolant. The large neutron capture cross sections of the dysprosium and gadolinium circulating in the reactor core have the potential to disrupt the neutron economy of the entire reactor. Therefore, the solubility of BNA under CANDU<sup>®</sup> operational conditions must be well understood. Further, this understanding must be expressed in such a way that the extent of BNA solubility can be incorporated into extremely broad-based fuel performance models. In particular, the BNA solubility model should cover excursions of temperature and pH. When the BNA solubility model



is incorporated into fuel performance models, the possible chemical combinations of the soluble species with other materials in the primary heat transport system can be evaluated.

### 1.5 BNA Solubility in Aqueous Solutions

Solubility studies for the pure BNA component oxides, namely  $Dy_2O_3$ ,  $Gd_2O_3$  and  $ZrO_2$ , have been undertaken in support of other technical fields such as geochemistry and electrochemistry. Recently, experimental studies applicable to CANDU® fuel bundle designs have been completed, sufficient to support ongoing engineering of the ACR-1000 reactor. This work at AECL-CRL (Chalk River Laboratory) encouraged the complementary modelling studies of the present project.

#### Geochemistry

Geochemistry studies have focused on the solubility of dysprosium and gadolinium in oxide mineral systems. Work by Diakonov *et al* [16] and Haas *et al* [17] has provided useful insight into the thermodynamic behaviour of these systems. In particular, these works have provided values of enthalpy, entropy, heat capacities and selected Gibbs energy of formation for various species. These values will be considered in the development of the aqueous thermodynamic model, discussed in Chapter 5.

## Electrochemistry

Reviews of dysprosium and gadolinium aqueous metal systems were completed as part of the pioneering work by Pourbaix. His landmark undertaking was completed in 1966 and related aqueous phase equilibrium to redox potential  $E(V)$  and pH at 25 °C [18] for all elements. The diagrams developed by Pourbaix and his coworkers are used as a primary reference and inspiration for the aqueous solubility treatment advanced later in this thesis. Modern computational methods now permit the extension of Pourbaix diagrams to higher temperatures with the assumption that the hydrostatic pressure is sufficient to suppress boiling [19].

With respect to materials involving  $Dy_2O_{3,s}$ ,  $Gd_2O_{3,s}$ ,  $Y_2O_{3,s}$  and  $ZrO_{2,s}$ , there are many similarities to be found between BNA and solid-state oxide-ion electrolytes developed for fuel cell and related applications [12]. The parallel bodies of applied research have yet to be fully integrated.

## Nuclear

Within the area of nuclear engineering, research has been propelled by CANDU® safety and licensing requirements. Noteworthy aqueous studies have included an analysis of the aqueous solubility of dysprosia-doped uranium dioxide, and analysis of the aqueous stability of zirconia. The thermodynamic stability of the solid solubility of the BNA material has been modelled and applied to its manufacture and operational use.

Aqueous solubility studies of dysprosia-doped uranium dioxide have been completed in support of the Low Void Reactivity Fuel (LVRF). Sunder *et al* [20] investigated the aqueous solubility of fuel pellets containing various concentrations of dysprosia in  $UO_2$ . These tests were conducted over a range of temperatures in chemical conditions close to operational CANDU<sup>®</sup> reactor conditions (e.g., temperatures of approximately 300°C, and pH of approximately 10.5 (at 25°C)). X-ray Photoelectron Spectroscopy (XPS) was used to determine the extent of solubility by analyzing dysprosium deposited on metal coupons which were exposed to the solution. Two noteworthy observations were (i) an unexplained drop in pH was observed throughout the experimentation trials and (ii) no dysprosium was observed to be deposited on the metallic coupons exposed to experimental solutions at these specific temperature and pH conditions. Additional studies involving oxides of dysprosium and gadolinium also concluded that the solubility in alkaline solutions, comparable to coolant conditions, is negligible [21].

Additional LVRF studies involving  $Dy_2O_3$  dissolved in  $UO_2$  were recently conducted by Hebert [22] at the Royal Military College of Canada (RMC) using Neutron Activation Analysis (NAA). Powdered samples of pure dysprosium oxide, sintered LVRF fuel, and solid LVRF fuel samples were introduced to solutions of known initial pH. Unfortunately, scattered measurements showing little distinct dependence on pH were attributed to difficulties in preparation and sampling of the solutions. This made it difficult to infer thermodynamic properties for dysprosium-containing ions in solution and in part justified the present research.

The solubility studies by Sunder *et al* [23] investigating pure zirconia confirmed the low solubility and high stability of the main constituent of the BNA matrix material ( $ZrO_{2,s}$ ). Inductively Coupled Plasma Mass Spectrometry (ICPMS) was used to analyze the aqueous concentrations of the zirconium ion for powdered samples exposed to a range of pH at room temperature.

Thermodynamic modelling reported by Corcoran [12] in support of the ACR-1000 fuel design has also been completed. In this work [12], thermodynamic models of the various possible phases were constructed to provide, by Gibbs energy minimization computation, the solid solubility of  $Dy_2O_{3,s}$  and  $Gd_2O_{3,s}$  in cubic zirconia, as affected by pellet sintering temperature. A year-long study involving heating the sample at temperatures in the range of 300°C with intermittent X-Ray Diffraction (XRD) tests confirmed that the metastable cubic phase was, for the most part, retained. The present work is intended to extend the thermodynamic methodology of this study [12] and relate equilibrium involving exposure to aqueous solutions.

## 1.6 Research Objectives

The goal of this project is to develop a thermodynamic treatment of the solubility of dysprosium and gadolinium sesquioxide ( $M_2O_3$ )\* in ACR-1000 BNA material. It is anticipated that this treatment will permit the integration of this knowledge into future fuel performance codes involving existing computational means, or those currently under development by Piro, Lewis, and Thompson [24]. These extensive computations, nevertheless amenable to desktop computing, may involve many chemical elements in contact with the coolant solutions at varying pH and temperature. These are increasingly viewed as the backbone of future nuclear fuel development, such as that for the ACR-1000. Limited experimental work was undertaken to verify such matters as solubility products and solubility in alkaline media, as affected by possible complex ions of the form  $Ln(OH)_n^{3-n}$ . It is the expectation that the solubility treatment will be useful as a framework for such additional work (at coolant temperatures), as may be necessary in support of safety and licensing of the ACR-1000 reactor.

---

\* Sesquioxide is the general term for compounds containing 3 moles of oxygen and 2 moles of another element denoted by  $M$ .

## CHAPTER 2 Background Chemistry

The active neutron absorbing elements in BNA (gadolinium and dysprosium) are chemically similar, and are located in the Lanthanide series of the Periodic Table. These elements, atomic numbers 57-70, are boxed in red in Figure 7.

hydrogen 1 H 1.0079																	helium 2 He 4.0026	
lithium 3 Li 6.941	beryllium 4 Be 9.0122											boron 5 B 10.811	carbon 6 C 12.011	nitrogen 7 N 14.007	oxygen 8 O 16.000	fluorine 9 F 18.998	neon 10 Ne 20.180	
sodium 11 Na 22.990	magnesium 12 Mg 24.305											aluminum 13 Al 26.982	silicon 14 Si 28.086	phosphorus 15 P 30.974	sulfur 16 S 32.065	chlorine 17 Cl 35.453	argon 18 Ar 39.948	
potassium 19 K 39.098	calcium 20 Ca 40.078	scandium 21 Sc 44.956	titanium 22 Ti 47.867	vanadium 23 V 50.942	chromium 24 Cr 51.996	manganese 25 Mn 54.938	iron 26 Fe 55.845	cobalt 27 Co 58.933	nickel 28 Ni 58.693	copper 29 Cu 63.546	zinc 30 Zn 65.39	gallium 31 Ga 69.723	germanium 32 Ge 72.61	arsenic 33 As 74.922	selenium 34 Se 78.96	bromine 35 Br 79.904	krypton 36 Kr 83.80	
rubidium 37 Rb 85.468	strontium 38 Sr 87.62	yttrium 39 Y 88.906	zirconium 40 Zr 91.224	niobium 41 Nb 92.906	molybdenum 42 Mo 95.94	technetium 43 Tc [98]	ruthenium 44 Ru 101.07	rhodium 45 Rh 102.91	silver 46 Ag 107.87	cadmium 47 Cd 112.41	indium 48 In 114.82	tin 49 Sn 118.71	antimony 50 Sb 121.76	tellurium 51 Te 127.60	iodine 52 I 126.90	xenon 54 Xe 131.29		
cesium 55 Cs 132.91	barium 56 Ba 137.33	* 57-70	lutetium 71 Lu 174.97	hafnium 72 Hf 178.49	tantalum 73 Ta 180.95	tungsten 74 W 183.84	rhenium 75 Re 186.21	osmium 76 Os 190.23	iridium 77 Ir 192.22	platinum 78 Pt 195.08	gold 79 Au 196.97	mercury 80 Hg 200.59	thallium 81 Tl 204.38	lead 82 Pb 207.2	bismuth 83 Bi 208.98	polonium 84 Po [209]	astatine 85 At [210]	radon 86 Rn [222]
francium 87 Fr [223]	radium 88 Ra [226]	** 89-102	actinium 89 Ac [227]	thorium 90 Th 232.04	protactinium 91 Pa 231.04	uranium 92 U 238.03	neptunium 93 Np [237]	plutonium 94 Pu [244]	americium 95 Am [243]	curium 96 Cm [247]	berkelium 97 Bk [247]	californium 98 Cf [251]	einsteinium 99 Es [252]	fermium 100 Fm [257]	mendelevium 101 Md [258]	nobelium 102 No [259]		
		* Lanthanide series	lanthanum 57 La	cerium 58 Ce	praseodymium 59 Pr	neodymium 60 Nd	promethium 61 Pm	samarium 62 Sm	europium 63 Eu	gadolinium 64 Gd	terbium 65 Tb	dysprosium 66 Dy	holmium 67 Ho	erbium 68 Er	thulium 69 Tm	ytterbium 70 Yb		
		** Actinide series	actinium 89 Ac	thorium 90 Th	protactinium 91 Pa	uranium 92 U	neptunium 93 Np	plutonium 94 Pu	americium 95 Am	curium 96 Cm	berkelium 97 Bk	californium 98 Cf	einsteinium 99 Es	fermium 100 Fm	mendelevium 101 Md	nobelium 102 No		

Figure 7. Periodic table. Elements involved in the Burnable Neutron Absorbing central element of the ACR-1000 fuel bundle are indicated in solid blue. The Lanthanide series of elements are outlined in dashed red.

The symbol  $Ln$  is sometimes used to collectively refer to any of the elements in the lanthanide series (e.g., sesquioxides denoted as  $Ln_2O_3$ ) when the distinction between different elements is not required. The term Rare Earth element includes scandium and yttrium (atomic numbers 21 and 39) as well as the lanthanides, since all are found in the

same earth mineralization. In the present document,  $Ln$  will be extended to include yttrium. The term Rare Earth implies low concentration of these elements in natural minerals but in fact the overall natural abundance is not particularly low and is comparable to such elements as nickel and copper [25]. The electronic structure of the lanthanides is similar to Xenon (atomic number 54). As the atomic number ascends from La, the  $4f$  electron orbitals are filled. The chemistry of these elements is dominated by the +3 oxidation state. Usually, an increase in atomic number is accompanied by an increase in ionic radius. However, for the lanthanide series of elements, the  $Ln^{3+}$  ionic radius contracts with increasing atomic number, as shown below in Figure 8. This is attributed to the poor shielding of the nuclear charge by the  $4f$  orbital electrons.

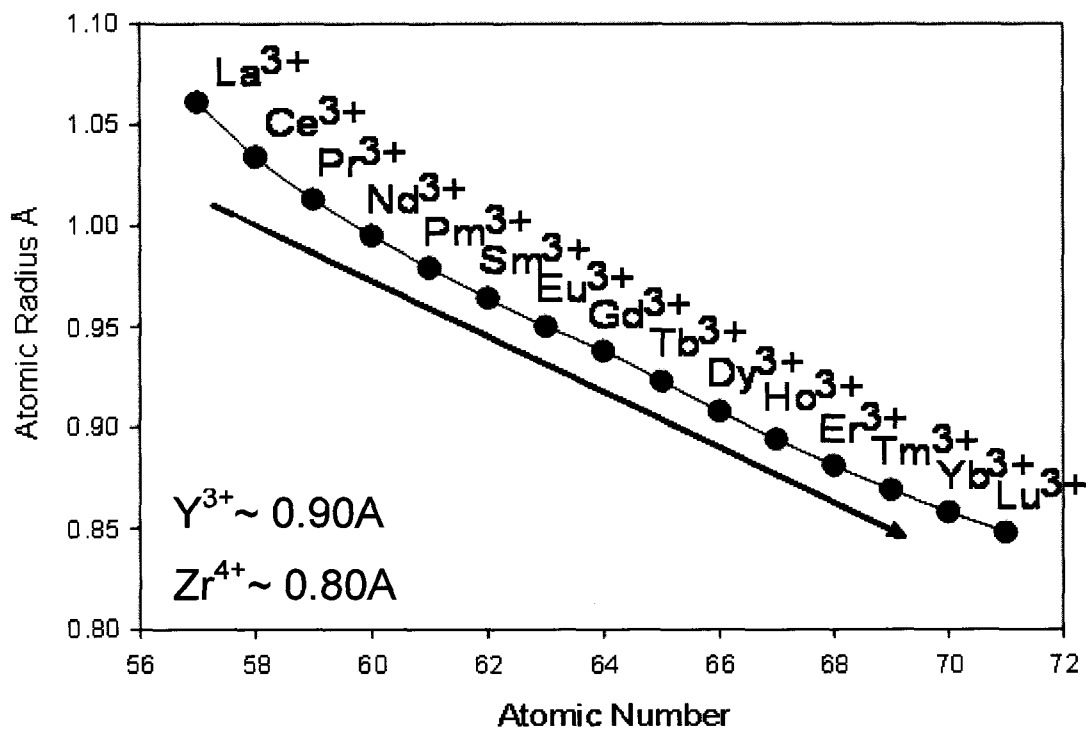


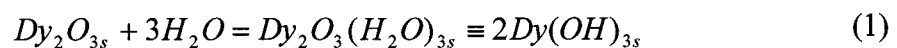
Figure 8. Ionic radii of lanthanide (Rare Earth) trivalent ions given in relation to the comparable radii of trivalent yttrium and tetravalent zirconium ions [26].

For the purposes of subsequent discussion, dysprosium will be the element of choice. However, the discussion remains applicable to gadolinium because of the chemical similarities mentioned above.

## 2.1 General Aqueous Solubility of Dysprosium Oxide

The term solubility, of a particular species, is a means to describe its concentration when it is in coexistence in a particular phase. Solubility is generally sensitive to the temperature, or other variables such as the pH. Lanthanide metals (elements) are highly soluble in acidic aqueous solutions but this process involves a concurrent change in oxidation state typically from  $Ln^0$  to  $Ln^{3+}$ . When an excess of  $Dy(OH)_3_s$  is introduced into water, the process of imparting a fixed concentration of dissolved  $Dy_{aq}^{3+}$  at a specified temperature is similar; however, there is no change in the oxidation state of dysprosium.

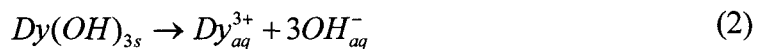
When anhydrous  $Dy_2O_3_s$  and other lanthanide sesquioxides are introduced into water, it is commonly believed that a hydration reaction occurs (at least on the surface of the oxide particles) as shown below



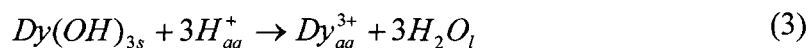
Note that the product of this hydration can, for the convenience of certain applications, either be expressed as a trihydrate or as a molar equivalent trihydroxide. The



concentration of dysprosium ion that eventually accumulates in the solution is thus determined by the chemical equilibrium below.



The forgoing process may equivalently be expressed as



In both cases, it is clear that an increase in acidity (lowering the pH) either by the increase in  $H^+$  concentration or its equivalent, the lowering of  $OH$  concentration, has the same effect. In particular, increasing the acidity will promote the dissolution of  $Dy(OH)_{3s}$  to introduce  $Dy_{aq}^{3+}$  into the aqueous phase at progressively higher concentrations until all of the hydroxide is dissolved [20, 22].

## 2.2 Complex Ions

As the population of ions of opposite charge ( $Dy_{aq}^{3+}$  cations and  $OH$  anions) increases with increasing solubility, it is not uncommon for complex ions to form. The dysprosium +3 aqueous ion is considered to be in solution surrounded by water molecules. The negative charge contribution of the oxygen in water molecules arrange due to the attraction to the trivalent ion, leaving the positive hydrogen atoms of the water molecule exposed. In the case of solutions with high alkalinity, negative hydroxide ions have a tendency to strip a hydrogen from the surrounding water molecules to give rise to

distinct chemical entities of the type  $M(OH)_n^{(3-n)}$ . Table 2 gives examples of various complex ions.

Table 2. Typical complex ions or neutral dissolved species involving hydroxide.

Species	Complex Ion
$Fe^{2+}$	$Fe(OH)_{aq}^+$
$Sn^{2+}$	$Sn(OH)_{aq}^+$
$Li^+$	$Li(OH)_{aq}$

It is noteworthy that solid lithium hydroxide is an alkaline additive used to control CANDU<sup>®</sup> reactor coolant conditions. The existence of the neutral species of lithium hydroxide only very slightly affects the concentration of  $LiOH_{aq}$  needed to provide a specified pH. As is the case for the other two common elements in Table 2, dysprosium ions are also believed to form complex ions to some extent with hydroxide ions [17]. This matter has a bearing on  $Dy(OH)_3_s$  solubility. If complex ions of dysprosium do indeed exist, the solubility of  $Dy(OH)_3_s$  in basic solutions would be somewhat greater than expected, when based solely on Equations (2) or (3). There is also the possibility that more than one hydroxide ion ( $OH$ ) may combine with  $Dy_{aq}^{3+}$  to form a series of species, as the alkalinity is raised to pH values near or slightly above 14. Speculated complexes are listed in Table 3.

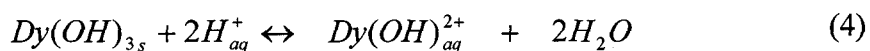
Table 3. Aqueous species of dysprosium.

#	Various Aqueous Hydroxide Complexes of Dy Ions
1	$Dy_{aq}^{3+}$
2	$Dy(OH)_{aq}^{2+}$
3	$Dy(OH)_{2\ aq}^{+}$
4	$Dy(OH)_{3\ aq}$
5	$Dy(OH)_{4\ aq}^{-}$

It is likely that no more than four hydroxide ions would arrange around the  $Dy_{aq}^{3+}$  ion because of steric-effects and the existence up to and including complexes of  $Dy(OH)_{4\ aq}^{-}$  has been proposed by Haas *et al* [17]. The sign of the charge on the complex ion affects the relationship of the pH to the changing solubility of  $Dy(OH)_{3\ s}$ , as discussed below.

#### Positive Complex Ion

In acidic solutions, the  $Dy(OH)_{3\ s}$  consumes hydrogen ions ( $H^+$ ) in the process of dissolution as indicated for example in Equation (4).



Here it is evident that as the pH decreases (increase in  $H^+$  concentration) increases the concentration of  $Dy(OH)_{aq}^{2+}$  giving rise to greater solubility of  $Dy(OH)_{3\ s}$ . The same line of reasoning would also apply to  $Dy(OH)_{2\ aq}^{+}$ .

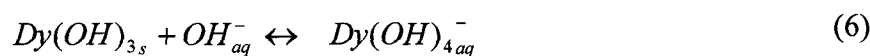
### Neutral Complex

The formation of a neutral aqueous species,  $Dy(OH)_{3\text{ }aq}$ , akin to the recognised neutral aqueous species  $Li(OH)$ , would not affect the pH since  $H^+$  or  $OH^-$  ions are not involved in the process of solubility.



### Negative Complex Ion

The formation of negative complex ions requires that  $Dy(OH)_{3s}$  consume hydroxide ions in the process of dissolution. Therefore, high alkalinity would favour increased solubility, the opposite of conventional expectations if  $Dy(OH)_{4aq}^-$  is not recognized.



With the foregoing discussion of possible complex ions of dysprosium with hydroxide ions and in consideration of the several competing chemical equilibria, it is not unreasonable to expect solubility as qualitatively depicted in Figure 9 below, by the red line labelled 1. This proposed characteristic behaviour is shown in relation to the downward sloping black line labelled 2 that represents the dissolved dysprosium  $Dy_{aq}^{3+}$  concentration on the premise that only the equilibrium in Equation (2) (or equivalently in Equation (3)) is controlling the solubility of  $Dy(OH)_{3s}$ .

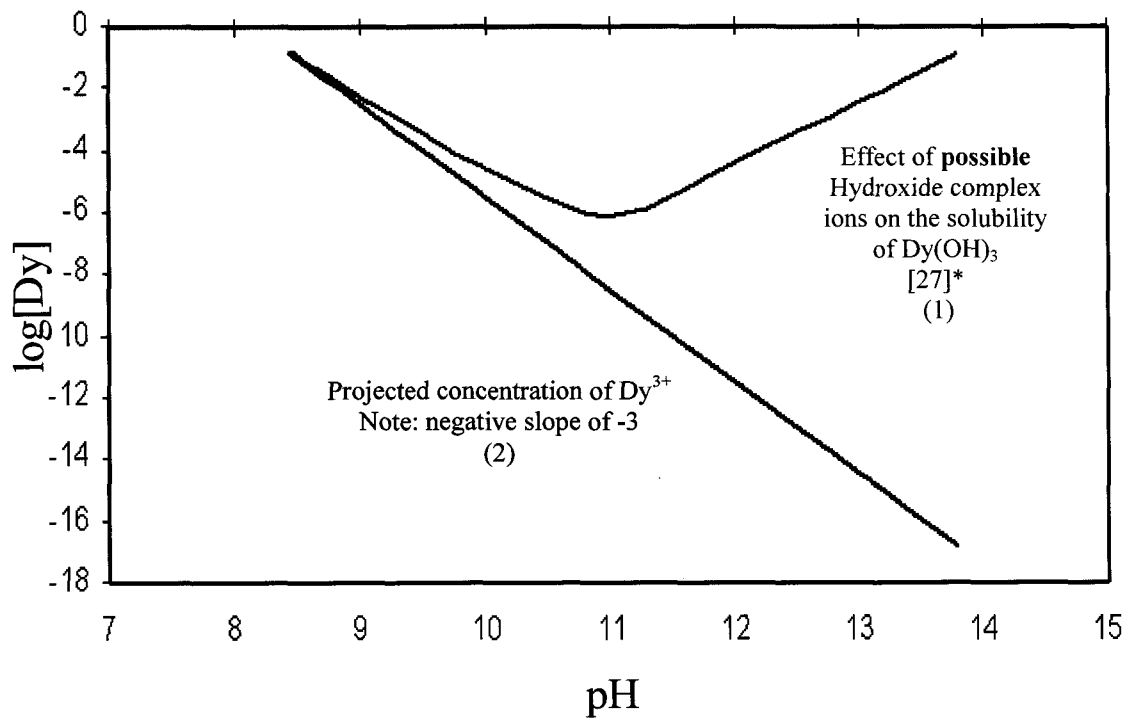


Figure 9. Solubility of  $Dy(OH)_3$ , as influenced by changes in pH. The vertical scale is the logarithm of the molality of dissolved dysprosium.

Justification for the linearity of the black line in Figure 9 is to be found in the solubility product ( $K_{sp}$ ).

$$K_{sp} = [Dy_{aq}^{3+}][OH_{aq}^-]^3 \quad (7)$$

or

$$\log(Dy_{aq}^{3+}) + 3\log(OH_{aq}^-) = \log(K_{sp}) \quad (8)$$

or, at 25 ° C, expressing the concentration of  $OH$  using the pH scale instead

$$\log(Dy_{aq}^{3+}) = -3pH + \log(K_{sp}) + 3(14) \quad (9)$$

\* Professor Peter Tremaine of the University of Guelph first drew attention to this matter.

The  $K_{sp}$  can be determined through knowledge of the concentration of dysprosium and hydroxide ions in solutions of sufficient acidity to preclude high concentrations of the hydroxide complex ions shown in Table 3. The solubility product Equation (7) can then be linked to the Gibbs energy change for Equation (2) by

$$\Delta G_{298K}^{\circ} = -RT \ln(K_{sp}) \quad (10)$$

The connection between the solubility and thermodynamic functions is made in this well-known expression. If the complex ions of dysprosium truly exist at significant concentrations, then additional equilibria involving these ions are necessary to make possible the computation of the collective concentration of all dissolved dysprosium species coexisting with  $Dy(OH)_3$ .

### 2.3 Thermodynamic Modelling

The exploitation of thermodynamic understanding is made possible through the technique of Gibbs energy minimization, an application of the Second Law of Thermodynamics. This powerful analytical technique, developed with the advent of digital computing, allows the consideration of a vast number of coexisting equilibria potentially involving many phases. The integration of this procedure is just now becoming involved in nuclear fuel performance codes to capture the complex chemistry involved with large numbers of elements associated with nuclear fission by-products, and their potential exposure to coolant, fuel sheathing, and materials of reactor construction.

To enable, in a practical sense, the task of Gibbs energy minimization, computational software must be employed. The Facility for the Analysis of Chemical Thermodynamics (F\*A\*C\*T) dating from 1979 employs this technique in conjunction with databases of thermodynamic properties that are automatically searched as required [ 28 ]. This computational software, in successive versions of advancement, specializes in computing multi-component systems and can involve many coexisting phases.

The computational software requires that the thermodynamic data of a species be expressed in terms of Gibbs energy ( $G_T^\circ$ , Equation (11)) recorded in the database as enthalpy of formation from the elements ( $\Delta H_T^\circ$ , Equation (12)), entropy ( $S_T^\circ$ , Equation (13)), and heat capacity ( $C_p$ ). Gibbs energy at any temperature can be therefore expressed by the following

$$G_T^\circ = \Delta H_T^\circ - T(S_T^\circ) \quad (11)$$

This Gibbs energy is sometimes called the “absolute” Gibbs energy in reference to the inclusion of the absolute entropy in the expression. In truth, the Gibbs energy is a relative term that cannot be known absolutely; but, this expression is useful as a starting point in making comparisons of differences in the Gibbs energy between the various possible ways elements can be distributed among phases in varying concentrations.

The enthalpy and entropy can be expressed at various temperatures by integrating the heat capacity as shown below in Equations (12) and (13), respectively.

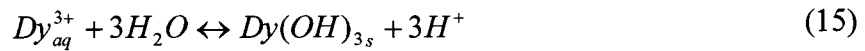
$$\Delta H^\circ_T = \Delta H^\circ_{298K} + \int_{298K}^T C_p dT \quad (12)$$

$$S^\circ_T = S^\circ_{298K} + \int_{298K}^T \frac{C_p}{T} dT \quad (13)$$

Combining Equations (12) and (13) into Equation (11)

$$G^\circ_T = \left[ \Delta H^\circ_{298K} + \int_{298K}^T C_p dT \right] - T \left[ S^\circ_{298K} + \int_{298K}^T \frac{C_p}{T} dT \right] \quad (14)$$

Consider for example, just one of the aqueous equilibria involving dysprosium in the current context,



The conventional standard Gibbs energy change which is related to the equilibrium constant can be calculated by taking the difference in the absolute Gibbs energies as shown in Equation (16).

$$\Delta G^\circ_T = \left( G^\circ_{Dy(OH)_3,T} + 3G^\circ_{H^+,T} \right) - \left( G^\circ_{Dy^{3+},T} + 3G^\circ_{H_2O,T} \right) \quad (16)$$

Conventions have defined that the absolute Gibbs energy for the hydrogen ion is zero at all temperature ( $G^\circ_{H^+,T} \equiv 0$ ). Thus Equation (16) reduces to,

$$\Delta G^\circ_T = \left( G^\circ_{Dy(OH)_3,T} \right) - \left( G^\circ_{Dy^{3+},T} + 3G^\circ_{H_2O,T} \right) \quad (17)$$



### 2.3.1 Precision and Accuracy in Recording Thermodynamic Properties

The nature of chemical equilibrium thermodynamic computations necessarily involves the repetitive computation of differences in Gibbs energies for the potentially many different ways elements combine to form possible compounds; that is to say, the most stable combination of elements into various compounds, at a particular temperature and pressure. This can be deduced by finding, through repetitive computations, those compounds that yield the most negative Gibbs energy change for an arbitrary initial condition (e.g. the un-combined (free) elements). In this methodology, it is therefore necessary to preserve small measurable differences between sometimes very large numbers. As a consequence, it is common to record (or compute) large values for properties, such as the enthalpy of formation, with high precision. Although, the absolute accuracy is almost invariably far lower.

To amplify on the important matter in the previous statement, consider the case of recording the vapour pressure of water using equations for the Gibbs energies of the respective phases (liquid and vapour). At a temperature of 350 K, the standard “absolute” Gibbs energy of the liquid following the conventions described above is found to be  $-310633.9 \text{ J}\cdot\text{mol}^{-1}$ . For the vapour phase, the standard “absolute” Gibbs energy at the same temperature is  $-308031.3 \text{ J}\cdot\text{mol}^{-1}$ . From the differences between these large numbers, the vapour pressure of water may be calculated using the following well-known equation

$$\Delta G^\circ = (-308031.3) - (-310633.9) = 2602.6 = RT \ln(P_{H_2O}) \quad (18)$$

At 350 K, this yields  $P_{H_2O}$  of 0.409 atm (absolute). It is this vapour pressure, to be accurately preserved, that must be provided by the careful recording of the Gibbs energies of the phases to a numerical precision so that the resultant  $\Delta G^\circ$  can be correctly computed. If the only purpose in recording the thermodynamics of  $H_2O$  phases were to provide the vapour pressure, the fundamental information leading to the Gibbs energies would not need to be recorded, as discussed above. However, if the intention is to also use the Gibbs energies for  $H_2O$  in other processes, such as the formation of hydrates and hydroxides, as in the present work, the necessity of recording the Gibbs energies to high precision is evident.

#### 2.4 Pourbaix Diagrams

A useful depiction of Gibbs energy minimization computations applied to aqueous systems is the stability diagram popularized by Pourbaix in his pioneering publication (*Atlas of Electrochemical Equilibria in Aqueous Solutions* [18]). These diagrams are isothermal plots generally at 25°C indicating domains of stability of a particular chemical species on  $E_h(V)$ -pH coordinates. The Standard Hydrogen Electrode (SHE) is typically used as the reference potential for the redox potential ( $E_h(V)$ ) scale<sup>§</sup>. Further explanation will be provided in the following chapter. A review of Pourbaix diagram construction involving Gibbs energy minimization and the concepts discussed

---

<sup>§</sup> The Saturated Calomel Electrode (SCE) is generally used as a more convenient reference in experimental work but is typically converted to the SHE scale by the addition of 0.242V at 25°C.

above is summarized in the Uhlig Corrosion Handbook [29], along with present work amplifying these diagrams to cover temperatures above 25°C (in the next edition currently in press [19]). A typical Pourbaix diagram for a lanthanide element (europium) is shown in Figure 10 below. Solid phases are shown in bold face.

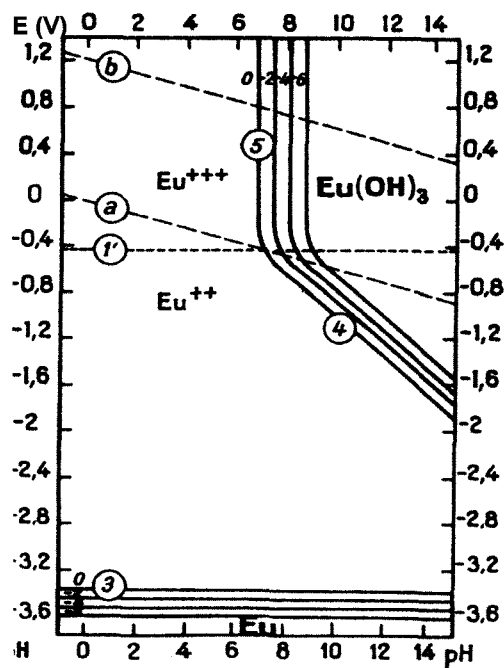


Figure 10. Pourbaix diagram of the europium – water system from the Atlas of Electrochemical Equilibria in Aqueous Solutions [18].

This diagram gives evidence of the stability of  $Eu(OH)_3$  in water since the field for  $Eu_2O_3$  does not appear. This diagram is characterized by areas or domains of stability for four europium species: namely  $Eu_s$ ,  $Eu_{aq}^{2+}$ ,  $Eu_{aq}^{3+}$  and  $Eu(OH)_3$ . The placement of the metallic  $Eu_s$  field calls attention to the extreme instability in contact with water as a result of the very low standard reduction potential ( $\sim -3.4$  V (SHE)) for

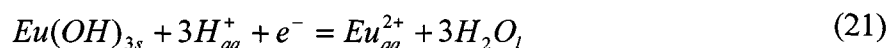


being far below that for



which is near zero depending on the pH, (line “a”).

At redox potentials higher than  $\sim -3$  V (SHE), particularly for pH less than 7, europium exists as  $Eu_{aq}^{2+}$  ions in water. When the redox potential becomes greater  $-0.4$  V (SHE) and crosses the dotted line  $l'$   $Eu_{aq}^{3+}$  ion becomes more dominant than  $Eu_{aq}^{2+}$ . To take the case of  $Eu_{aq}^{3+}$ , increasing concentrations of hydroxide ions above about pH 7, results in precipitation of  $Eu(OH)_{3s}$ . The relationship between the concentrations of  $Eu_{aq}^{3+}$  in water when it coexists with  $Eu(OH)_{3s}$  is depicted by the family of lines labelled 5. The number scale on the lines refers to the exponent of 10 giving the ion concentration in molality (m). Thus by pH 9 or slightly less, the concentration of  $Eu_{aq}^{3+}$  in aqueous solution coexisting with  $Eu(OH)_{3s}$  is about  $10^{-6}$  m. The family of lines 5 bends as it crosses the line  $l'$  to become the family of lines 4 that represents the equilibrium



This equilibrium calls attention to the significance of the redox potential, which is why this particular element was chosen for the present discussion.

The upper and lower lines on Figure 10 and Figure 11 labelled “a” and “b” give the redox potential of water as controlled by hydrogen and oxygen saturation (1 atm pressure), respectively. Between the lines “a” and “b”, the partial pressures of both  $O_{2g}$  and  $H_{2g}$  are less than 1 atm and are related to each other by the dissociation constant for water decomposition into its elemental pure gases [18]. The half-cell reaction for the hydrogen saturation “a” line is



The half-cell reaction for the oxygen saturation “b” line is



Between lines “a” and “b”, water is stable with respect to decomposition. Above line “b” conditions are so oxidizing that oxygen gas is evolved. Below line “a” conditions are so reducing that hydrogen gas is expelled. These thoughts are captured in Figure 11.

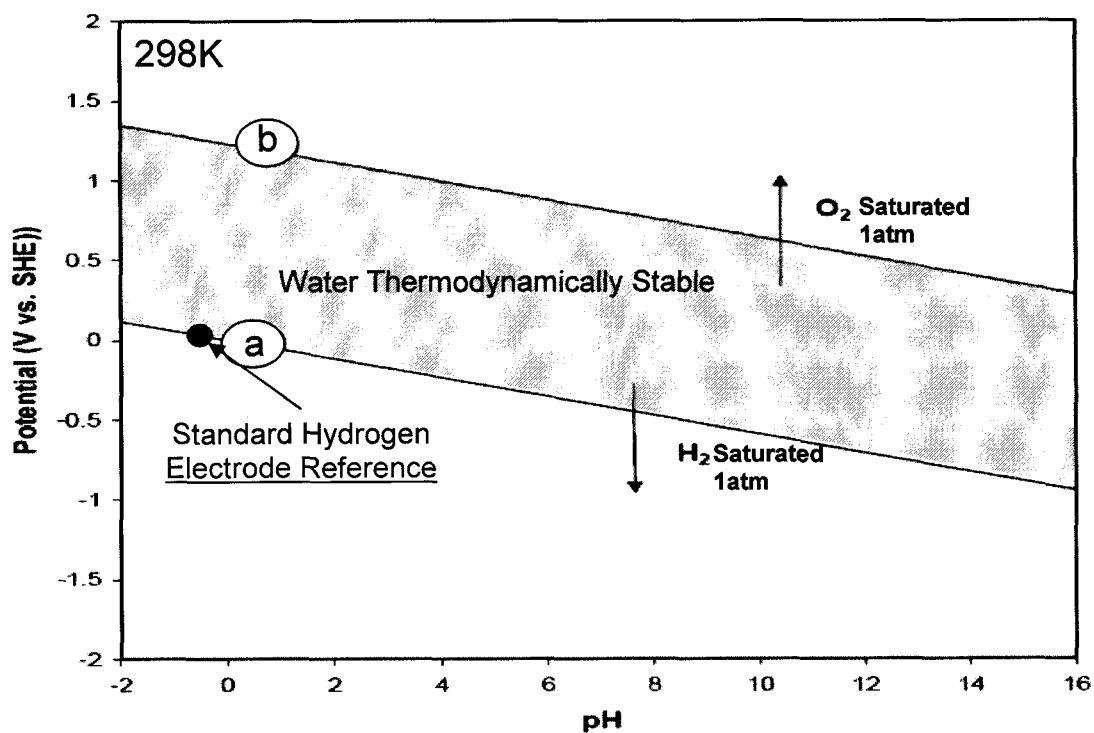


Figure 11. General Pourbaix diagram of water.

To summarize the general discussion of Pourbaix diagrams, a condition of oxygen saturation of water would permit the study of the equilibrium



A condition of hydrogen saturation could complicate such a study by the partial reduction of  $Eu_{aq}^{3+}$  to  $Eu_{aq}^{2+}$ . To be more specific, if a hydrogen-saturated aqueous solution containing  $Eu(OH)_{3s}$  was at pH of approximately 9 (see Figure 10) the concentration of europium in the water would be approximately  $10^{-6}$  m with most of the europium being  $Eu_{aq}^{2+}$ . If the pH were now lowered to nearer 7, the concentration of europium in water would reach a total of about 1 m with approximately equal concentrations of  $Eu_{aq}^{2+}$  and

$Eu_{aq}^{3+}$  (both  $\sim 0.5$  m). Observe in Figure 10 the lines labelled 4, 5, and 1' all intersect at hydrogen saturation line "a".

Figure 12 below is the dysprosium Pourbaix diagram from Pourbaix's original book. It differs from that of europium in that there is only one oxidation state. Thus, the solubility of  $Dy(OH)_3_s$  in water is unaffected by changes in redox potential ranging from oxygen saturation to hydrogen saturation. This observation makes it possible to study the solubility of  $Dy(OH)_3_s$  in aqueous solutions involving accurate measurements of pH using a hydrogen electrode. The same conclusion can be reached for gadolinium, as is evident from the Pourbaix diagram also shown in Figure 12.

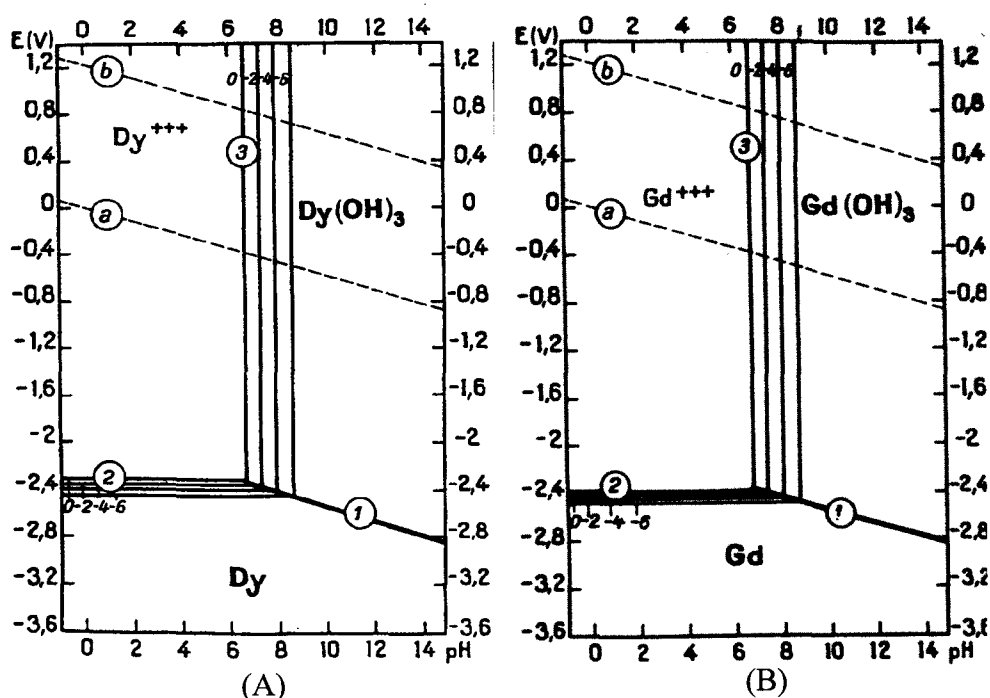


Figure 12. Pourbaix diagram of dysprosium – water (A) and gadolinium – water (B) from the Atlas of Electrochemical Equilibria in Aqueous Solutions [18].

In the three Pourbaix diagrams for *Eu*, *Dy*, and *Gd*, it is evident that the lower limit of concentration deemed significant is  $10^{-6}$  m. While this may be satisfactory for most aqueous chemistry purposes, the particular needs of the nuclear industry must make inquiries about much lower concentrations, due to the high neutron capture cross sections of these elements as previously discussed in relation to the proposed ACR-1000 fuel bundle. It is at these lower concentrations associated with pH levels near 10 where possible complex formation with hydroxide ions may become a matter of significance.



## CHAPTER 3 Experimental Procedures

The experimental work to gather the necessary data in support of the aqueous chemistry of dysprosia and gadolinia, sufficient to infer reasonable thermodynamic properties of the various phases and species, can be divided into three categories:

- 1) Discrete determination and verification of the solubility products for  $Dy(OH)_3$  and  $Gd(OH)_3$ .
- 2) Thermogravimetry to study the decomposition of the hydroxides and hydrates of  $Dy_2O_3$  and  $Gd_2O_3$ .
- 3) Neutron Activation Analytical studies of saturated alkaline solutions ranging in pH from approximately 10 to 14.

### 3.1 Measurement of pH

For the purposes of conducting parts 1 and 3, accurate measurements of pH are required. There are various ways of determining the pH of a solution. These can range from qualitative indicators (litmus paper, coloured indicators) to sensitive electronic pH meters based on the use of a glass electrode. Electronic pH meters are almost universally used, except for the extremes of pH, where this approach does not provide the precise measurements of acidity or alkalinity that may be required. Furthermore, these devices require frequent calibration with buffer solutions and are susceptible to slow drift with time. Accordingly, electronic pH meters are not the best choice for thermodynamic studies which emphasize a high degree of reproducibility. To circumvent this concern, it was decided to use the primary standard in pH measurements, the platinum hydrogen electrode, with potential measured with respect to a saturated calomel electrode. This

choice is possible because the oxidation state of  $Dy_{aq}^{3+}$  and  $Gd_{aq}^{3+}$  is not affected by hydrogen.

The pH is defined as

$$pH = -\log_{10}(a_{H^+}) \quad (25)$$

where  $a_{H^+}$  is the activity of the hydrogen ion in aqueous solution. The activity is a measure of effective concentration that has meaning particularly in reference to computations of thermodynamic equilibrium. However, as a consequence of the conventions used in referencing the activity (the standard state) for dilute aqueous solutions, it is convenient and permissible to express activity as molality ( $m_{H^+}$ ). Consequently, Equation (25) becomes,

$$pH = -\log_{10}(m_{H^+}) \quad (26)$$

The electrochemical equilibrium at the *Pt* electrode can be expressed as



The platinum surface in contact with the solution senses the electrochemical potential. In a solution of a particular pH, this potential has a unique value when the hydrogen partial pressure is known. The temperature is also a factor but the conventions in aqueous solutions define the temperature effect on this particular equilibrium (standard electrode potential) to be zero. This convention is made because of the use of the hydrogen

electrode as a primary standard in referencing the potentials of other electrochemical equilibria (that is, those involving electron transfer). The potential of the *Pt* electrode follows the Nernst equation.

$$e_{Pt} = e^{\circ} - \frac{RT}{\mathfrak{F}} \ln\left(\frac{P_{H_2}^{\frac{1}{2}}}{m_{H^+}}\right) \quad (28)$$

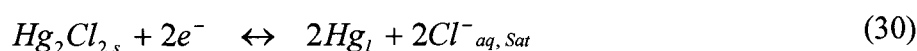
where:

- $e^{\circ} \equiv 0V$  (hydrogen standard electrode potential by definition at all temperatures)
- $m_{H^+}$  Molality of the hydrogen ion in solution ( $\text{mol}\cdot\text{kg}^{-1}$ )
- $\mathfrak{F}$  Faraday constant ( $\text{C}\cdot\text{mol}^{-1}$ )
- $R$  Ideal gas constant ( $\text{J}\cdot\text{K}^{-1}\cdot\text{mol}^{-1}$ )
- $T$  Temperature (K)
- $P_{H_2}$  Partial pressure of hydrogen gas (atm)

The potential defined by Equation (28) for a particular hydrogen concentration and hydrogen partial pressure cannot be measured absolutely. Therefore, a reference electrode must be employed and an open circuit (current = 0 amp) voltage measurement ( $E_{measured}$ ) is made between the *Pt* electrode ( $e_{Pt}$ ) and the reference. Among the most widely used secondary reference electrodes in aqueous electrochemistry is the Saturated Calomel Electrode (SCE). Owing to the construction of the reference electrode, its potential is not affected appreciably by the solution in which it is immersed. Thus, the measured potential in the experimental work, described hereafter, is the difference between the electrode potentials as shown by Equation (29). In the present application, the *Pt* electrode is the indicator electrode providing the desired measurement of pH and the saturated calomel electrode is the fixed (secondary) standard.

$$E_{measured} = (e_{SCE})_{reference} - (e_{Pt})_{pH \text{ indicating electrode}} \quad (29)$$

The saturated calomel reference electrode (SCE) consists of mercury metal in contact with mercurous chloride ( $HgCl$  or more commonly  $Hg_2Cl_2$ ) and saturated aqueous potassium chloride solution (~4 molal). The electrochemical equilibrium and half cell potential for the calomel reference electrode can be expressed as



$$e_{SCE \text{ reference}} = +0.242 \text{ V at } 298.15 \text{ K}$$

The significance of the sign convention is that it conveys knowledge of the polarity of the saturated calomel electrode, in this case, when connected to the standard hydrogen electrode (pH = 0,  $P_{H_2}$  = 1.0 atm).

A physical representation of the preceding discussion of electrochemical equilibria in relation to the present project appears in Figure 13.

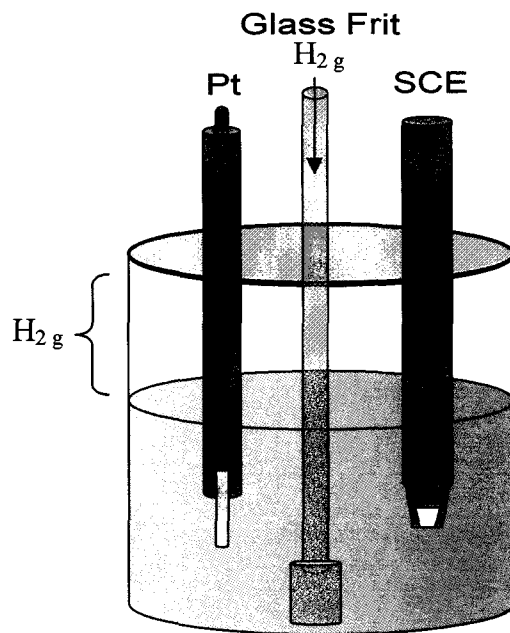


Figure 13. Experimental Setup to measure pH using a  $Pt / H_{2g}$  and SCE.

In the apparatus shown in Figure 13, the pH is provided from the measurement of the cell voltage. A direct voltage measurement can be converted into a corresponding pH measurement by the following rearrangement of Equations (28) and (29)

$$pH = \frac{(E_{measured} - e_{SCE}) \cdot \mathfrak{F}}{2.303RT} - \frac{1}{2} \log(P_{H_2}) \quad (31)$$

It was found that a 1 mV change corresponded to a change in pH of approximately 0.02. Also, taking into account the temperature effect on the system, including the saturated calomel reference electrode [30], a change in temperature of one degree Celsius corresponded approximately to a change in the related pH of approximately 0.02. Thus, the temperature must be well-known, but even so, measurements of pH with precisions greater than 0.01 should not be claimed.

### 3.2 Determination of Solubility Product

The  $Dy_2O_3$  powder was purchased from Alfa Aesar. Scanning electron microscope images of the oxide powder are included in Appendix A. Approximately 5 g of the oven dried ( $\sim 500^\circ\text{C}$ ) anhydrous dysprosium sesquioxide ( $Dy_2O_3$ ) was introduced to 500 ml of water to which sufficient nitric acid was then added to dissolve all of the  $Dy_2O_3$  and bring the pH to approximately 1. The solution was then titrated with a standard lithium hydroxide solution ( $\sim 2$  molal) until precipitation occurred. Afterward, as additional lithium hydroxide solution was introduced, a white precipitate continued to form and additions of lithium hydroxide solution had little effect on the pH, until virtually all of the dissolved dysprosium (ion) had precipitated. Subsequently, the pH rapidly increased to a high alkaline value ( $\sim 10$ ). The foregoing description is the typical expectation of a titration involving the formation of a precipitate.

There is concern in the water chemistry with rare earth compounds that carbonates may form by contact with air. The small partial pressure of  $CO_2$  in air is sufficient to dissolve over time in water resulting in hydroxide-carbonate precipitation. The manner in which the pH was measured with a hydrogen electrode provided the side benefit of a cover gas, keeping air from direct contact with the solution.

### 3.3 Thermogravimetric Analysis (TGA)

Thermogravimetric analysis of the precipitate produced by titration studies was performed. A Setaram TG-DTA 2400 along with a TA instrument Thermogravimetric

Analyzer 2050 was used in this work and the cover gas was ultra high purity Argon, purchased from Air Liquide Canada.

Generally, to prepare the samples for TGA, the precipitate was filtered and dried in air at room temperature for at least a day until most of the residual free water had evaporated. Then, milligram quantities (~50 mg) of the superficially dried precipitate were introduced in the TGA. The weight loss was measured as the temperature was ramped from room temperature (approximately 25°C) to 800°C over periods of several hours, depending on the TGA used. The results are discussed and interpreted in the following chapter.

#### 3.4 Solubility in Highly Alkaline Solutions

In the particular application to which the research in this thesis is directed, the requirement is that the solubility of dysprosia and gadolinia in alkaline solutions be well understood. To be more specific, recall that the BNA material containing the dysprosia and gadolinia may come into contact with light water coolant with the pH expected to be controlled near pH 10.5 (298 K) by small lithium hydroxide additions. This pH is selected for such reasons as to add protection to the oxide on the Zircaloy fuel sheath from otherwise corroding more rapidly than is desirable. Accordingly, studies were conducted on the very low solubility of  $Dy(OH)_3$  in solutions of high pH, covering the range 10-14, to near the point of lithium hydroxide saturation. The saturated solutions of  $Dy(OH)_3$  were prepared by continuous agitation over several hours (~20 hours plus). The solution was then allowed to settle for at least 24 hours, resulting in an optically clear

solution. Samples of the supernatant solution were then analyzed by neutron activation analysis at the SLOWPOKE-2 facility at RMC.

Neutron activation analysis provides a means to determine the concentration of specific elements. A sample is collected and bombarded with neutrons. The neutrons are absorbed by the sample creating radioactive isotopes. These isotopes begin to decay from their excited nuclear states. The decay process involves the emission of gamma rays with an energy characteristic of each element, analogous to a fingerprint. The concentration of a specific element is found by studying the intensity of the characteristic energy emissions, in relation to a standard sample of known concentration. The technique is particularly sensitive for strong neutron absorbers such as dysprosium [31].

Prepared samples, as discussed above, were irradiated for 0.5 min and placed in a high purity germanium coaxial photon detector system Model No. GMX 35-PLUS 45-N31974A. The analysis was conducted in accordance with the Canadian Association for Laboratory Accreditation Inc. (CALA) [32].



## CHAPTER 4 Experimental Results

### 4.1 Precipitation Experiments

A typical titration experiment involving the introduction of lithium hydroxide solution, to initially acidic solutions containing dissolved  $Dy_{aq}^{3+}$ , is illustrated in Figure 14.

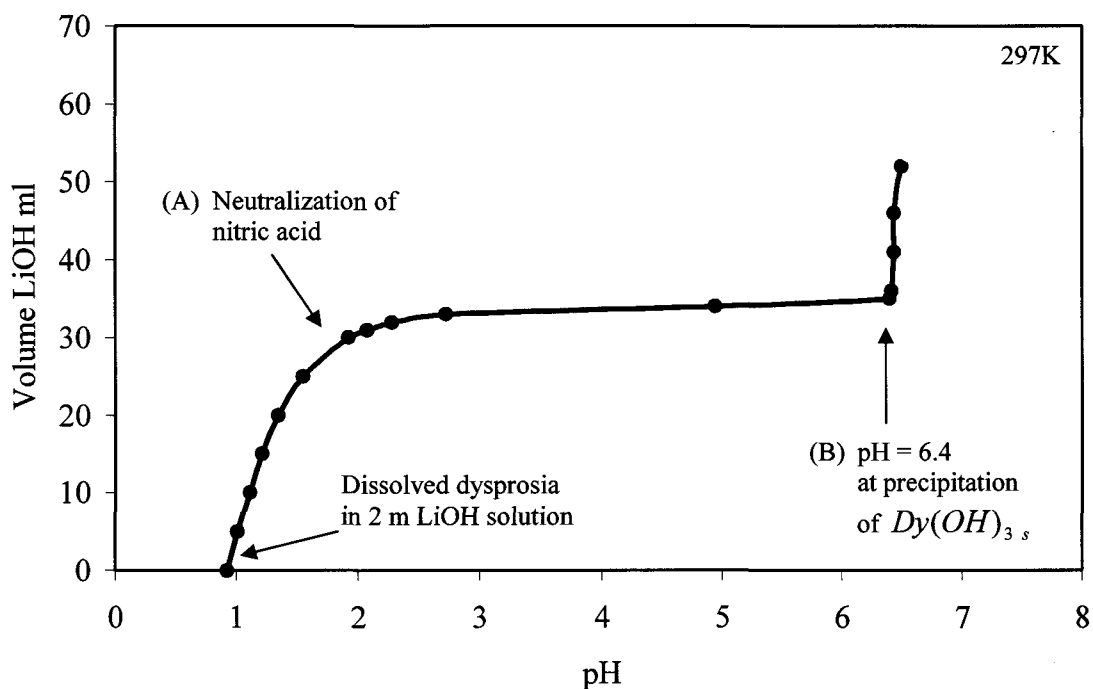


Figure 14. Precipitation of  $Dy(OH)_3_s$  providing data to determine the solubility product.

In Figure 14, approximately 2 m lithium hydroxide solution was added to an acidic ( $HNO_3$ ) solution (pH ~ 1) containing approximately 5 g dysprosium oxide. There are two features of interest on Figure 14, namely, the acid neutralizing curve (labelled A) and the onset of precipitation associated with the steeply rising part of the curve, at approximately pH 6.4 (labelled B). The precipitation point is interpreted as meaning the chemical combination of  $Dy_{aq}^{3+}$  aqueous ions with hydroxide ions ( $OH$ ) to form a

precipitate of  $Dy(OH)_3$ , as in Equation (2). The numerical treatment of this data in relation to establishing the Gibbs energy of formation of  $Dy(OH)_3$  will be discussed in the next chapter. Experimentation with gadolinium was conducted in a similar manner as shown in Figure 15 below.

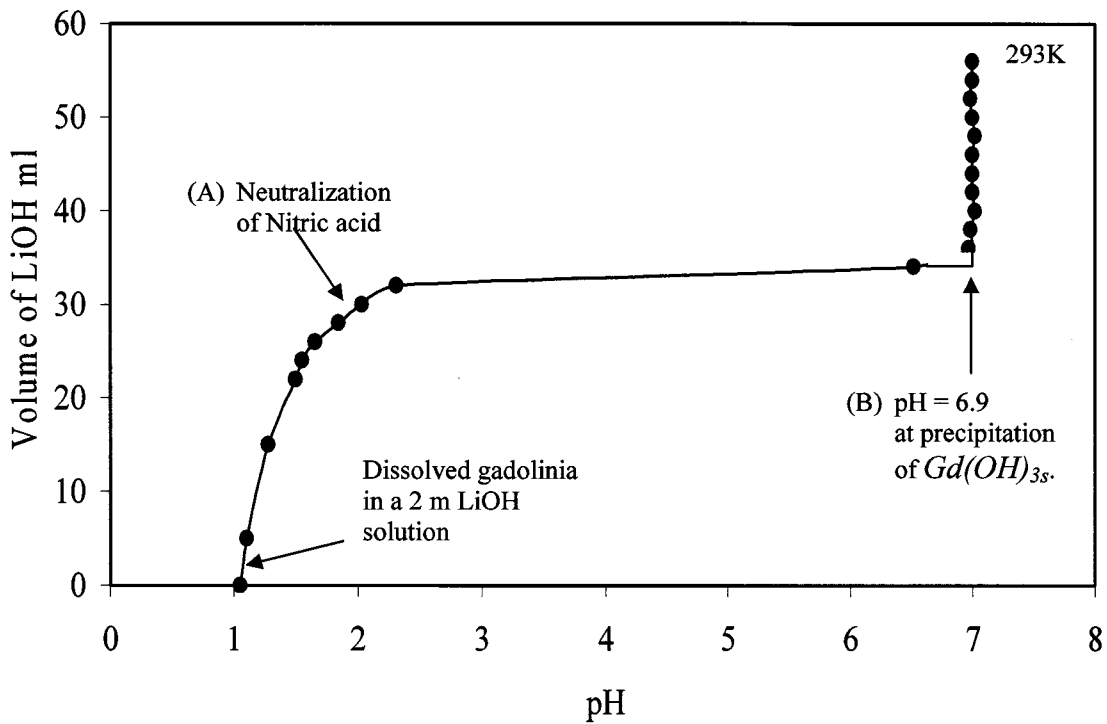
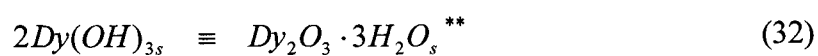


Figure 15. Precipitation of  $Gd(OH)_3$  providing data to determine the solubility product.

Figure 15 is similar to Figure 14 but presents data for gadolinium. The noteworthy difference is the slightly higher pH associated with the onset of  $Gd(OH)_3$  precipitation (pH ~6.9) for an element that, as previously discussed, is very similar chemically to dysprosium. Of course, the nuclear properties of gadolinium are vastly different than dysprosium in relation to its ability to capture neutrons.

## 4.2 Thermogravimetric Analysis (TGA) Results

In the previous section, it was tacitly assumed that the precipitates were the trihydroxides of the lanthanides under study. To consider the case of dysprosium, as the supposed  $Dy(OH)_3$  is heated, water vapour is driven off until the material becomes the anhydrous sesquioxide,  $Dy_2O_3$ . This fact is more evident by the molar equivalence shown below.



This recognition is useful when considering the mass loss to be expected when the dry trihydroxide is heated to sufficiently high temperatures in the thermogravimetric equipment. The TGA results for the dehydration of the precipitate  $Dy(OH)_3$  are shown in Figure 16.

---

\*\* Describing a hydroxide as its respective hydrate is made for convenience purposes in illustrating the water loss associated with heating in the TGA procedure and does not convey structural information about the condensed phase.

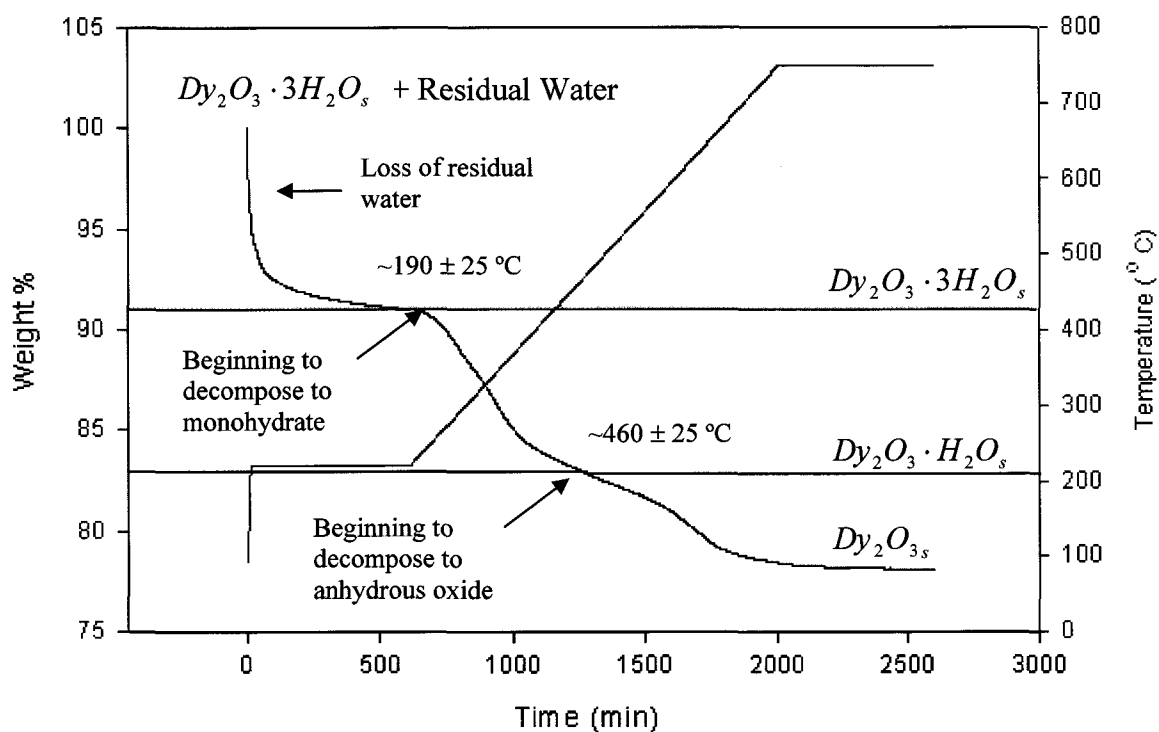
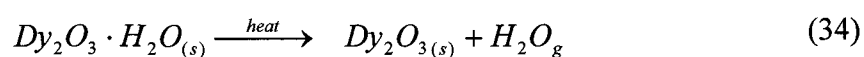
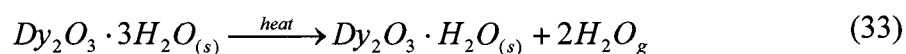
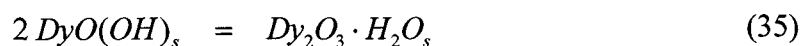


Figure 16.  $Dy(OH)_3$  dehydration profile.

The different scales on each side of Figure 16 provide an indication of mass loss (left) and temperature (right) at comparable times. It appears, from the irregular behaviour of the mass loss as the temperature is increased, that water is driven off in 2 steps. That is to say, the trihydrate loses two moles of water first, followed by the additional mole of water when the temperature has increased to a sufficiently higher temperature. The two dehydration reactions are listed below



Note that the monohydrate could also be expressed alternately by  $DyO(OH)_s$  as the equivalence below makes clear.



Although the partial pressure of water vapour was not controlled in the TGA, the liberation of two moles of water from the trihydrate is considered to occur at approximately  $190 \pm 25$  °C. The final mole of water vapour was interpreted as being driven off at approximately  $460 \pm 25$  °C. These judgements are to be understood in reference to considering the mass loss of pure water heated in the TGA without fixing the partial pressure of water vapour. To take the case of water, mass loss occurs well below the boiling point as the vapour pressure of water is building to cause rapid evaporation. The construction of the TGA precluded fixing the vapour pressure of water at a significant level (e.g. 0.1 atm) since condensation would occur in the colder parts of the apparatus affecting the knowledge of the true partial pressure. By the time the sample reached about 750°C, approximately a 13% mass loss was observed. This is near the theoretical mass loss equivalent to the loss of three moles of water affirming that the assumption of the precipitation of trihydroxide in the previous section was valid.

Thermogravimetric analysis of the gadolinium precipitate is shown in Figure 17. The observations were very similar to those for dysprosium, though the loss of the final molecule of hydration occurred at a somewhat higher temperature shown below.

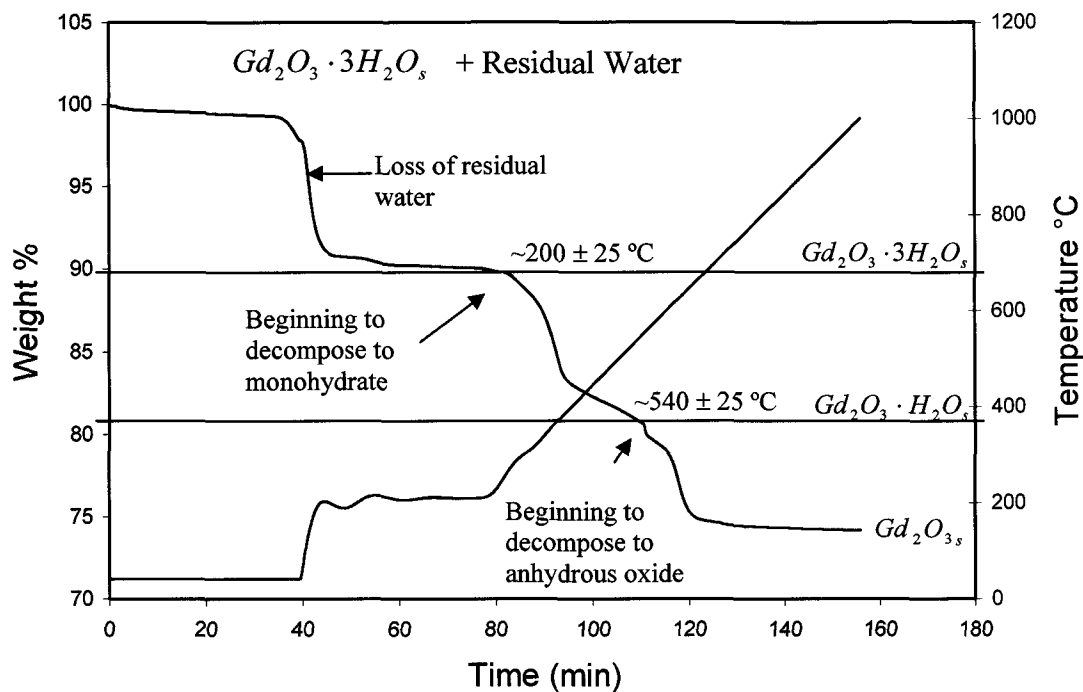


Figure 17.  $Gd(OH)_3$  dehydration profile.

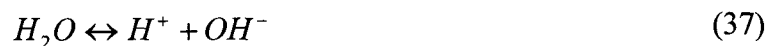
#### 4.3 High Alkaline Solubility Results

Given that the solubility is considered to be very low (and therefore difficult to measure) at alkaline conditions of commercial interest, experiments were conducted near room temperature in concentrated alkaline solutions. To better understand the nature of solubility in highly concentrated alkaline solutions, it is necessary to first consider the chemistry of lithium hydroxide at extreme alkalinity.

Measurements of pH for four solutions of differing lithium hydroxide concentrations were examined and compared to the expected pH values associated with complete dissociation. The findings are summarized in Table 4. The theoretical pH was calculated using

$$pH = 14.14 + \log(\text{molality}) \quad (36)$$

The constant representing the logarithm of the dissociation constant for



is greater than 14 because the temperature was 21°C instead of 25 °C, calling attention to the temperature effect on the pH scale. In many cases this matter is ignored, since the correction is minimal in the vicinity of room temperature. Temperature effects on the pH of solution will be discussed in greater detail in Chapter 6.

Table 4. Measurements of pH in concentrated lithium hydroxide solutions.

Solution	Prepared Concentration (molality)	Expected pH	Measured pH
1	4.01	14.74	14.15
2	2.00	14.44	13.97
3	1.00	14.14	13.78
4	0.10	13.14	12.94

The measured pH values in relation to the expected pH are shown in Figure 18.

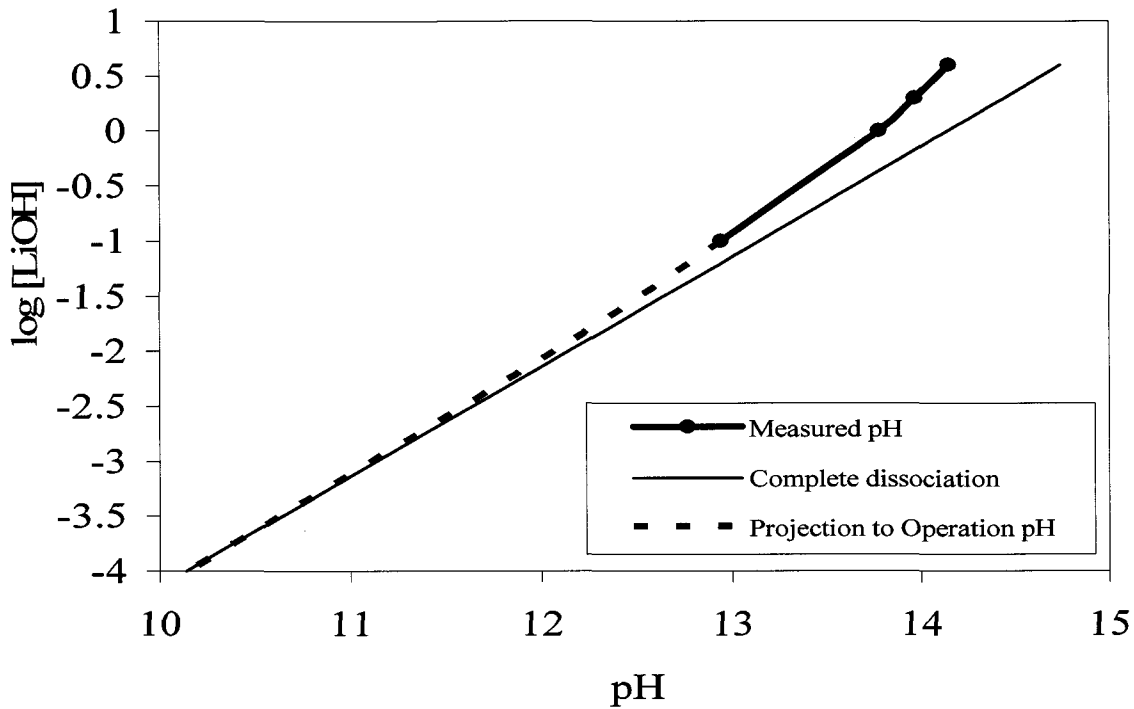


Figure 18. Measurements of pH in Lithium hydroxide solution at 21°C.

The black line connects the experimental measurements. An extrapolation to approximate conditions of reactor pH (near 10) is shown as well\*. The red straight line depicts Equation (36) assuming that  $LiOH$  additions completely dissociate to  $Li^+_{aq}$  and  $OH^-_{aq}$  ions. There is evidence that this assumption may not be so. This matter is explored further in the next chapter, with considerations made for the following possible neutral species of lithium hydroxide.



\* Recall that CANDU® reactors have the coolant with a pH 10 to 10.3 at 298 K.



The product species in this equilibrium is to be understood as a dissolved neutral complex ion for which thermodynamic data independently exist and is in accord with the behaviour illustrated in Figure 18. This matter must not be overlooked in considering the solubility of  $Dy(OH)_3$ , which is expected to involve the appearance of hydroxide complex ions as the pH is progressively raised. That is to say, the concentration of hydroxide ions available to complex  $Dy^{3+}_{aq}$  is somewhat less than the pH would suggest. For example, if the pH at 25°C were exactly 14, the hydroxide ion concentration might be falsely taken to be 1 molal, when in fact (because of the incomplete dissociation of lithium hydroxide qualitatively evident in Figure 18 above), the free hydroxide concentration is significantly less. This matter is pursued in the next chapter in the process of extraction of thermochemical information from the measurements, for the properties of the aqueous ions of dysprosium.

Aqueous measurements for dysprosium (total concentration) in saturated alkaline lithium hydroxide solutions are shown in Figure 19. The exact measurements are recorded in the report from the Analytical Sciences Group in Appendix B.

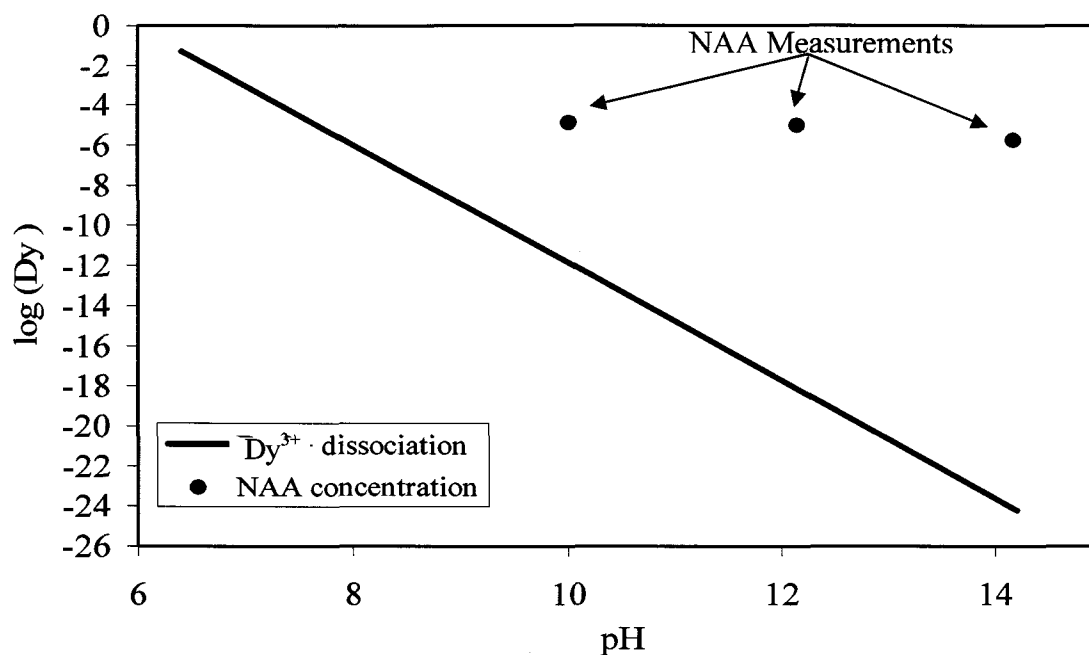


Figure 19. Measured concentrations (molality) of dissolved dysprosium in highly alkaline solutions. Sloped line is the expectation when  $Dy(OH)_3$  dissociates to  $Dy_{aq}^{3+}$  and  $OH$ .

It is clearly evident that the measured concentrations, for this research cannot be rationalized on the basis of the equilibrium between  $Dy(OH)_3$  with  $Dy_{aq}^{3+}$  and  $OH$  only.

The treatment attempting to quantify the formation of complex ions (akin to  $Li(OH)$  ion pairs) is presented in the next chapter. There were no measurements involving gadolinium leading to a figure similar to Figure 19. However, establishing a preliminary model for gadolinium, based on the chemical similarities of dysprosium, is explained further in the following chapter.

## CHAPTER 5 Thermodynamic Modelling of Solubility

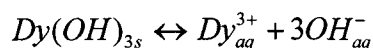
The following section is intended to lead to thermodynamic properties estimated for various dysprosium and gadolinium-containing species. It is expected that these properties will be used in conjunction with many other compounds in better understanding nuclear fuel chemistry, for the purposes of improved fuel design and reactor safety analysis. Accordingly, the ensuing sections are broken down into discussions pertaining to specific phases or species of dysprosium. Gadolinium will be presented subsequently.

### 5.1 Dysprosium Trihydroxide

As previously discussed in Chapter 2, the solubility product for dysprosium hydroxide can be expressed as

$$K_{sp} = [Dy_{aq}^{3+}][OH_{aq}^{-}]^3$$

To find the solubility product, both the dysprosium trivalent ion and hydroxide ion concentrations (molality), must be known at the onset of precipitation, while accounting for dilution effects on the  $Dy_{aq}^{3+}$ , associated with the introduction of the water in the lithium hydroxide solution. The solubility product was thus calculated to be  $7.8 \times 10^{-25}$ , evidence of extremely low solubility. Recalling the discussion in Chapter 2, the standard Gibbs energy of the precipitation reaction is related to the solubility product by Equation (10). Accordingly, the standard Gibbs energy change for



was found to be  $+137.6 \text{ kJ}\cdot\text{mol}^{-1}$ . The positive value is another way of expressing the very limited solubility of  $Dy(OH)_{3s}$ . Details on this calculation are to be found in Appendix C.

To be useful in computational processing by such procedures as Gibbs energy minimization, the Gibbs energy of formation from the elements is necessary. The thermodynamic data [33] for  $Dy_{aq}^{3+}$  and  $OH$  in aqueous solution appear in Table 6 and these properties are accepted in this development. It will be noted that in addition to the standard Gibbs energy of formation at 298 K that the enthalpy of formation, entropy and partial molar heat capacity are given. The Gibbs energy at any temperature can be derived from the latter three properties by methods discussed in Chapter 2. Experimental studies of  $Dy(OH)_{3s}$  solubility were performed only near 298 K. Accordingly, estimates of the entropy and heat capacity are required to complete the desired data set so that thermodynamic computations can, at a later time, be undertaken at any temperature, not just near 298 K. Table 5 cites properties for the solid hydroxides thought to be comparable to  $Dy(OH)_{3s}$ . The standard entropy has been reported for  $Dy(OH)_{3s}$ , of  $130.3 \text{ J}\cdot\text{K}^{-1}\cdot\text{mol}^{-1}$  [16]. This value is in reasonable agreement with the hydroxides shown in Table 5 and is accepted.

Table 5. Entropy and heat capacity comparison of various solid hydroxides.

Species	Approximate $S^{\circ}_{298K}$ ( $J \cdot K^{-1} \cdot mol^{-1}$ )	Approximate $C_p$ $_{298K}$ ( $J \cdot K^{-1} \cdot mol^{-1}$ )	Reference
Fe(OH) <sub>3s</sub>	104	101	[34]
Sc(OH) <sub>3s</sub>	100	114	[33],[35]
Al(OH) <sub>3s</sub>	71	93	[36]
Ga(OH) <sub>3s</sub>	100	113	[33],[35]

On the other hand the heat capacity for  $Dy(OH)_{3s}$  was estimated using Table 5 as a guide, and was selected to be  $115 J \cdot K^{-1} \cdot mol^{-1}$  at 298.15 K. Fortunately, when computations of equilibrium only are involved, the required Gibbs energy derived from these properties ( $H$ ,  $S$ ,  $C_p$ ) is insensitive to the heat capacity. This now leaves, in Table 6 below, only the value for the enthalpy of formation for  $Dy(OH)_{3s}$  to be determined. This was calculated in such a way as to provide the Gibbs energy for  $Dy(OH)_{3s}$  that the differences in Table 6,  $(-629.9+3(-226.7)-(-1448.0)) kJ \cdot mol^{-1}$  would equal the Gibbs energy change for the solubility product formulation given as  $(+137.6 kJ \cdot mol^{-1})$ .

Note in Table 6, the negative values of entropy and partial molar heat capacity for  $OH$ . These perhaps unexpected negative entries are to be understood as arising from the conventions associated with ions in water, stemming from the conventions of assigning zero to the partial molar heat capacity and entropy of hydrogen ion. Thus, for example, a negative partial molar heat capacity for an ion simply means that the heat capacity of the solution in which that ion is dissolved is lowered from that of otherwise pure water.

Table 6. Thermodynamic properties for dysprosium and related species.

Species	Phase	T min (K)	T max (K)	“Absolute” $G^{\circ}_{298K}$ (kJ·mol <sup>-1</sup> )	$\Delta H^{\circ}_{298K}$ (kJ·mol <sup>-1</sup> )	$S^{\circ}_{298K}$ (J·mol <sup>-1</sup> ·K <sup>-1</sup> )	$C_p$ (J·mol <sup>-1</sup> )
Dy	Solid	298	400	-22.3	0	74.9	28.1
Dy <sup>3+</sup>	Aqueous	298	300	-629.9	-698.7	-231.0	20.9
OH <sup>-</sup>	Aqueous	298	573	-226.7	-230.0	-10.9	-122.6
<i>Dy(OH)<sub>3</sub></i>	<i>Solid</i>	298	600	-1448.0	-1409.2	130.3	115

As a check on the properties of  $Dy(OH)_3$ , provided by Table 6, the titration curve up to the onset of precipitation (Chapter 4, Figure 14) was reproduced using Gibbs energy minimization software [29]. Calculations corresponding to various additions of lithium hydroxide solution are shown in Figure 20, Figure 21, and Figure 22. The beginning of the neutralization of nitric acid is shown in Figure 20; the onset of precipitation of  $Dy(OH)_3$  is shown below in Figure 21; the progression of precipitation following the continued introduction of lithium hydroxide solution is shown in Figure 22.

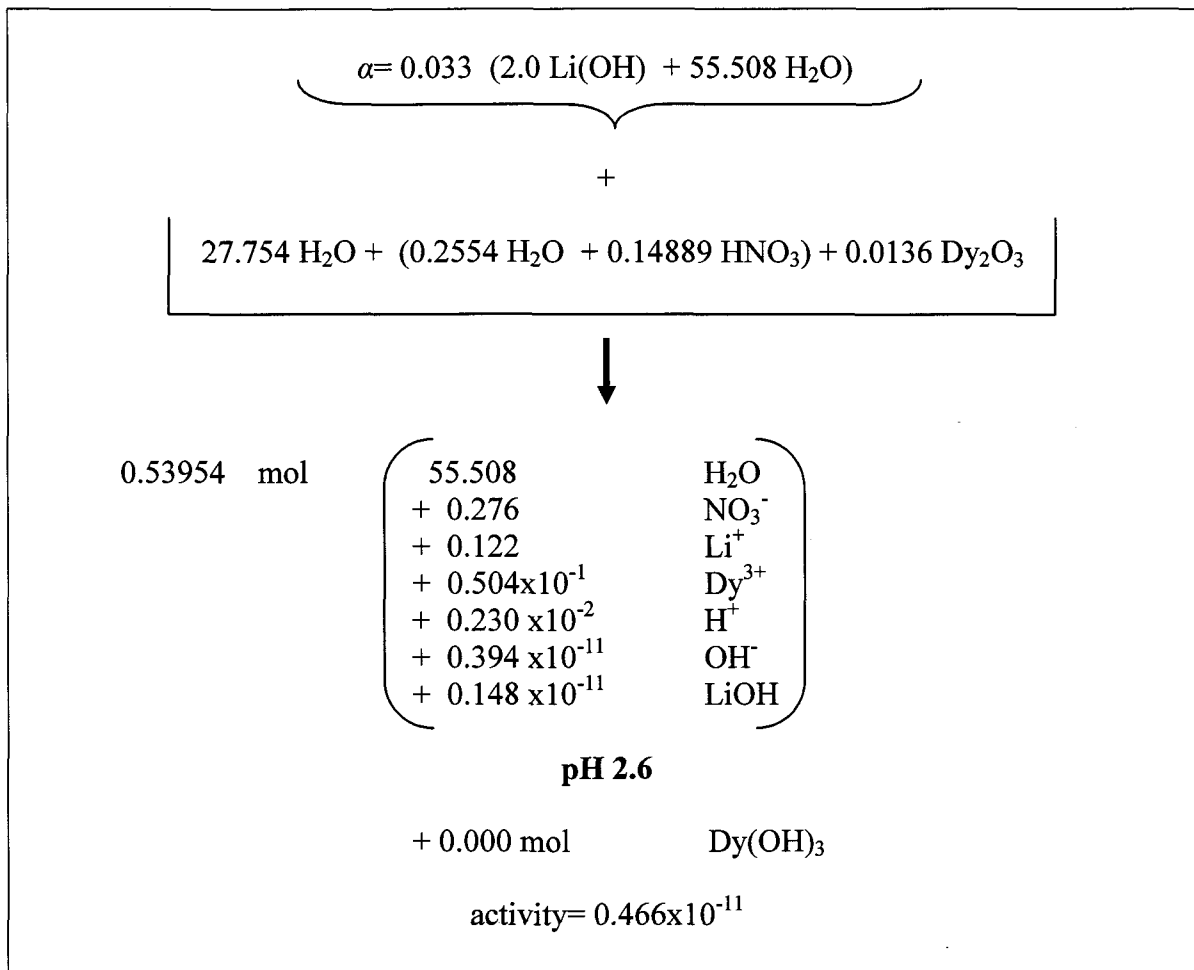


Figure 20. Gibbs energy minimization computation at 297.15 K for a value of  $\alpha = 0.033$  offered as evidence that the thermodynamic properties introduced for  $\text{Dy(OH)}_3$  replicate the measurements recorded in Figure 23.

Consider Figure 20, the first lines represent the standard lithium hydroxide solution. This is presented as moles of lithium hydroxide in relation to 55.508 mols of water (1 kg). Accordingly, the entry is to be understood as a 2 molal solution of lithium hydroxide. The value of  $\alpha$  represents the quantity of this solution being added to the dysprosium containing acid solution. Strictly speaking,  $\alpha$  is the number of liters of water introduced, however, in consideration of the density of a 2 molar lithium hydroxide solution ( $1.05 \text{ g}\cdot\text{ml}^{-1}$ ) and the mass fraction of water in that milligram (0.954), the factor  $\alpha$ , is very

nearly to be understood as liters of lithium hydroxide solution added to the water. The overall composition of the system (contents of the beaker before the lithium hydroxide solution is added) is shown on the second line with symbolism to associate this with the beaker.

The computed output shown below the symbol ↓ represents the concentration and redistribution of elements associated with the most stable chemical state. This is the state otherwise described as the products of a balanced chemical equation (when the most stable product species determination is part of the computation). The product number of moles of water has been normalized (by 0.53902) so that the mole numbers preceding the aqueous solutes can be seen in relation to 55.508 mols of water (1 kg). In this way, the concentration, for example of nitrate ion, can be recognized as being 0.276 molal. It is evident, from the negative logarithm of the computed molality of  $H^+$ , that the pH is 2.6, insufficient to precipitate dysprosium hydroxide. Accordingly, the solid hydroxide shown at the very bottom of Figure 20 has an activity far less than one and does not appear as a phase (0.000 mols).

In Figure 21 the addition of lithium hydroxide solution has been increased by approximately 1 ml, bringing the pH to 6.4 as experimentally measured when precipitation begins. Dysprosium hydroxide is now at the threshold of precipitation (solubility product satisfied).



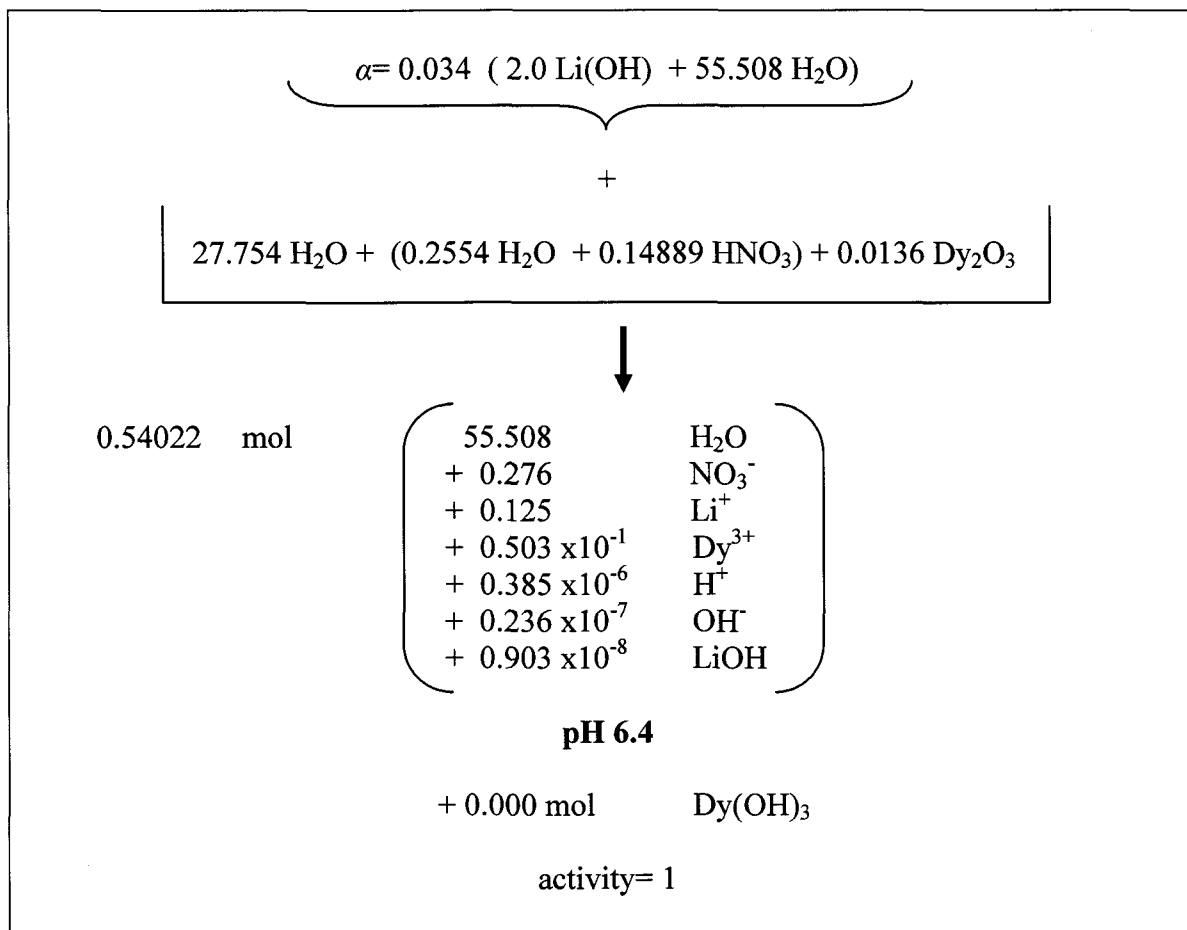


Figure 21. Gibbs energy minimization computation at 297.15 K for a value of  $\alpha = 0.034$  offered as evidence that the thermodynamic properties introduced for  $\text{Dy(OH)}_{3,s}$  replicate the measurements recorded in Figure 23.

Figure 22 shows a further addition of lithium hydroxide solution (value of  $\alpha$  increasing to 0.038) leading to significant precipitation of  $\text{Dy(OH)}_{3,s}$  and a concurrent reduction in the dissolved dysprosium ion concentration. The precipitation of dysprosium hydroxide has a strong buffering effect.

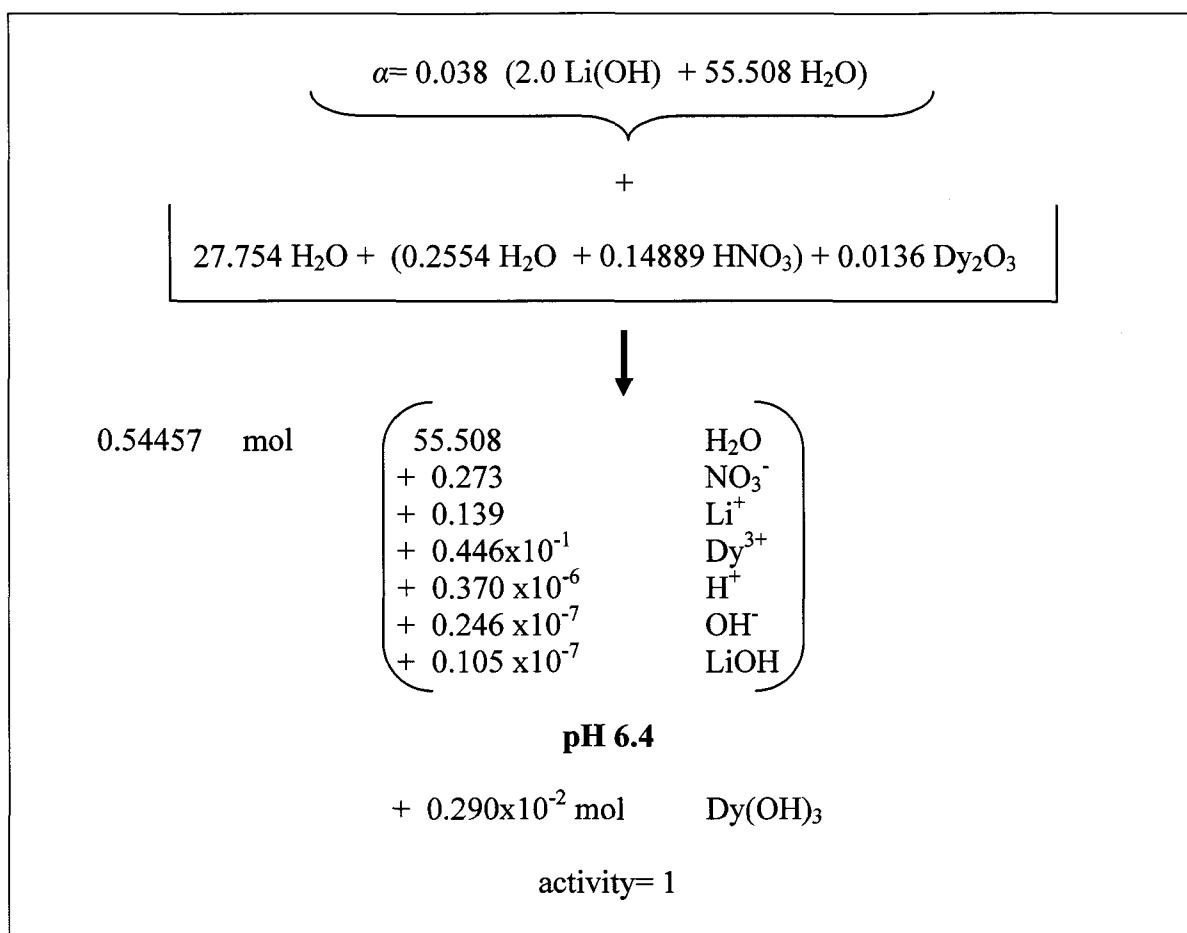


Figure 22. Gibbs energy minimization computation at 297.15 K for a value of  $\alpha = 0.038$  offered as evidence that the thermodynamic properties introduced for  $\text{Dy(OH)}_3$  replicate the measurements recorded in Figure 23.

By a repetition of the calculations in Figure 20, Figure 21 and Figure 22, making the slight correction to recognize the distinction between “ $\alpha$ ” and liters of  $\text{LiOH}$  solution added, the entire titration curve can be constructed and compared with the experimental one. This comparison is shown in Figure 23. Specific points connected to Figure 20, Figure 21 and Figure 22 are identified in Figure 23.

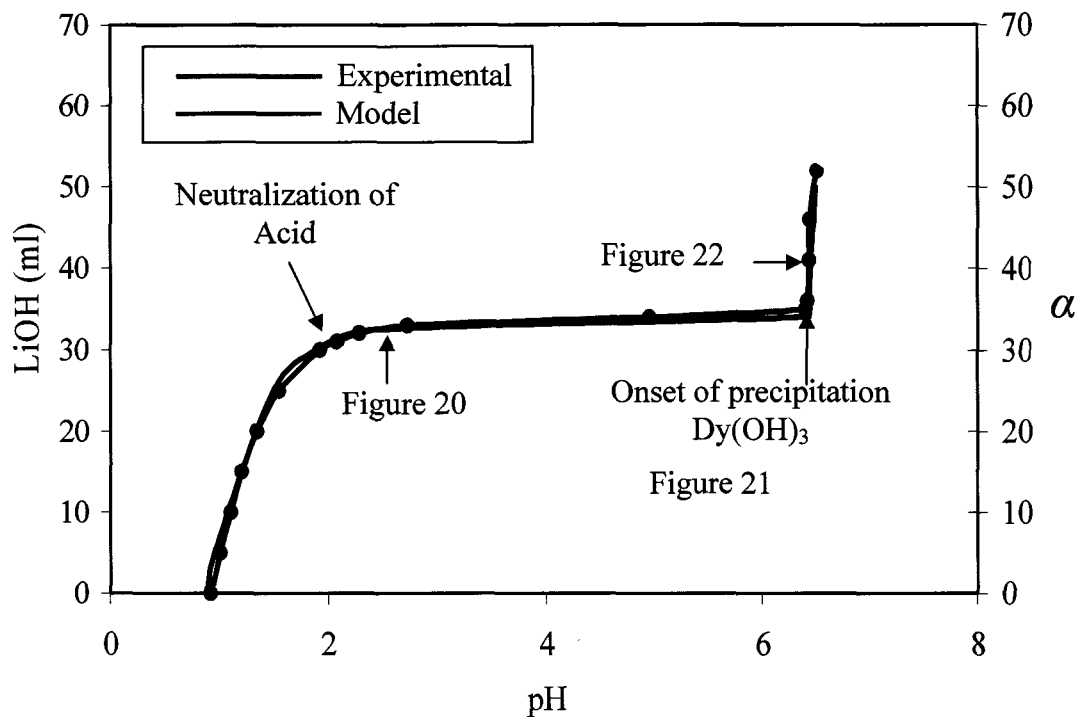


Figure 23. Modelling comparison to solubility product experiment offered as evidence in support of the thermodynamic properties for dysprosium hydroxide given in Table 6.

## 5.2 Dysprosium Monohydrate

Thermogravimetric analytical work on  $Dy(OH)_3$ , discussed in Chapter 4 indicated the presence of an intermediate stable monohydrate developing at elevated temperatures. By methods comparable to those discussed in relation to  $Dy(OH)_3$ , the thermodynamic properties of  $DyO(OH)$  were inferred to be in approximate accord with the experimental observations. The proposed properties appear in Table 7.

Table 7. Thermodynamic data for dysprosium oxides and hydrates.

Component	Phase	$\Delta H^{\circ}_{298K}$ (kJ·mol <sup>-1</sup> )	$S^{\circ}_{298K}$ (J·K <sup>-1</sup> ·mol <sup>-1</sup> )	$C_p$ (J·K <sup>-1</sup> ·mol <sup>-1</sup> )
<i>Dy(OH)<sub>3s</sub></i>	<i>Solid</i>	<i>-1409.2</i>	<i>130.3</i>	<i>115</i>
<i>DyO(OH)<sub>s</sub></i>	<i>Solid</i>	<i>-1084.0</i>	<i>120</i>	<i>100</i>
<i>Dy<sub>2</sub>O<sub>3</sub></i>	<i>Solid</i>	<i>-1863.1</i>	<i>149.8</i>	<i>115.4</i>

\*Estimates in italics

The information in Table 7 is sufficient to generate a phase diagram showing the approximate relationship between water vapour pressure and temperature as it is related to the stability of the compounds. The computed phase diagram is shown in Figure 24.

Examining Figure 24, it can be seen that the two downward sloping lines represent equilibrium boundaries separating the domains of  $Dy_2O_{3s}$  on the left and below, from  $DyO(OH)_s$  crossing the middle of the diagram and  $Dy(OH)_{3s}$  appearing on the upper right. The temperature scale on the bottom is  $1/T$  making the temperature scale increase from right to left on the logarithmic plot. The blue line (upper boundary) represents the equilibrium between  $Dy(OH)_{3s}$  and  $DyO(OH)_s$ , while the red line (lower boundary) represents the phase boundary between  $DyO(OH)_s$  and  $Dy_2O_{3s}$ . From Figure 24, for conditions of 1 atm partial pressure  $H_2O$ ,  $Dy(OH)_{3s}$  decomposes to  $DyO(OH)_s$  at an approximate temperature of 463 K. On continued heating, Figure 24 implies that decomposition of  $DyO(OH)_s$  to the anhydrous oxide occurs at about 700 K. Thermodynamic computations of these two transitions are shown in Appendix D. At lower partial pressures of water vapour, the same decomposition processes occur at lower

temperatures. Results from TGA experiments and this proposed equilibrium diagram cannot be quantitatively related because the partial pressure of  $H_2O$  was not controlled in this equipment. Nevertheless, the build up in the equilibrium partial pressure of  $H_2O$  on heating that can be inferred from the diagram (move upward to the left along the phase boundaries) gives a qualitative indication of the expected loss of water vapour. This understanding may be likened to the rapid evaporation of water at temperatures as the normal boiling point is approached on heating.

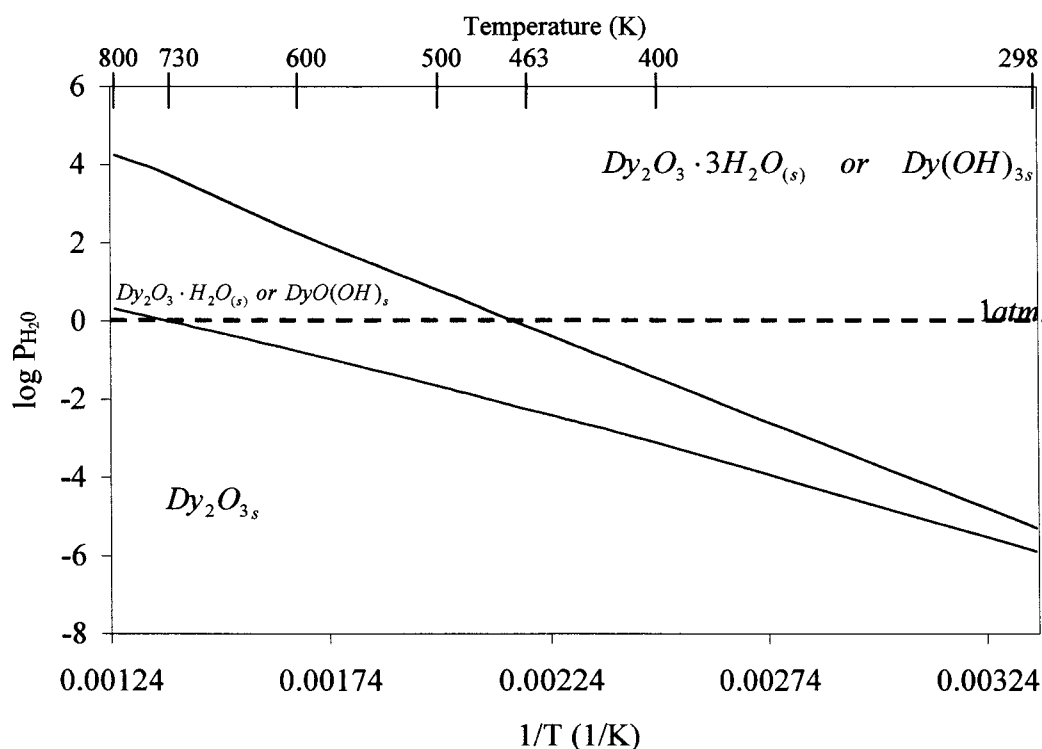
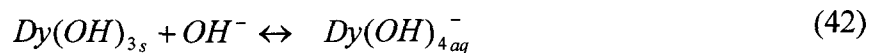
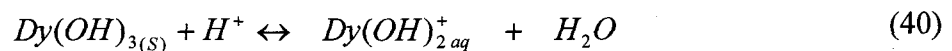
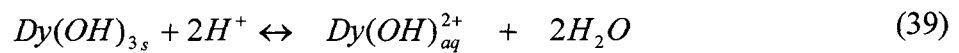


Figure 24. Proposed phase diagram for the stability of dysprosium oxide hydrates qualitatively consistent with thermogravimetric experiments.

### 5.3 Complex Ions

As concluded in the discussion of the solubility measurements made in highly alkaline solutions, the experimental findings cannot be rationalized solely on the basis of  $Dy_{aq}^{3+}$ , controlled by the solubility product of  $Dy(OH)_{3s}$ . Accordingly, it was necessary to introduce additional chemical species involving  $Dy_{aq}^{3+}$  and hydroxide ions as previous experimental work claims is necessary [17]. In this section, it is proposed that in addition to the  $Dy(OH)_{4aq}^-$  complex ion [17], three other complex species may form. These are  $Dy(OH)_{aq}^{2+}$ ,  $Dy(OH)_{2aq}^+$ , and  $Dy(OH)_{3aq}$ . For the present purposes, it is necessary to infer the Gibbs energies of formation of these complex ions in such a way as to resonate with the experimental solubility measurements. The intention is to produce a set of thermodynamic properties that could be used for the general modelling purposes, as previously mentioned. Therefore, following the practice for the compounds previously discussed, the enthalpy for each complex ion must be estimated. The enthalpy of formation is then adjusted to provide Gibbs energies that generate equilibrium constants for



in order to collectively provide the total concentration of dissolved dysprosium, in a saturated solution.

In view of the foregoing assumptions, the partial molar heat capacity for each species was set to zero. As previously mentioned, the heat capacity has very little effect on the computation of Gibbs energies, and in particular on the way the Gibbs energy projects to temperatures above 298 K [19]. This is not to say that a heat capacity for these complex ions do not exist, as every species has an associated specific heat capacity related to the energy required to raise the temperature of that species one unit. However, for ions these values can be negative or positive based on the contribution effect that they have on pure water (i.e. raising or lowering the heat capacity of water). Regarding the temperature regions of interest for this research (298 K- 550 K) the heat capacity has only a minimal contribution to the overall Gibbs energy expression when a comparison is made at these temperature values.

The entropies ( $S^{\circ}_{298\text{K}}$ ) for the complexes were chosen based on trends from other aqueous ionic species. For example, a comparable species was found to form multiple complex ions similar to the formation of the proposed complexes of dysprosium. This is shown in Table 8.

Table 8. Comparison of trending entropy as a function of hydroxide group addition.

Species (Indium)	Entropy $J \cdot K^{-1} \cdot mol^{-1}$	Reference
$In^{3+}$	-150.624	[37]
$In(OH)^{2+}$	-87.864	[37]
$In(OH)_2^+$	25.104	[37]

Dysprosium complex ion entropy estimations were therefore made to increase by  $100 J \cdot K^{-1} \cdot mol^{-1}$  for each subsequent hydroxide addition. The enthalpy of formation was then adjusted iteratively and the resulting effect on the calculated solubility was compared with the NAA measurements. In view of the systematic pattern of estimated entropies, it was decided to maintain a comparable systematic pattern for the estimated enthalpies of formation of  $Dy(OH)_n^{3-n}$ , guided by the expression below

$$\frac{[\Delta H_{\text{Complex hydroxyl}} - \Delta H_{Dy^{3+}}]}{(n)_{\text{hydroxylcomplex}}} \approx \text{constant} \quad (43)$$

A typical set of estimated thermodynamic properties for dysprosium complex ions can be seen in Table 9.

Table 9. First estimate for dysprosium aqueous complex ions.

Component	Phase	$\Delta H_{298K}^{\circ}$ ( $J \cdot mol^{-1}$ )	$S_{298K}^{\circ}$ ( $J \cdot K^{-1} \cdot mol^{-1}$ )	$C_p$ ( $J \cdot K^{-1} \cdot mol^{-1}$ )
$Dy^{3+}_{aq}$	Aqueous	-698728	-230.956	20.92
<i><math>Dy(OH)^{2+}_{aq}</math></i>	<i>Aqueous</i>	<i>-922121</i>	<i>-130</i>	<i>0</i>
<i><math>Dy(OH)_2^+_{aq}</math></i>	<i>Aqueous</i>	<i>-114514</i>	<i>-30</i>	<i>0</i>
<i><math>Dy(OH)_3_{aq}</math></i>	<i>Aqueous</i>	<i>-1368907</i>	<i>70</i>	<i>0</i>
<i><math>Dy(OH)_4^-_{aq}</math></i>	<i>Aqueous</i>	<i>-1592300</i>	<i>170</i>	<i>0</i>

\*Estimates in italics.

Using the estimates in Table 9, the concentration of each complex ion coexisting with  $Dy(OH)_3_s$  solid was computed. Then, the total dysprosium molality of all the



dysprosium containing ions in water was summed. The resultant total molality is plotted as a function of pH in Figure 25. The findings are shown in relation to the NAA measurements, as well as the concentration that would be expected if  $Dy(OH)_3$  dissolved only to give  $Dy_{aq}^{3+}$  ions. It is apparent that complex ion formation can account for the greater than expected solubility, but the selection of properties for the first estimate fails to generate all measured concentrations.

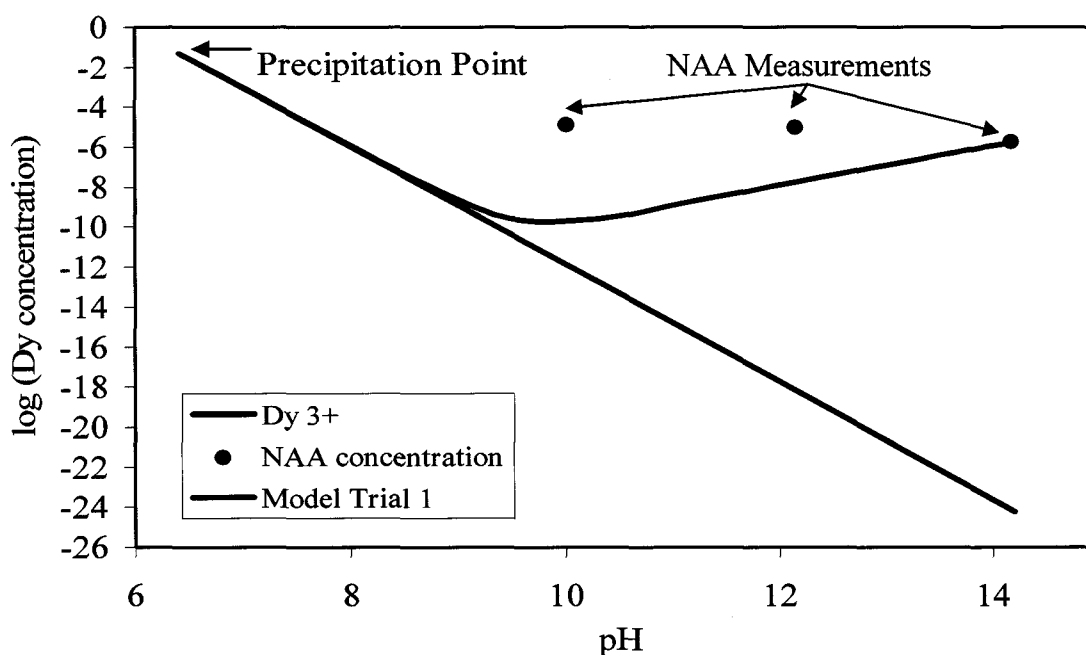


Figure 25. First attempt at modelling solubility in highly alkaline solutions based upon the estimated thermodynamic properties of complex ions given in Table 9.

A second attempt was therefore made (by adjusting enthalpy values *guided* by Equation (43)) retaining a systematic set of thermodynamic properties for the complex ions. This is shown in Table 10. The consequences on the calculated solubility are evident in Figure 26 with the modeled behaviour showing improvements when compared to the first attempt.

Table 10. Second estimate for dysprosium aqueous complex ions.

Component	Phase	$\Delta H^{\circ}_{298K}$ ( $J \cdot mol^{-1}$ )	$S^{\circ}_{298K}$ ( $J \cdot K^{-1} \cdot mol^{-1}$ )	$C_p$ ( $J \cdot K^{-1} \cdot mol^{-1}$ )
$Dy^{3+}_{aq}$	Aqueous	-698728	-230.956	20.92
$Dy(OH)^{2+}_{aq}$	<i>Aqueous</i>	<i>-920000</i>	<i>-130</i>	<i>0</i>
$Dy(OH)^{+}_{2aq}$	<i>Aqueous</i>	<i>-1150000</i>	<i>-30</i>	<i>0</i>
$Dy(OH)^{0}_{3aq}$	<i>Aqueous</i>	<i>-1390000</i>	<i>70</i>	<i>0</i>
$Dy(OH)^{-}_{4aq}$	<i>Aqueous</i>	<i>-1590000</i>	<i>170</i>	<i>0</i>

\*Estimates in italics.

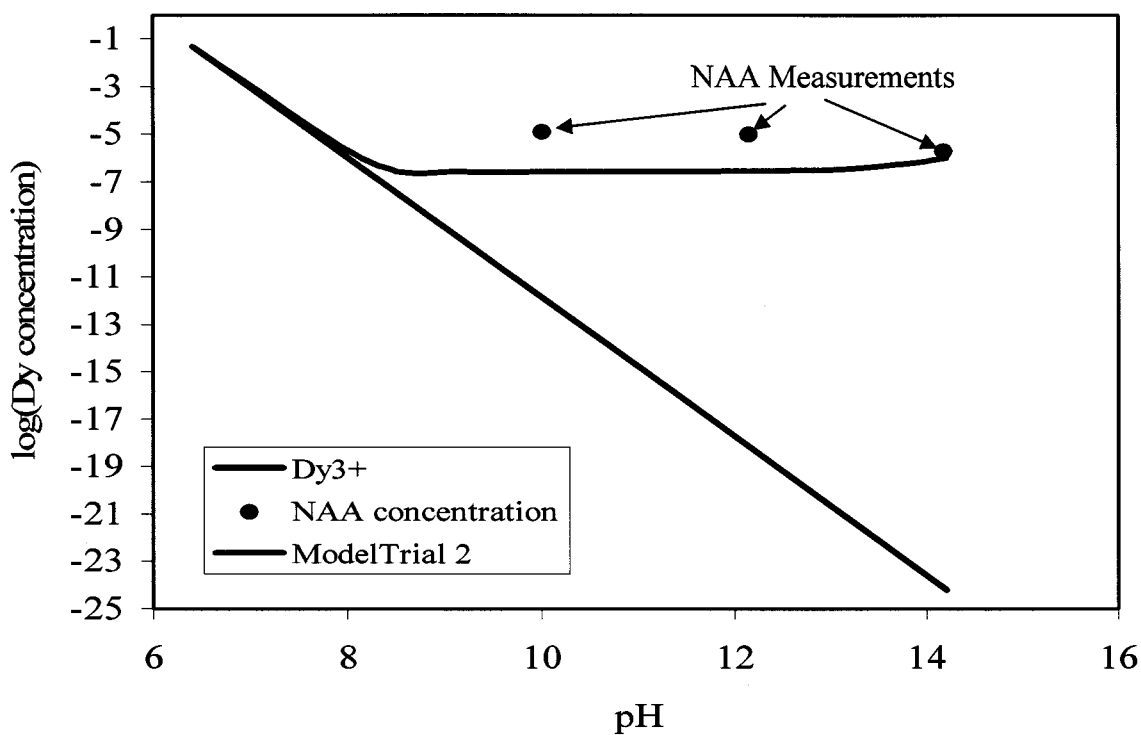


Figure 26. Second attempt at modelling solubility in highly alkaline solutions based upon the estimated thermodynamic properties of complex ions given in Table 10.

A final set of properties was selected for the series of complex ions as given in Table 11. The effect of these estimates on the solubility is shown in Figure 27. In view of the limited number of measurements and in particular their precision, further adjustments to better represent the solubility was not thought to be justified.

Table 11. Final estimate for dysprosium aqueous complex ions.

Component	Phase	$\Delta H^{\circ}_{298K}$ ( $J \cdot mol^{-1}$ )	$S^{\circ}_{298K}$ ( $J \cdot K^{-1} \cdot mol^{-1}$ )	$C_p$ ( $J \cdot K^{-1} \cdot mol^{-1}$ )
$Dy^{3+}_{aq}$	Aqueous	-698728	-230.956	20.92
$Dy(OH)^{2+}_{aq}$	<i>Aqueous</i>	<i>-920000</i>	<i>-130</i>	<i>0</i>
$Dy(OH)^{+}_{2aq}$	<i>Aqueous</i>	<i>-1150000</i>	<i>-30</i>	<i>0</i>
$Dy(OH)^{0}_{3aq}$	<i>Aqueous</i>	<i>-1395000</i>	<i>70</i>	<i>0</i>
$Dy(OH)^{-}_{4aq}$	<i>Aqueous</i>	<i>-1590000</i>	<i>170</i>	<i>0</i>

\*Estimates in italics.

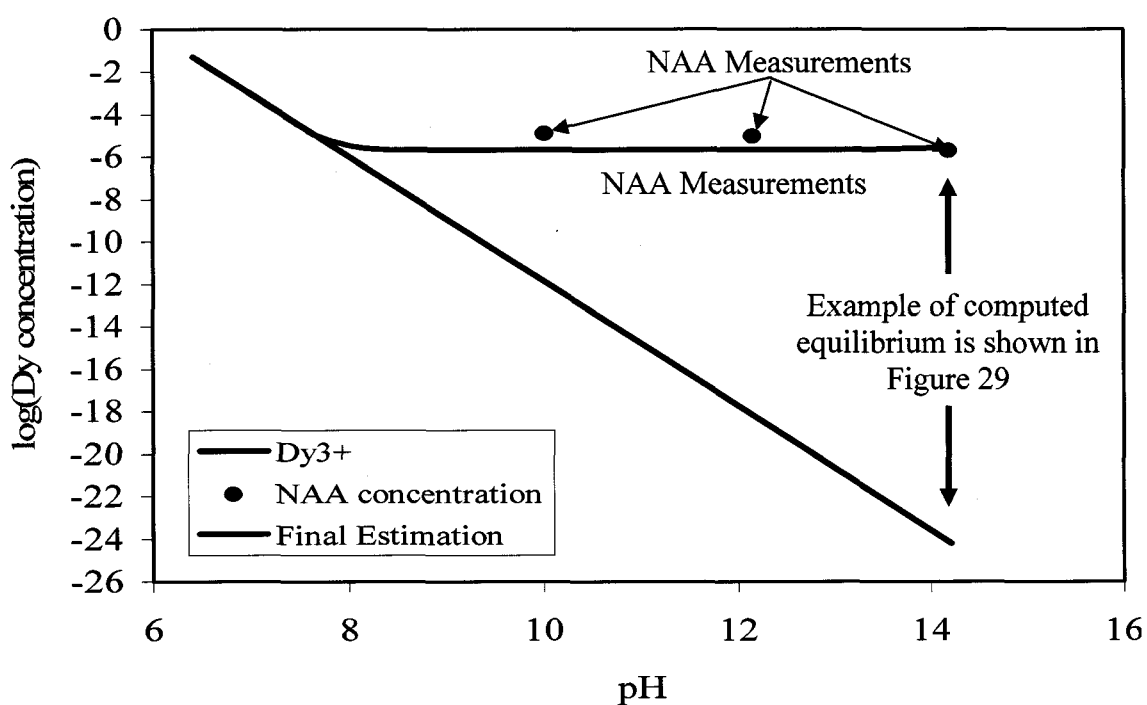


Figure 27. Final attempt at modelling solubility in highly alkaline solutions based upon the estimated thermodynamic properties of complex ions given in Table 11.

The variation in the enthalpy of formation in Table 11 is plotted in Figure 28 where it is evident that the supposition embodied in the constraints of Equation (43) are satisfied.

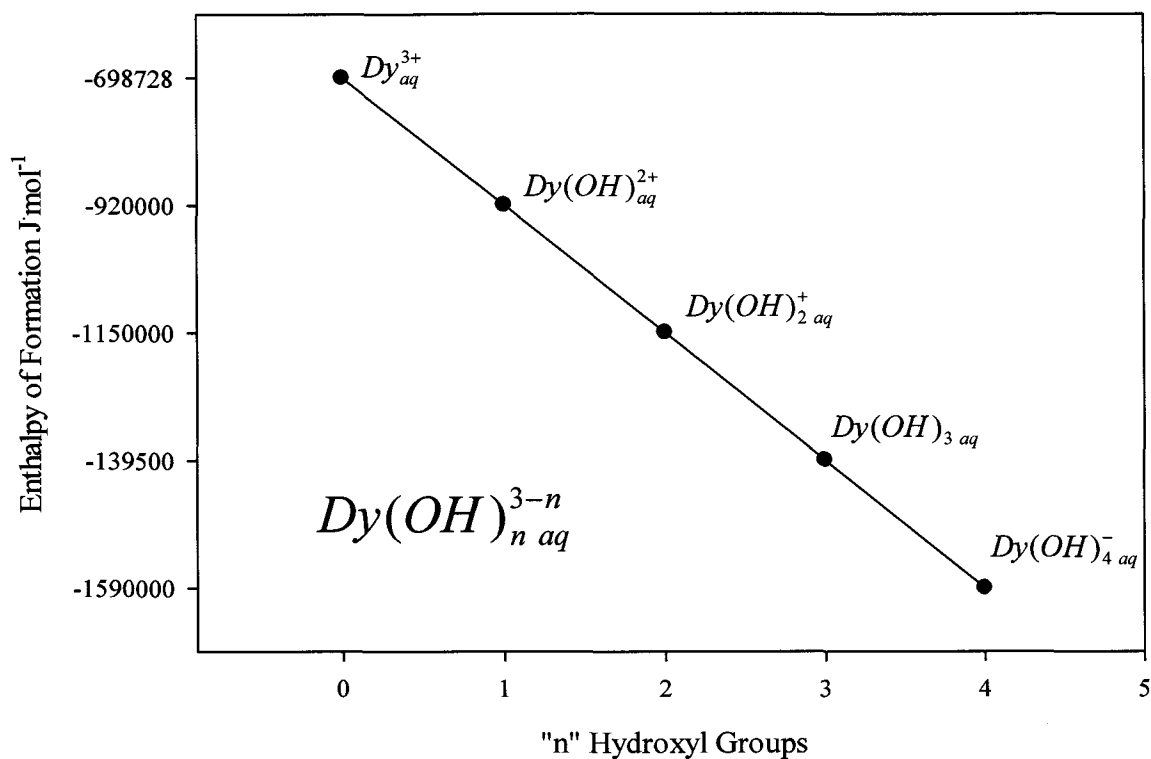


Figure 28. Linear enthalpy trends for final estimations made for complex ions.

Following the output associated with the use of thermodynamic data in Gibbs energy minimization computations, as shown previously in Figure 20, Figure 21 and Figure 22, Figure 29 was constructed. Figure 29 illustrates a solubility calculation of  $Dy(OH)_3$  in solutions of very high alkalinity, where there is competition for the hydroxide ions between  $Li^+$  to form  $LiOH$  ion pairs and  $Dy^{3+}_{aq}$  to form  $Dy(OH)^-_{4 aq}$ , along with other dysprosium hydroxide complexes becomes important.

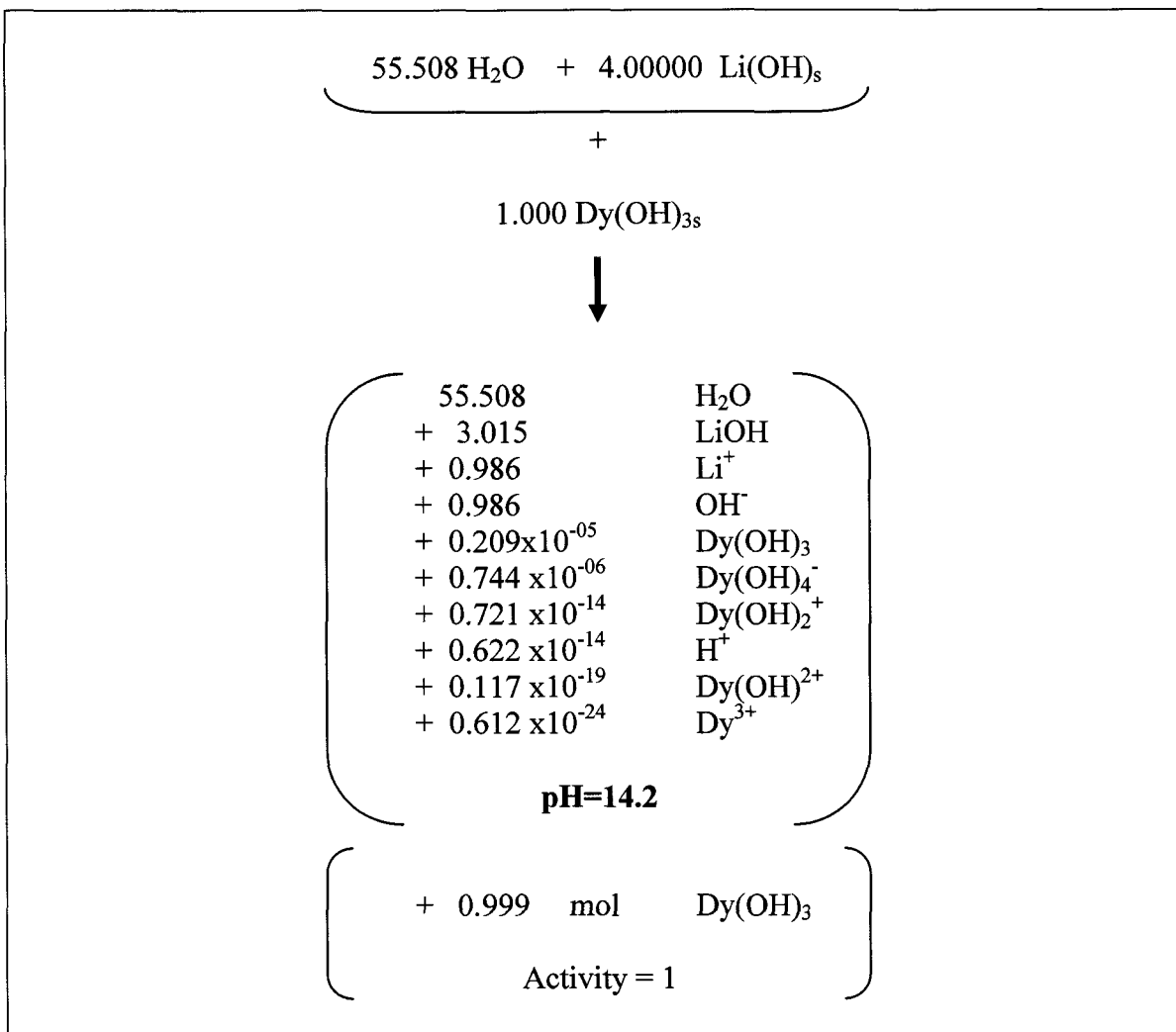


Figure 29. Computed equilibrium at 298 K representative of position marked in Figure 27.

Among the significant matters evident in Figure 29 is the high concentration of  $\text{LiOH}$  ions affecting the population of free hydroxide ions and the effect on the pH. The dominant dysprosium containing species in the water are the  $\text{Dy(OH)}_{3\text{ aq}}$  and  $\text{Dy(OH)}_{4\text{ aq}}^-$ . The combined molality of these two ions ( $\sim 2.8 \times 10^{-6}$ ) is, for practical purposes, solely responsible for the dissolution of  $\text{Dy(OH)}_{3\text{ s}}$ . The computed concentration of free  $\text{Dy}_{\text{aq}}^{3+}$  is extremely low and may be understood in reference to Figure 27.

The output in Figure 29 shows that the dissolution of  $Dy(OH)_3$ , in a concentrated lithium hydroxide solution, could not be expressed by observing the disturbing effect on pH, as the equilibrium (previously mentioned in Chapter 2) for these proposed complexes might suggest. The concentration of all forms of dissolved dysprosium are simply too low to significantly disturb the concentration of hydroxide ions, in terms of its ability to be measured (logarithmically) on the pH scale. Initial attempts to undertake studies of this type (before the very low solubility was established) proved unsuccessful in terms of the precision with which pH could be measured. Further attempts at precipitating  $Dy(OH)_3$  from the saturated solution, (similar to that represented in the calculations in Figure 29) by acidifying the supernatant solution, failed to show any cloudiness. This added further indication that the solubility is extremely low even in strongly alkaline solutions.

#### 5.4 Dysprosia Additions to Pure Water

The aforementioned interpretation of the solubility of  $Dy_2O_3$  implies that the surface of  $Dy_2O_3$  converts to trihydroxide and the solubility is controlled by the equilibrium of that phase with ions or complex hydroxide ions of dysprosium. This matter merits some consideration. Figure 30, Figure 31 and Figure 32 are computations of the pH resulting from forced equilibrium with  $Dy_2O_3$ ,  $DyO(OH)$ , and  $Dy(OH)_3$ , respectively. In the computations, the desired phase constraint is imposed by withdrawing the two solid phases not to be considered.

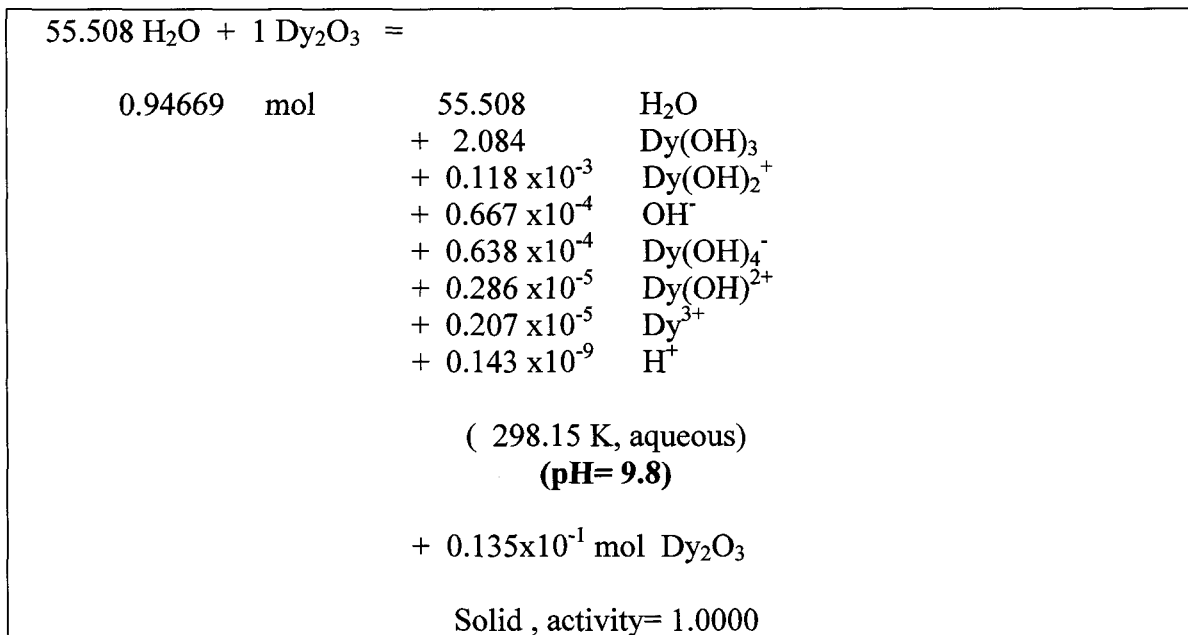


Figure 30. Aqueous equilibrium in the supposition that  $\text{Dy}_2\text{O}_3, s$  coexists with aqueous solution.

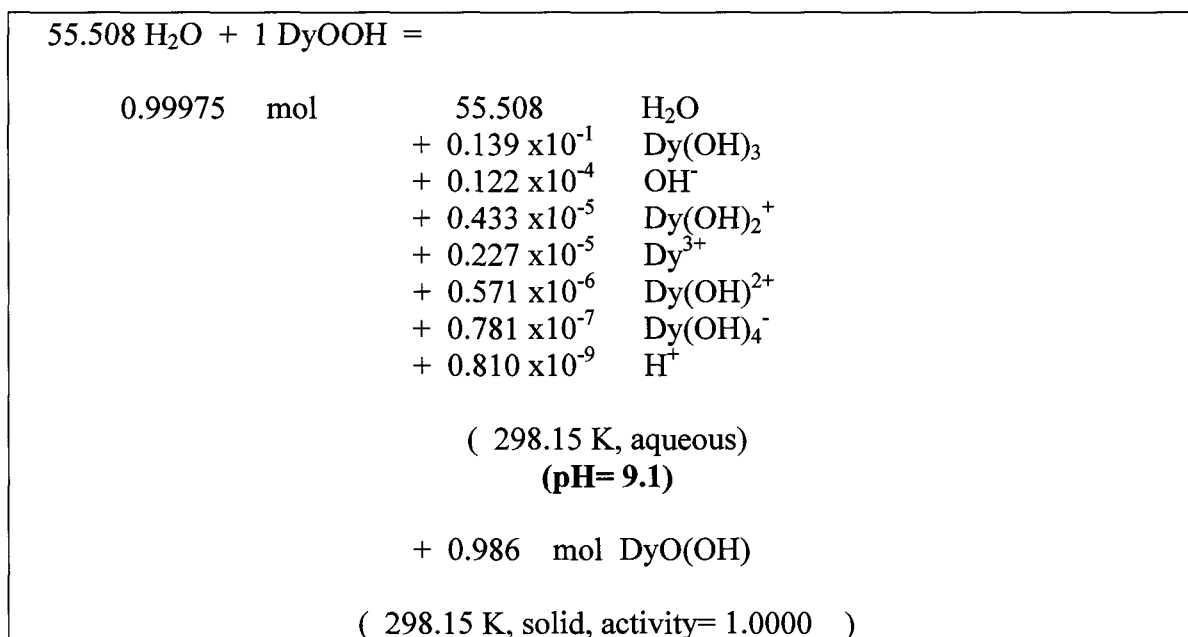


Figure 31. Aqueous equilibrium in the supposition that  $\text{DyO(OH)}_s$  coexists with aqueous solution.

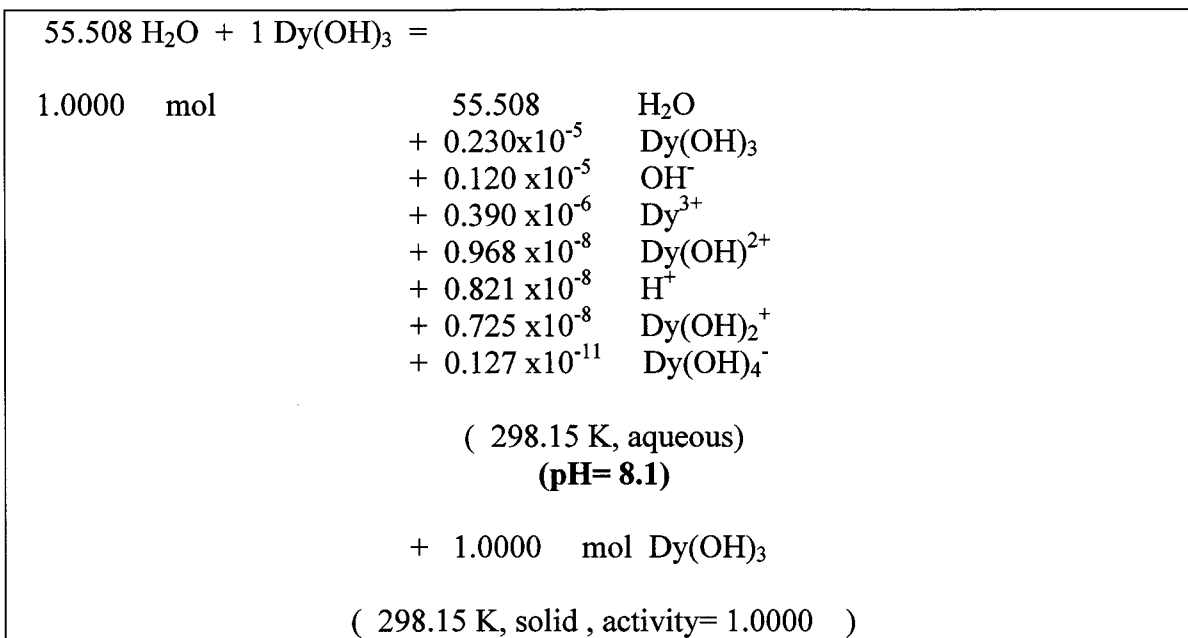


Figure 32. Aqueous equilibrium in the supposition that  $\text{Dy(OH)}_{3,s}$  coexists with aqueous solution.

Direct measurements of the pH of initially distilled water, after dysprosium oxide powder was left in contact with the solution for several hours under hydrogen gas cover (to prevent minor pH disturbance by  $\text{CO}_2$  dissolution from the air), gave a pH of 7.7. Although at this pH very minor concentrations of impurities can disturb the value, the observation is nearest the pH computation involving  $\text{Dy(OH)}_{3,s}$  (Figure 32). In particular, it is not possible to account for a pH as high as those calculated on the supposition that  $\text{DyO(OH)}_s$  (Figure 31) or  $\text{Dy}_2\text{O}_{3,s}$  (Figure 30) is controlling the solubility and the consequent disturbance of the pH. The extent of trihydroxide formation on the surface of  $\text{Dy}_2\text{O}_{3,s}$  is expected to be very limited. Long term exposure of  $\text{Dy}_2\text{O}_{3,s}$  to water followed by evaporation to dryness does not result in water absorption associated with 3 mols of water chemically combined with all of the  $\text{Dy}_2\text{O}_{3,s}$  added. Of course, during the precipitation from acidic aqueous solution in the experiments involving the addition of



lithium hydroxide, precipitation entirely as  $Dy(OH)_3$  is understandable because component ions ( $Dy_{aq}^{3+}$  and  $OH_{aq}^-$ ) can associate on the atomic scale during the process of crystallization from solution.

### 5.5 Computed Pourbaix Diagrams for Dysprosium at 298 K

Updated Pourbaix diagrams for the solubility of dysprosium oxide have been computed using the thermodynamic properties proposed in the previous section. Pourbaix diagram construction method is described in the Uhlig Corrosion Handbook [38]. The updated diagrams are shown below for concentrations of dysprosium aqueous species of  $10^0$ ,  $10^{-2}$ ,  $10^{-4}$ , and  $10^{-5}$  molal. The diagram at 1 molal ( $10^0$ ) concentration is very much like the one appearing in Pourbaix's Atlas in Figure 12. The overlay of the diagram at  $10^{-4}$  appears on the same figure in the style of Pourbaix. The diagram at  $10^{-6}$  molal is different when the  $Dy(OH)_3$  field is recognised not to be a solid hydroxide but rather a neutral aqueous species. There is also the matter of the intrusion of the  $Dy(OH)_4^-$  on the extreme right of the diagram. Although the computed Pourbaix diagrams resemble the literature, they have been appropriately adjusted to reflect the inclusion of aqueous complex ions of dysprosium.

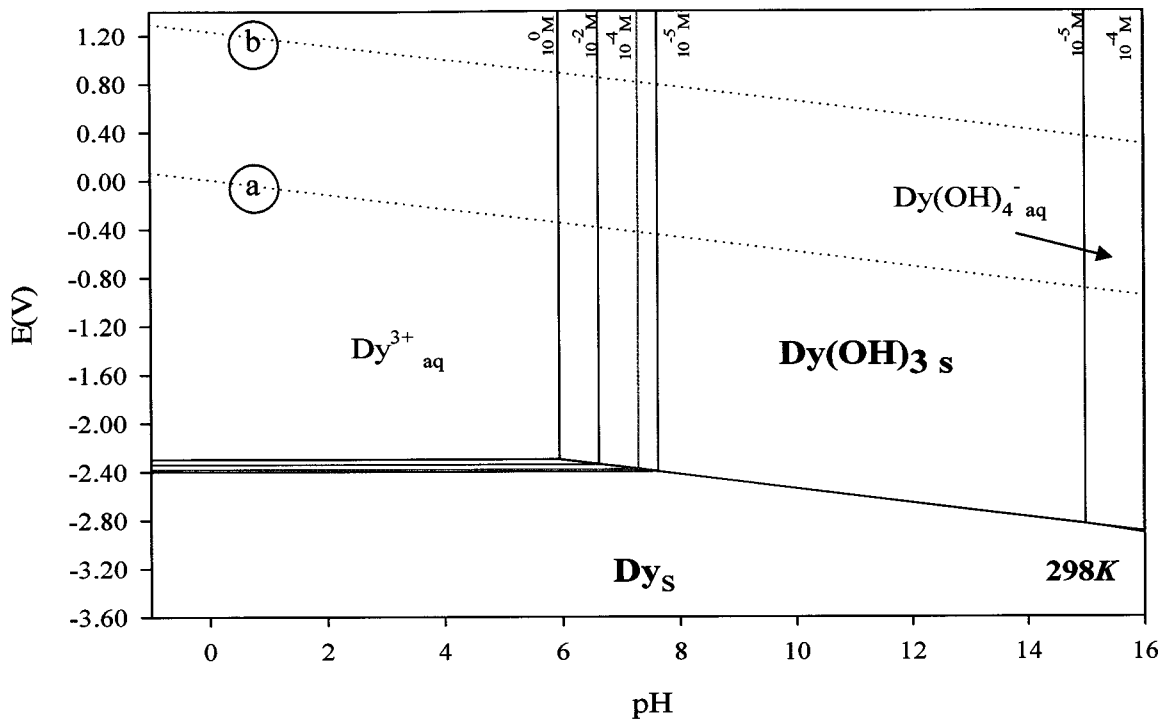


Figure 33. Calculated Pourbaix diagram for dysprosium at 298 K, for aqueous concentrations of 1,  $10^{-2}$ ,  $10^{-4}$ , and  $10^{-5}$  molal.

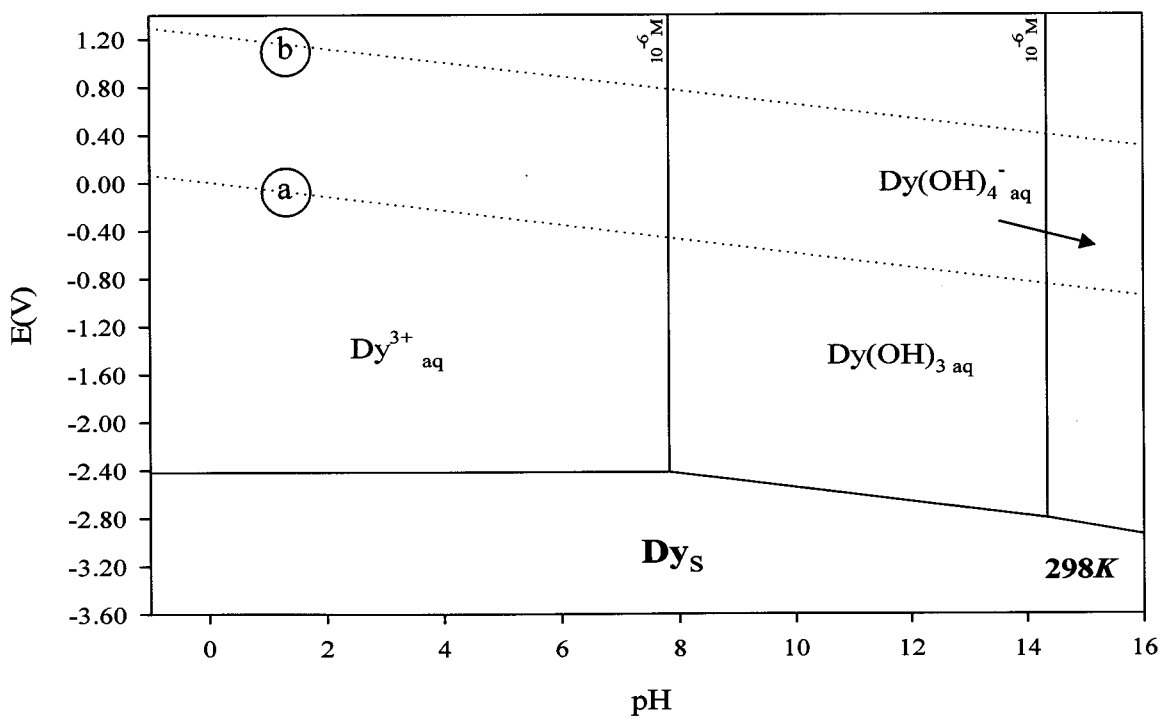


Figure 34. Calculated Pourbaix diagram for dysprosium at 298 K, for an aqueous concentration of  $10^{-6}$  molal

## 5.6 Solubility Model for Gadolinia

The processes for establishing estimates of complex ions and compounds of gadolinium were performed in accordance with the comparable treatment for dysprosium. Shown below in Table 12 are the estimated thermodynamic properties for gadolinium species.

Table 12. Final estimate for gadolinium aqueous complex ions and solid phases.

Component	Phase	$\Delta H^{\circ}_{298K}$ ( $J \cdot mol^{-1}$ )	$S^{\circ}_{298K}$ ( $J \cdot K^{-1} \cdot mol^{-1}$ )	$C_p$ ( $J \cdot K^{-1} \cdot mol^{-1}$ )
$Gd^{3+}_{aq}$	Aqueous	-684502	-205.853	-19.674
<i><math>Gd(OH)^{2+}_{aq}</math></i>	<i>Aqueous</i>	<i>-905774</i>	<i>-105</i>	<i>0</i>
<i><math>Gd(OH)_2^{+}_{aq}</math></i>	<i>Aqueous</i>	<i>-1127046</i>	<i>-5</i>	<i>0</i>
<i><math>Gd(OH)_3_{aq}</math></i>	<i>Aqueous</i>	<i>-1348318</i>	<i>95</i>	<i>0</i>
<i><math>Gd(OH)_4^{-}_{aq}</math></i>	<i>Aqueous</i>	<i>-1569590</i>	<i>195</i>	<i>0</i>
<i><math>GdO(OH)_s</math></i>	<i>Solid</i>	<i>-1066000</i>	<i>120</i>	<i>100</i>
$Gd_2O_3_s$	Solid	-1819621.9	156.9	106.6
<i><math>Gd(OH)_{3s}</math></i>	<i>Solid</i>	<i>-1396000</i>	<i>126.6</i>	<i>91.1</i>

\*Estimates in italics.

As for dysprosium, the solubility product for  $Gd(OH)_3_s$  was experimentally determined and can be seen in Appendix E. Thermogravimetric analysis for the precipitate of gadolinium was also conducted. Thermodynamic computations representative of the decomposition of gadolinium hydroxide to the hydrous oxide and subsequent anhydrous oxide can be seen in Appendix F. Pourbaix diagrams for the gadolinium-water system at 298 K can be seen below in Figure 35 and Figure 36. These have been constructed with the inclusion of complex ions of gadolinium, which appear to show a predominant domain of stability between the very low molalities of  $10^{-4}$  and  $10^{-6}$ .

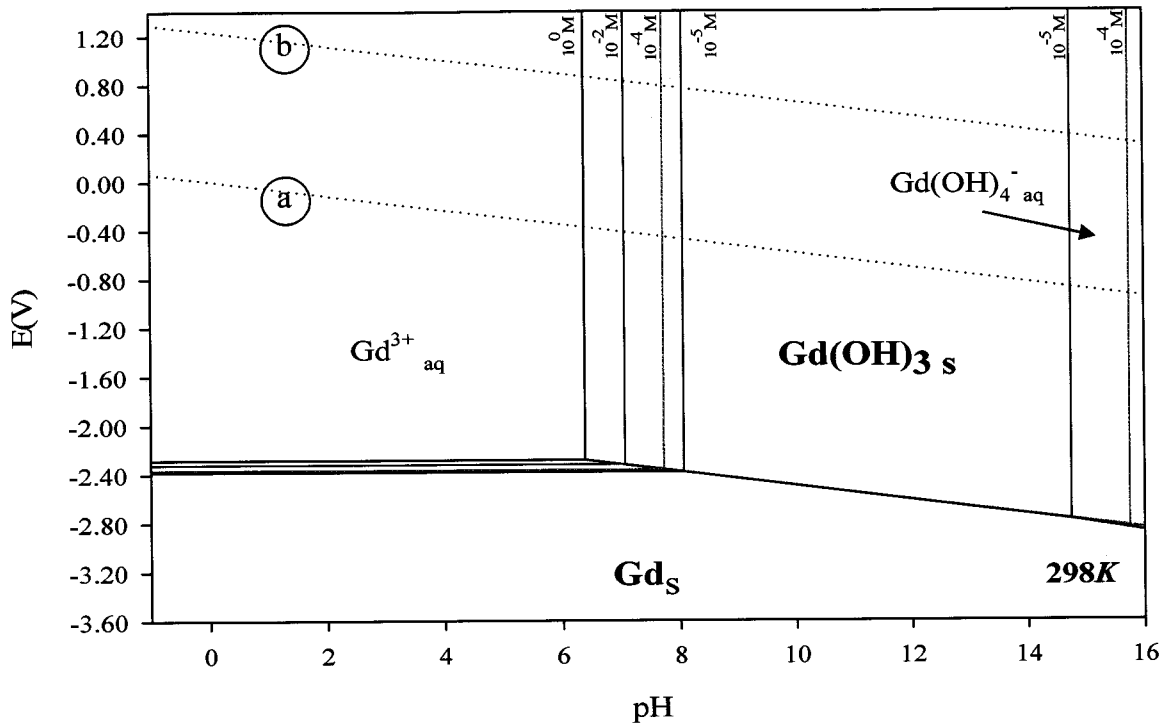


Figure 35. The Pourbaix diagram for gadolinium at 298 K, for aqueous concentrations of 1,  $10^{-2}$ ,  $10^{-4}$ , and  $10^{-5}$  molal.

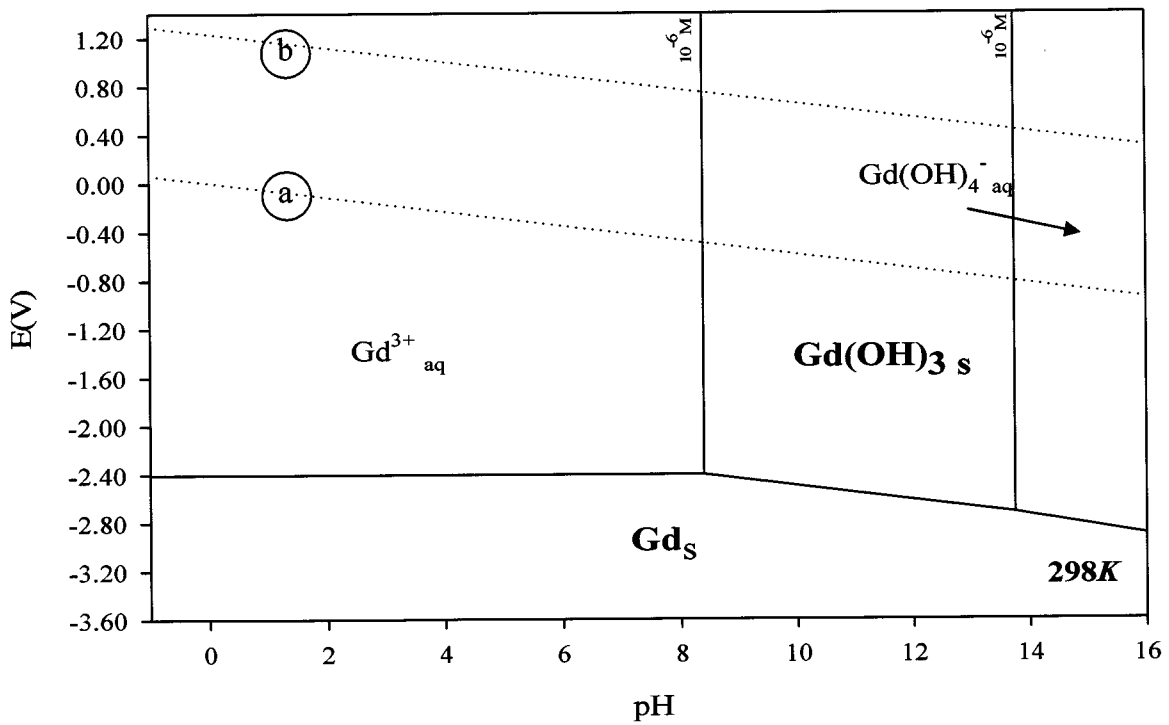


Figure 36. The Pourbaix diagram for gadolinium at 298 K, for an aqueous concentration of  $10^{-6}$  molal.

## CHAPTER 6 Discussion

The experimental work leading to estimates for the thermodynamic properties of dysprosium and gadolinium hydroxides, hydrates and complex ions in aqueous solutions are intended to be supportive of the continued development of burnable neutron absorber (BNA) materials for the Advanced CANDU<sup>®</sup> Reactor 1000 (ACR-1000) fuel bundle. Pure dysprosium and gadolinium oxides, as were studied in this work, are not actually employed in the BNA material. Instead, a material comprised of  $ZrO_{2,s}$  with proprietary concentrations of  $Gd_2O_{3,s}$  and  $Dy_2O_{3,s}$  and  $Y_2O_{3,s}$  \* are to be used. Accordingly it is appropriate to consider the solubility of pure  $ZrO_{2,s}$  which is actually the most concentrated component in the BNA.

### 6.1 Behaviour of Zirconia in Aqueous Solution

The Pourbaix diagrams for pure  $Zr$  are shown in Figure 37 and Figure 38 for temperatures of 298 K and 550 K respectively.

---

\* Because yttrium is not a strong absorber of neutrons it was not included in the current research. Moreover chemically, it is expected to behave similarly to Dy and Gd as are all the Rare Earth elements as discussed in Chapter 2.

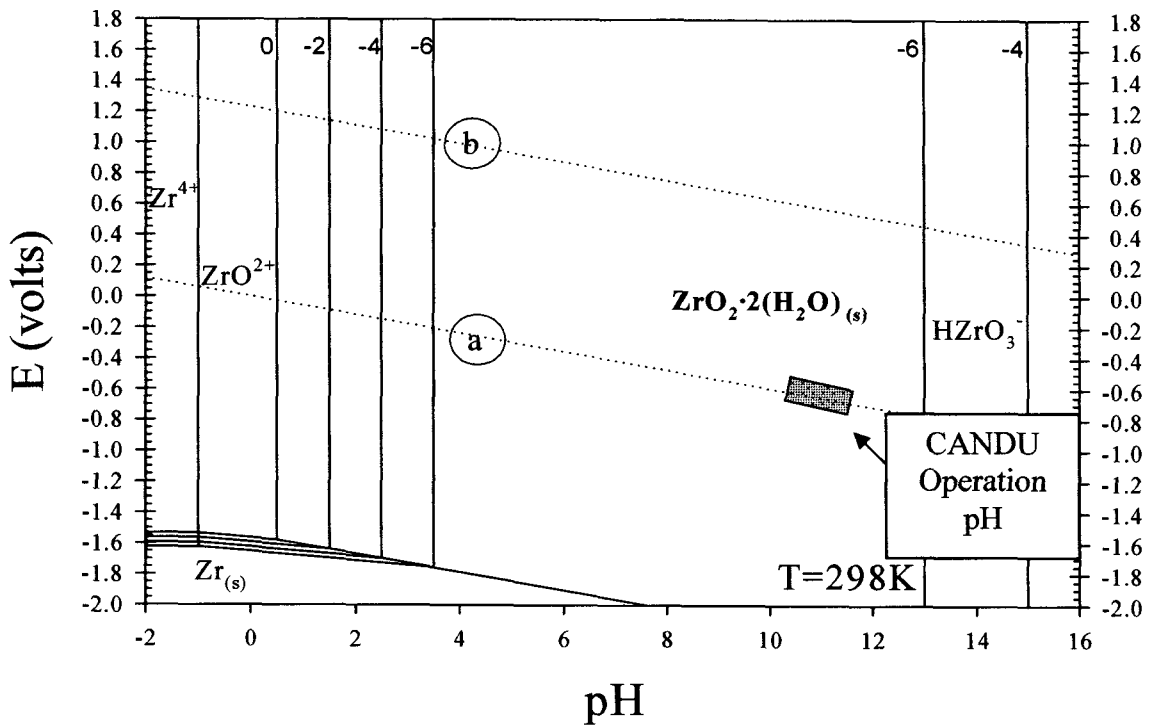


Figure 37. The Pourbaix diagram for Zr at 298 K, showing aqueous concentrations at  $1$ ,  $10^{-2}$ ,  $10^{-4}$ , and  $10^{-6}$  molal. The pressure is understood to be sufficient to suppress boiling [19].

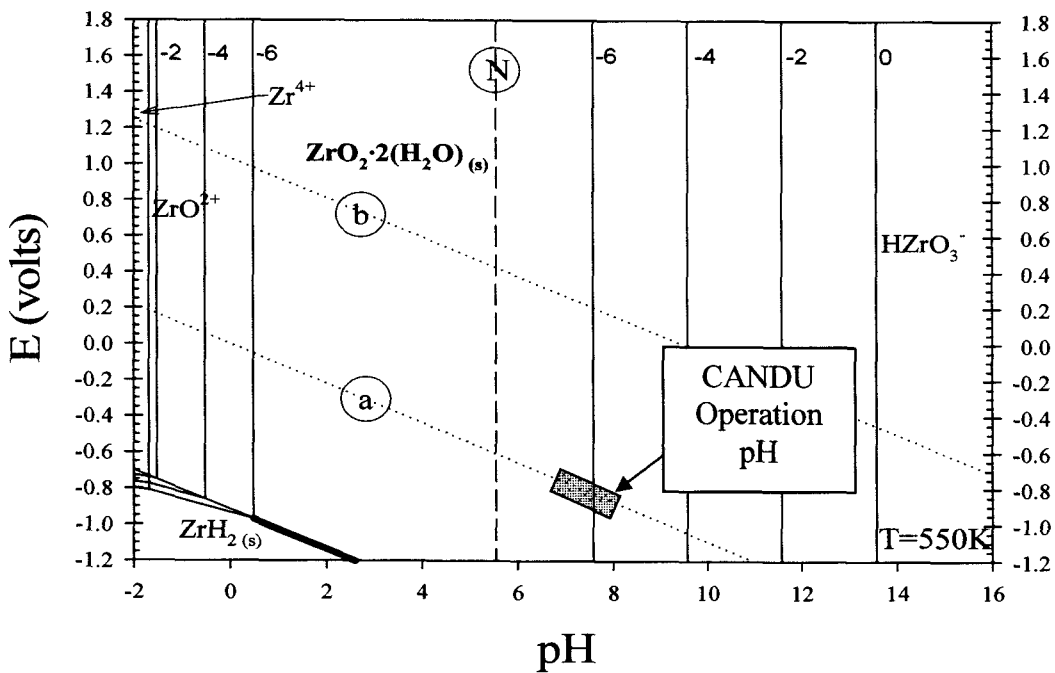


Figure 38. The Pourbaix diagram for Zr at 550 K, showing aqueous concentrations at  $1$ ,  $10^{-2}$ ,  $10^{-4}$ , and  $10^{-6}$  molal. The pressure is understood to be sufficient to suppress boiling [19].

The notable point in relation to the present work is the stability of the  $ZrO_2 \cdot 2H_2O_s$  in contact with water at coolant operating conditions. Consider the diagram at 298 K, at a pH of 13. The solubility of  $ZrO_2 \cdot 2H_2O_s$  anywhere between the extremes of oxygen saturation (line “b”) and hydrogen saturation (line “a”) depends on the  $HZrO_3^-_{aq}$  dominant ion in aqueous solution ( $10^{-6}$  molal). In principle, the  $ZrO_{2,s}$  is covered with a superficial layer of the dihydrate. This hydrate formation is similar to the case of pure  $Dy_2O_{3,s}$  and pure  $Gd_2O_{3,s}$  depicted previously in Figure 12 in Chapter 2. If the pH of an aqueous solution for pure zirconia were shifted to a lower value near 10, for example 10.3, the concentration of  $HZrO_3^-_{aq}$  shifts to a lower value that can be judged from the line placements on Figure 37 in the order of  $10^{-8}$  molal, or slightly lower. This is in accord with the findings of Sunder and Wren [23]. As the temperature is raised, the solubility of  $ZrO_{2,s}$ , that is  $ZrO_{2,s}(H_2O)_{2s}$ , changes in accordance with Figure 38 [19].

## 6.2 Temperature Effect on pH Scale

The vertical line labelled “N” is to be noted on Figure 38. This is the pH of neutrality of water at 550 K. The shift in the pH of neutrality is a consequence of the self dissociation constant of water increasing with temperature, as shown in Figure 39. Also shown in Figure 39 is the alteration in pH of lithium hydroxide solutions as the temperature is raised. These are represented by the two curves on the right of the diagram bracketing the range of alkalinity maintained in the coolant. This figure draws attention to the need to make clear the temperature at which the pH is measured particularly when the

temperature is substantially different than 298 K. A pH of 10 at room temperature creates a pH of a much lower value at coolant conditions that are nearer 300°C.

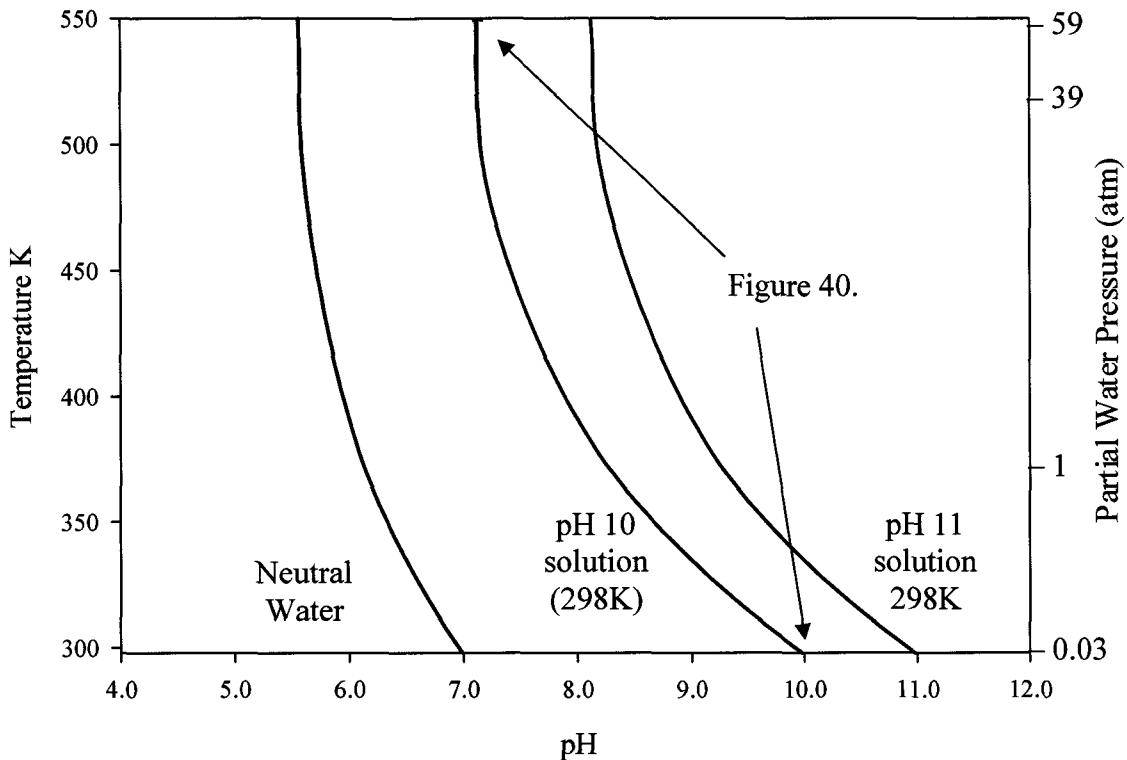


Figure 39. Temperature effect on aqueous solutions. Approximate water partial pressure (atm) shown on right.

In considering Figure 39, one must keep in mind that the pressure is also a variable, and it is necessary to maintain a high value for the stability of the liquid phase. Therefore, at 550 K a coolant pressure in excess of (~60 atm) [39] is sufficient to suppress boiling (coolant “voiding” with implications as discussed in Chapter 1).

Figure 40 below shows computations related to the construction of Figure 39. This makes the small point that the effects of temperature on the pH cannot be made strictly speaking without knowledge of the chemical speciation in the solution controlling the pH. In



particular, the presence of neutral *LiOH* species involved in reactor coolant competes with the equilibrium of hydroxide ions associating with hydrogen ions to form water molecules. Therefore, it is not possible in principle to make the correction for the effect of temperature on a pH measurement without knowledge of the entire water chemistry. That is, knowledge of the base controlling the pH, along with the possible presence of such species of dysprosium and gadolinium are proposed in the present interpretation of BNA solubility.

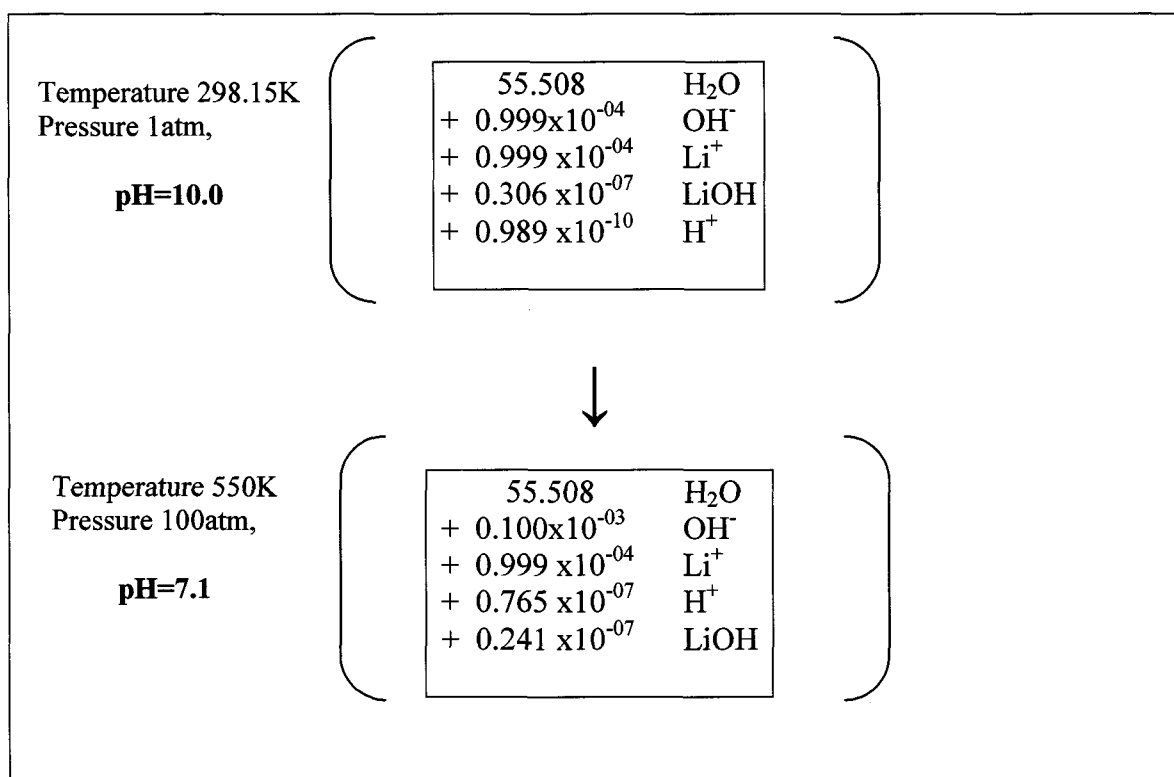


Figure 40. Sample calculation depicting the effect of temperature on alkaline lithium hydroxide solution typical of reactor coolant. Points are indicated on Figure 39.

### 6.3 Pourbaix Diagrams Projected to High Temperature

Returning to the construction of the Pourbaix diagrams for dysprosium and gadolinium, projections to high temperatures can be made with the knowledge of how changes in temperature affect Gibbs energies. This requirement was the main reason for estimating the entropy ( $S=dG/dT$ ) of the proposed complex ions. Shown below in Figure 41 to Figure 44 are the sets of Pourbaix diagrams for dysprosium and gadolinium respectively, projected to 550 K, with the inclusions of the proposed complex ions.

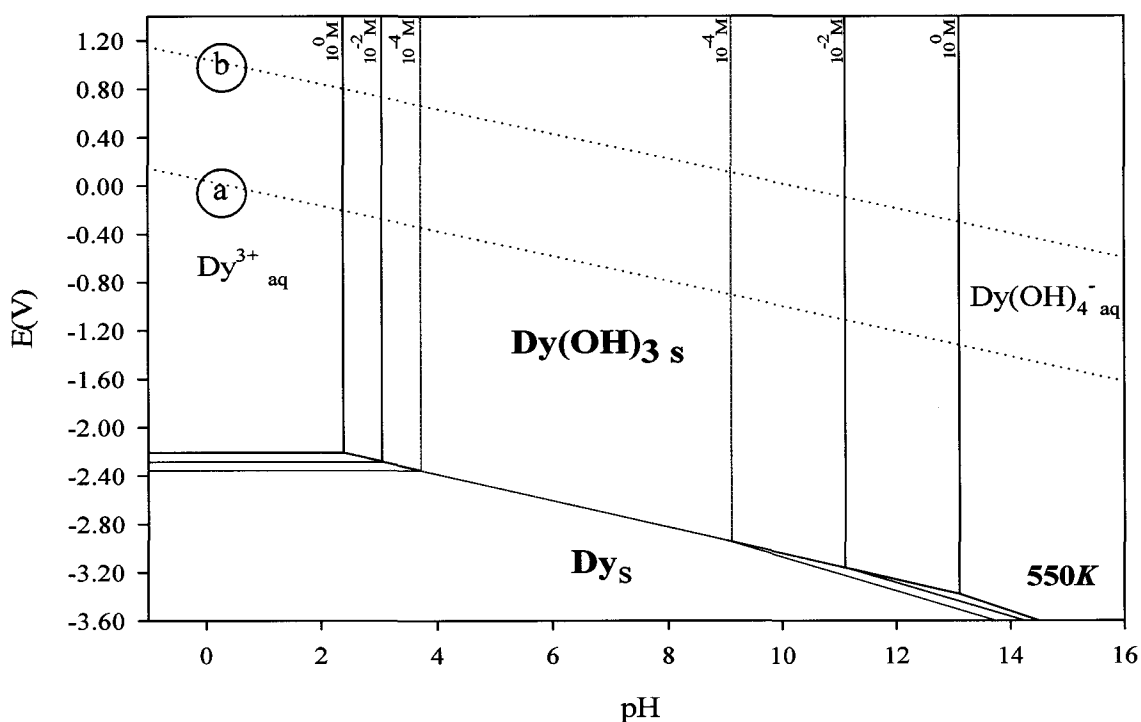


Figure 41. The Pourbaix diagram for dysprosium at 550 K, for aqueous concentrations of 1,  $10^{-2}$ , and  $10^{-4}$  molal.

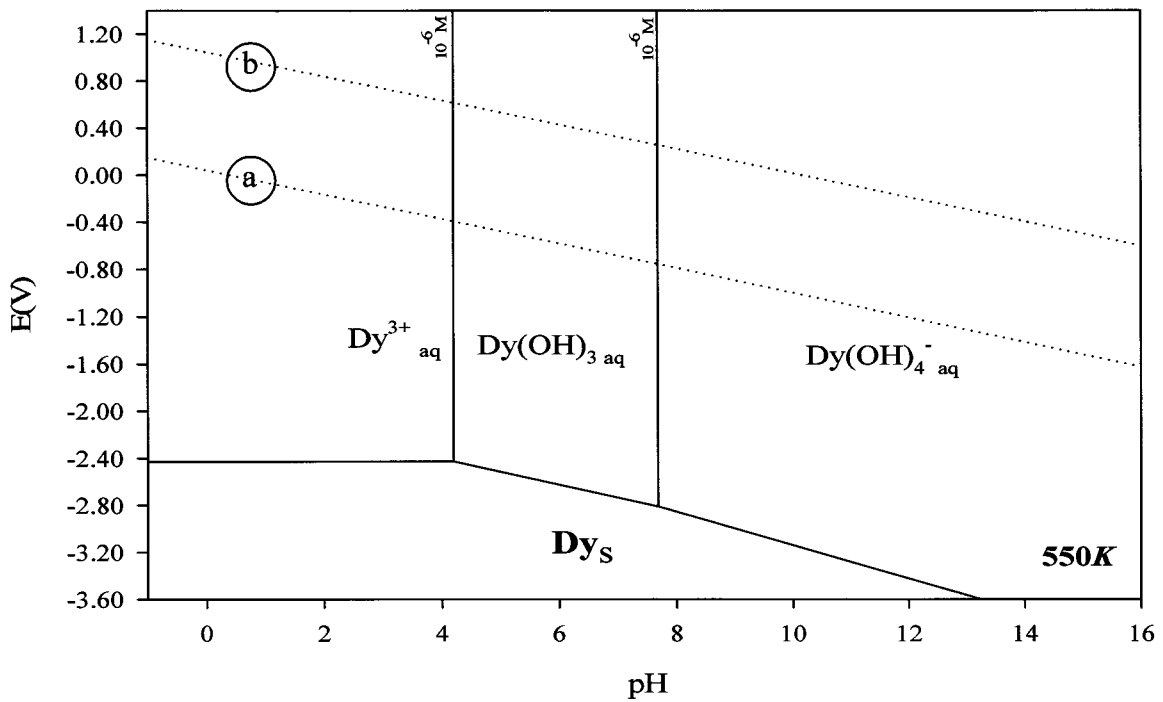


Figure 42. The Pourbaix diagram for dysprosium at 550 K, for an aqueous concentration of  $10^{-6}$  molal.

It can be seen from the above two figures that, as the concentration of dysprosium ions in solution becomes progressively lower, the stable domain of dysprosium hydroxide becomes progressively narrower because of the growing dominance of the indicated complex ions. When the concentration becomes sufficiently low (approximately  $10^{-5}$  to  $10^{-6}$  m), shown in Figure 42, the stability of the neutral complex ion predominates over that of the solid hydroxide. Gadolinium acts much in the same way, with minor unique features shown below in Figure 43 and Figure 44.

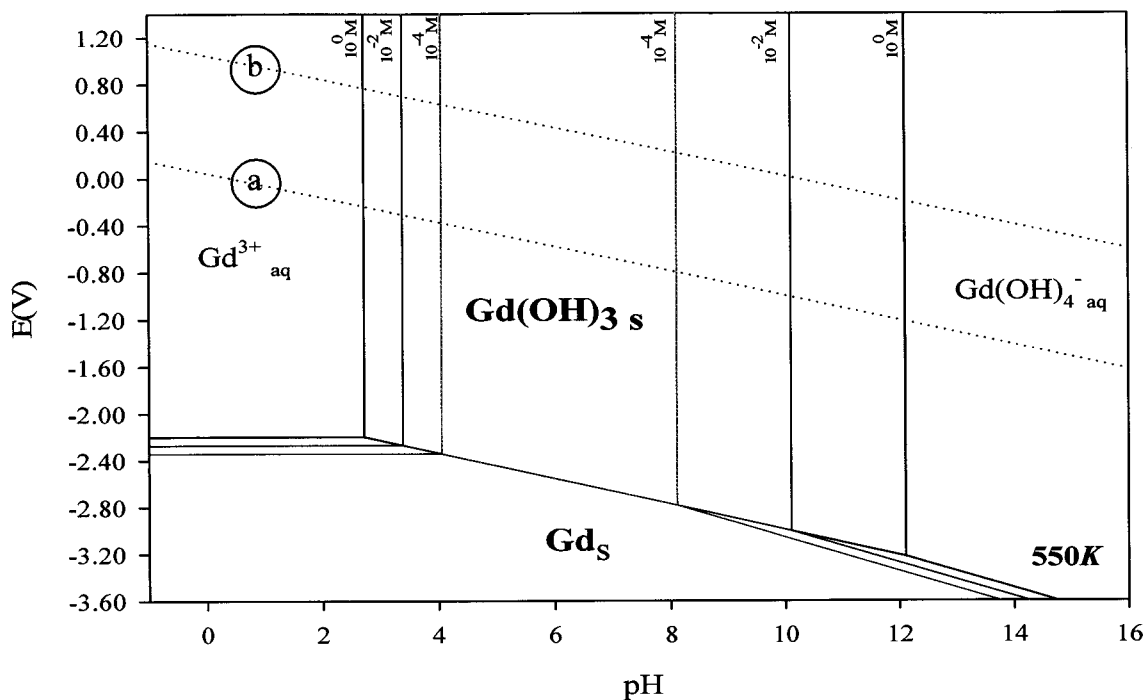


Figure 43. The Pourbaix diagram for gadolinium at 550 K, for aqueous concentrations of 1,  $10^{-2}$ , and  $10^{-4}$ , molal.

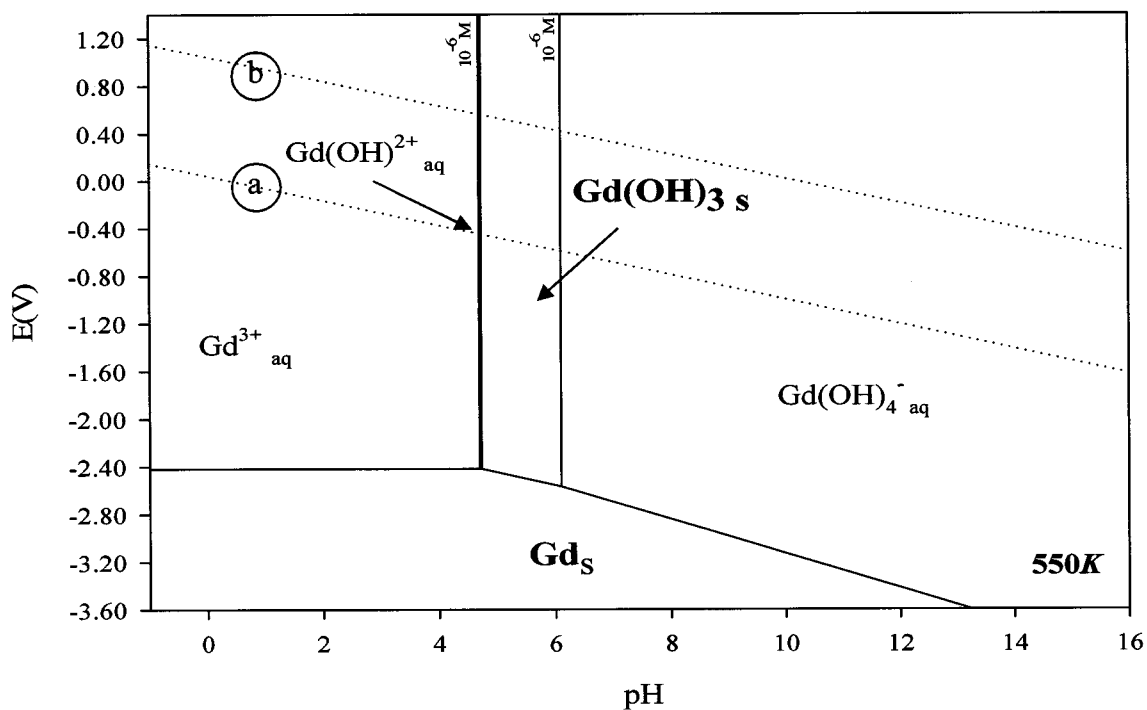


Figure 44. The Pourbaix diagram for gadolinium at 550 K, for an aqueous concentration of  $10^{-6}$  molal.

Like dysprosium, lower gadolinium concentrations expose a larger stable field for the complex gadolinium ions. A difference however, is the fact that unlike dysprosium at concentrations of  $10^{-6}$  m the solid gadolinium hydroxide still remains. A narrow field for  $Gd(OH)_{aq}^{2+}$  appears at the left hand boundary of the field for  $Gd(OH)_{3,s}$ .

#### 6.4 Coexistence of Dysprosium and Gadolinium

In the actual BNA material, the oxides are sintered into a solid solution with  $ZrO_{2,s}$ . The phase diagrams of the  $ZrO_{2,s}-Gd_2O_{3,s}$  and  $ZrO_{2,s}-Dy_2O_{3,s}$  appear below in Figure 45 and Figure 46 respectively. These diagrams have been previously modeled by Gibbs energy minimization methods, as introduced in Chapter 2, to be consistent with experimental studies of the phase equilibrium [12]. The BNA material is a metastable cubic solid solution with the fluorite crystal structure. This phase, in principle, is not thermodynamically stable at temperatures for intended in core reactor use ( $\sim 300^\circ\text{C}$ ), as the phase diagrams below indicate. However, experiments have shown that the cubic solid solution phase is very long lived in relation to the intended fuel bundle service.

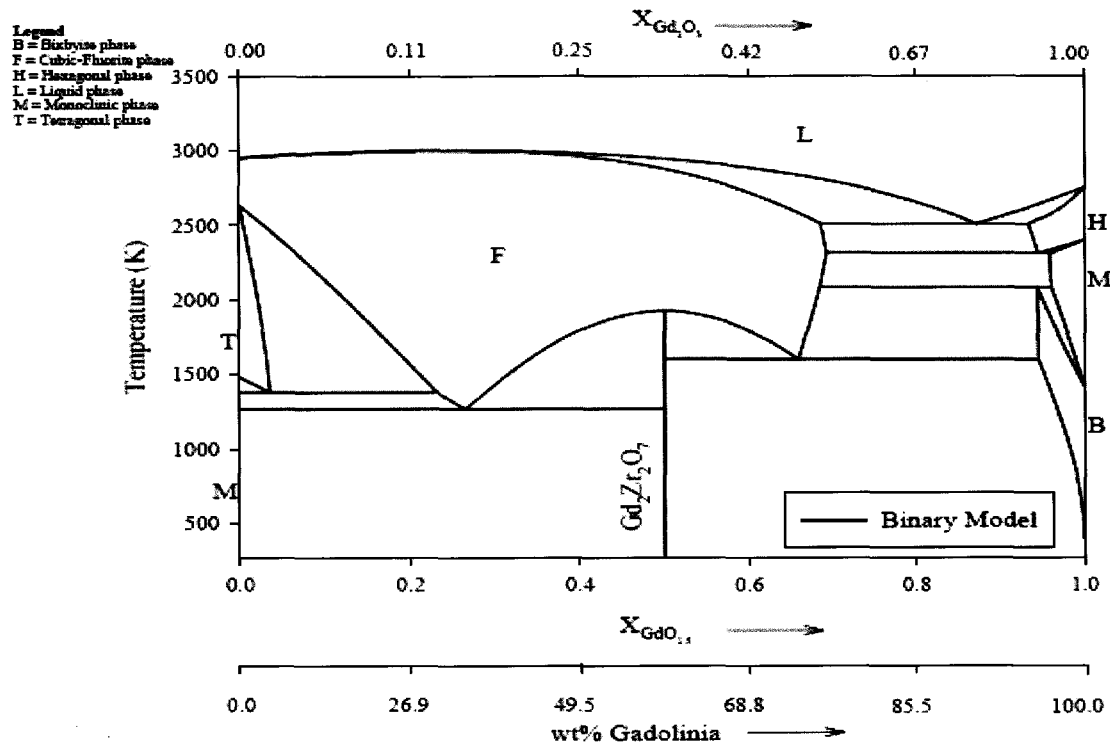


Figure 45. Binary phase diagram of zirconia-gadolinia [12].

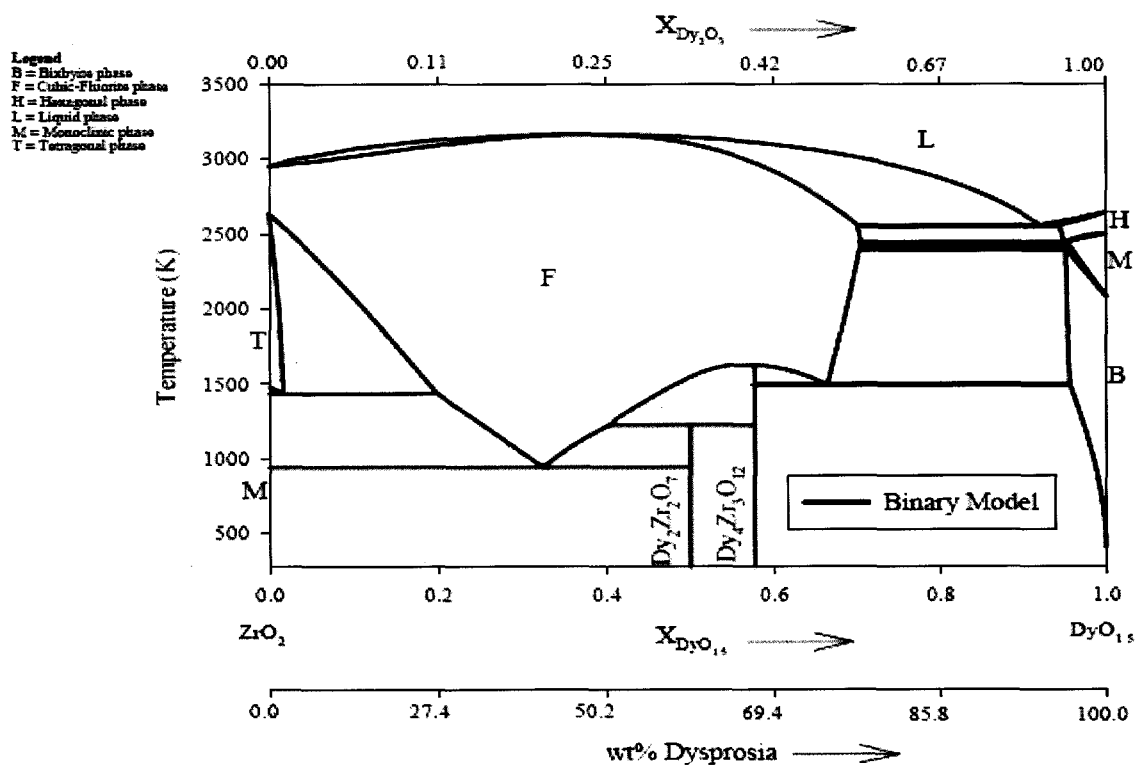
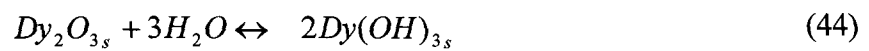


Figure 46. Binary phase diagram of zirconia-dysprosia [12].

With the foregoing in mind, the thermodynamic activities (effective concentration) of  $Dy_2O_{3,s}$  and  $Gd_2O_{3,s}$  are lower than one. This will have implications on chemical equilibria that qualitatively lower the concentration of soluble species in the coolant and may also preclude the formation of hydrates of dysprosium and gadolinium hydroxide. This point is perhaps made clearer by considering the equilibrium below



The concern here is that the activity of  $Dy_2O_{3,s}$  (dissolved in zirconia) may not be high enough in the presence of liquid water (coolant) to form  $Dy(OH)_{3,s}$ . If  $Dy(OH)_{3,s}$  does not form, then the solubility cannot be described using the Pourbaix diagrams, or the equilibrium concepts involved in interpreting experimental solubility measurements, which assumed coexistence with  $Dy(OH)_{3,s}$ .

It is evident that there are many considerations in computing the solubility in a multi-component system involving many possible species and phases, not to mention the concerns involved in achieving equilibrium. Herein lies the necessity of a powerful computational technique such as Gibbs energy minimization, to which the solubility framework in the present thesis is addressed.

Let us consider, for example, water containing a small number of moles of BNA with an arbitrary composition (mol fractions of  $Dy_2O_{3,s}$  and  $Gd_2O_{3,s}$  are both 0.1). The water phase is understood to be made alkaline with a low concentration of lithium hydroxide.

This is further made reducing by the small addition of dissolved hydrogen gas (representative of reactor coolant). This is to be understood as a simplified system for the discussion of BNA solubility.

To visualize the computation proposed, refer to Figure 47 for 550 K. The coolant, made alkaline with lithium hydroxide, is shown in light blue. Represented below the coolant is a section of hypothetical BNA pellet surface (light gray) that would come into contact with the coolant if there were a sheath breach in the central element of the ACR-1000 fuel bundle. The final equilibrium condition is shown below the downward pointing bold arrow; this is the computed equilibrium using Gibbs energy minimization. The same equilibrium may be computed at 298 K and is shown in Figure 48.



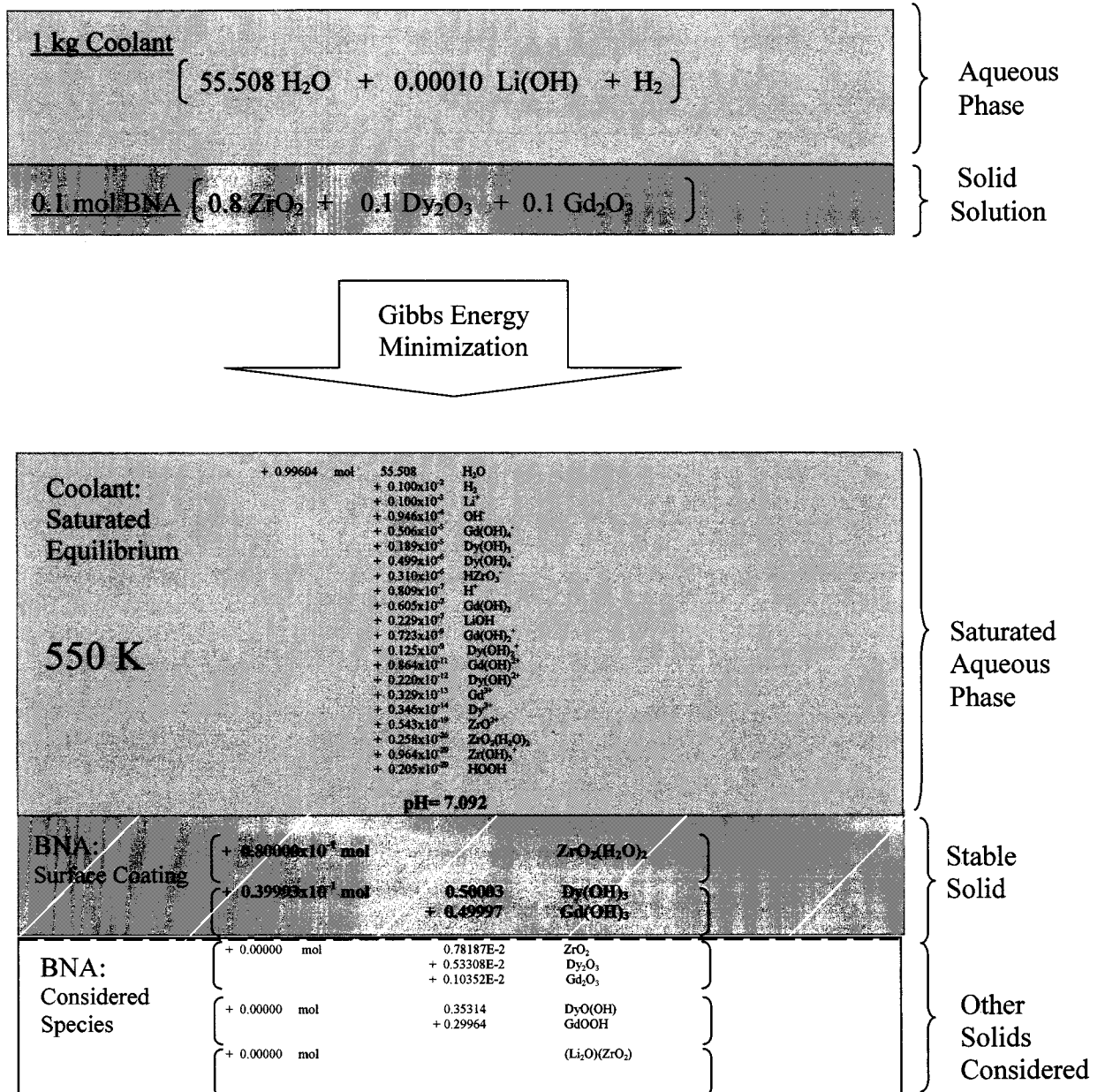
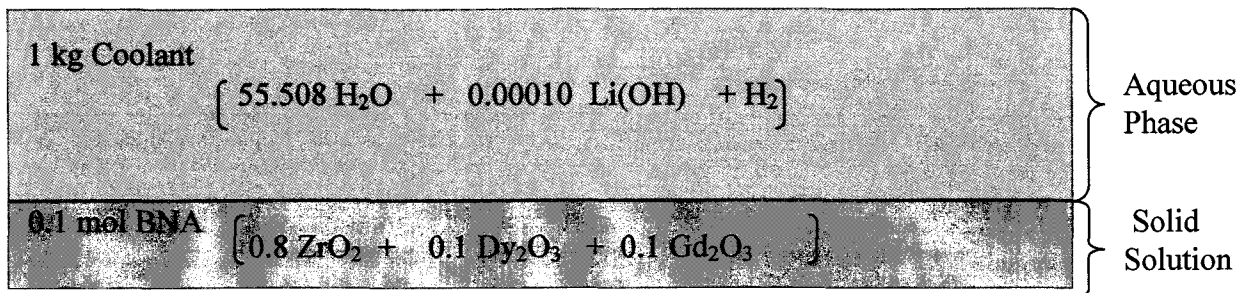


Figure 47. Solubility computation of an arbitrarily chosen BNA composition at 550 K .



Gibbs Energy Minimization

Coolant: Saturated Equilibrium 298K	+ 0.99604 mol	55.508	H <sub>2</sub> O	} Saturated Aqueous Phase
		+ 0.100x10 <sup>-02</sup>	H <sub>2</sub>	
		+ 0.100x10 <sup>-03</sup>	Li <sup>+</sup>	
		+ 0.100x10 <sup>-04</sup>	OH <sup>-</sup>	
		+ 0.115x10 <sup>-05</sup>	Dy(OH) <sub>3</sub>	
		+ 0.309x10 <sup>-07</sup>	LiOH	
		+ 0.893x10 <sup>-09</sup>	HZrO <sub>3</sub>	
		+ 0.106x10 <sup>-09</sup>	H <sup>+</sup>	
		+ 0.915x10 <sup>-10</sup>	Gd(OH) <sub>3</sub>	
		+ 0.531x10 <sup>-10</sup>	Dy(OH) <sub>2</sub>	
		+ 0.495x10 <sup>-10</sup>	Gd(OH) <sub>2</sub>	
		+ 0.435x10 <sup>-10</sup>	Dy(OH) <sub>2</sub> <sup>+</sup>	
		+ 0.268x10 <sup>-10</sup>	Gd(OH) <sub>2</sub> <sup>+</sup>	
		+ 0.145x10 <sup>-10</sup>	Gd(OH) <sub>2</sub> <sup>2+</sup>	
		+ 0.710x10 <sup>-11</sup>	Gd <sup>3+</sup>	
		+ 0.696x10 <sup>-12</sup>	Dy(OH) <sub>2</sub> <sup>2+</sup>	
		+ 0.336x10 <sup>-12</sup>	Dy <sup>3+</sup>	
		+ 0.885x10 <sup>-13</sup>	ZrO <sub>2</sub> <sup>+</sup>	
		+ 0.175x10 <sup>-21</sup>	ZrO <sub>2</sub> (H <sub>2</sub> O) <sub>2</sub>	
		+ 0.203x10 <sup>-24</sup>	Zr(OH) <sub>3</sub> <sup>+</sup>	
	pH= 9.975			
BNA: Surface Coating	+ 0.90000x10 <sup>-1</sup> mol		ZrO <sub>2</sub> (H <sub>2</sub> O) <sub>2</sub>	} Stable Solid
	+ 0.39999x10 <sup>-1</sup> mol	0.50001 + 0.49999	Dy(OH) <sub>3</sub> Gd(OH) <sub>3</sub>	
BNA: Considered Species	+ 0.00000 mol	0.26141x10 <sup>-5</sup> + 0.12809x10 <sup>-5</sup> + 0.79307x10 <sup>-8</sup>	ZrO <sub>2</sub> Dy <sub>2</sub> O <sub>3</sub> Gd <sub>2</sub> O <sub>3</sub>	} Other Solids Considered
	+ 0.00000 mol	0.76839x10 <sup>-4</sup> + 0.17302x10 <sup>-4</sup>	DyO(OH) GdOOH	
	+ 0.00000 mol		(Li <sub>2</sub> O)(ZrO <sub>2</sub> )	

Figure 48. Solubility computation of an arbitrarily chosen BNA concentration at 298 K.

In both Figure 47 and Figure 48 it can be seen that there is a far larger amount of water compared to the BNA material. This is representative of a small breach in a Zircaloy

sheath. This occurrence is expected to expose a small surface quantity of BNA material to a considerably large quantity of coolant.

Once equilibrium is reached, represented by the state after Gibbs energy minimization, the coolant is shown to become saturated with the proposed aqueous species of dissolved BNA material. Comparing the aqueous equilibrium output for both 550 K and 298 K indicates that slightly more BNA dissolves at high temperature; however, both conditions indicate that the extent is minute. Equilibrium computations have also indicated that aqueous species of dysprosium and gadolinium become more soluble and therefore more dominant in the aqueous phase than species of zirconium. The extent to which these species of dysprosium and gadolinium leach into the saturated coolant is limited. As previously mentioned, once these oxides are in contact with water, they form a surface coating of each respective hydroxide or in the case of zirconia, a dihydrate (above the dashed line representing the surface coating). It is these two solid phases ( $ZrO_{2,s}(H_2O)_{2s}$ , and  $\{(Dy,Gd)(OH)_{3,s}\}$ ) which are considered to be controlling the solubility. In this treatment, the chemically similar  $Dy(OH)_{3,s}$  and  $Gd(OH)_{3,s}$  are considered to form an ideal solid solution (denoted by  $\{\}$ ), making the activity of each component hydroxide equal to the mole fraction.

A limitation on the dissolution of Dy and Gd may be attributed to the fact that the coolant is saturated with zirconium. Once the hydroxides of dysprosium and gadolinium on the thin surface coating leach, it would become progressively more difficult for Dy and Gd some distance under the pellet surface to dissolve, since solid state diffusion is required.

It is thought that further significant dissolution would be hindered by the general saturation of coolant with zirconium dihydrate ( $ZrO_2 \cdot (H_2O)_{2s}$  covering all Zircaloy through which the coolant must pass). In performing the Gibbs energy minimization computations, other solid species and solid solutions were considered. These are shown below the dashed line. However, the inclusion of these possible phases in the equilibrium assemblage does not contribute to lowering the Gibbs energy of the system and these compounds show zero mols formed.

Figure 47 and Figure 48 are suggestive of how the current solubility treatment could be useful in not only modelling effects of temperature and pressure, but also on how to plan high temperature experimentation in order to yield data to improve the current model. In particular, these figures draw attention to the difficulty of sampling hot saturated solutions that may precipitate before chemical analysis can be performed.

## CHAPTER 7 Summary and Conclusion

The thesis is intended to contribute insight into aqueous solubility of neutron absorbing materials proposed for use in the BNA central element of the Advanced CANDU<sup>®</sup> reactor fuel bundle. In particular, a framework to model solubility with thermodynamic parameters for the various aqueous species and phases is proposed.

1. Solubility measurements were conducted on dysprosium oxide ( $Dy_2O_{3,s}$ ) and gadolinium oxide ( $Gd_2O_{3,s}$ ) at room temperature and pressure conditions, yielding the solubility products of each trihydroxide.
2. The most important variable under consideration was the pH. This was measured using a platinum - hydrogen electrode and a saturated calomel reference electrode.
3. Thermogravimetric analysis provided the decomposition behaviour of the hydroxides as well as the monohydrates. The measurements were used to infer thermodynamic properties establishing proposed phase boundaries on a diagram of  $\log(P)$  versus  $1/T$ .
4. It was concluded that the solubility of  $Dy_2O_{3,s}$  and  $Gd_2O_{3,s}$  (collectively  $Ln_2O_{3,s}$ ) is controlled by a superficial formation of trihydroxide ( $Ln(OH)_{3,s}$ ) or equivalently trihydrate ( $Ln_2O_3 \cdot 3H_2O_s$ ).

5. Solubility measurements and related thermodynamic information were interpreted and expressed on the supposition that complex ions of the type  $Ln(OH)_n^{3-n}$  exist ( $n=1$  to 4).
6. Estimates of the entropy of proposed complex ions and other aqueous species were established in order that Gibbs energy minimization calculations could be made at elevated temperatures associated with conditions in a reactor.
7. Pourbaix diagrams were calculated for Dy and Gd at 298 K and 550 K using the proposed thermodynamic properties and other accepted data to establish domains of stability in redox potential - pH space.
8. Calculations, using Gibbs energy minimization, illustrated how solubility measurements based on the proposed treatment might be useful in matters of commercial ACR-1000 design, as well as the planning of additional solubility experiments.
9. It is generally concluded that the low solubility of dysprosium and gadolinium in coolant with pH near 10 (measured at 298 K) does not pose a safety concern with respect to the issue of neutron economy in ACR-1000 operation caused by a defected central element.

## CHAPTER 8 Recommendations

It is recommended for the further development of aqueous solubility modelling that the following be undertaken:

1. Perform additional measurements of solubility under conditions of high alkalinity. These should include gadolinium oxide as well as yttrium oxide (the cubic phase stabilizer).
2. Perform direct measurements of solubility at operating conditions, not withstanding the complications of sampling saturated solutions at high temperature and pressure as well as the disturbing effects caused by the likely precipitation during cooling.
3. Perform thermogravimetric work, controlling the partial pressure of water vapour, to provide improved decomposition temperatures for the hydrates.

## REFERENCES

1. G. Timilsina, T. Walden, A. Shahmoradi, A. Naini, D. McColl, P. Prince, and J. Rozhon, "The Canadian Nuclear Industry: Contributions to the Canadian Economy", Canadian Nuclear Association, Ottawa, Canada (2008).
2. CANDU Canada, "Other Questions", website:  
<http://www.canducanada.ca/eng/questions.html> (2007).
3. World Nuclear Association, "Nuclear Power in Canada", website:  
[http://www.world-nuclear.org/info/inf49a\\_Nuclear\\_Power\\_in\\_Canada.html](http://www.world-nuclear.org/info/inf49a_Nuclear_Power_in_Canada.html) (2010).
4. CANDU Canada, "Energy Gap", website:  
<http://www.canducanada.ca/eng/energy.html> (2007).
5. J. Lamarsh and A. Baratta, "Introduction to Nuclear Engineering". 3<sup>rd</sup> Ed., Prentice Hall, New Jersey, United States (2001).
6. Nuclear Threat Initiative, "Nuclear Terrorism: Fission", website image:  
[http://www.nti.org/h\\_learnmore/nuctutorial/chapter02\\_02.html](http://www.nti.org/h_learnmore/nuctutorial/chapter02_02.html) (2009).
7. Korea Atomic Energy Research Institute, "Table of Nuclides", website:  
<http://atom.kaeri.re.kr/> (2000).
8. B. Cox, "Zirconium Alloy Corrosion", Uhlig's Corrosion Handbook 2<sup>nd</sup> Ed., Ed. R. Winston Revie, John Wiley and Sons Incorporated, New York, United States (2000) 904-914.
9. Atomic Energy of Canada Limited, "ACR-1000 Technical Summary: An Evolution of CANDU<sup>®</sup>", Atomic Energy of Canada Limited (2007).
10. W. Garland, "How and Why is CANDU Designed the Way It Is", McMaster University, Ontario, Canada (2003).
11. Alfa Aesar, "Research Chemicals, Metals and Materials", A Johnson Matthey Company, Massachusetts, United States (2008).
12. E. Corcoran, "Thermodynamical Modeling of Advanced CANDU Reactor Fuel", Doctoral Thesis, Royal Military College, Kingston, Ontario, Canada (2009).
13. D. Torgerson, "The ACR-700 – Raising The Bar for Reactor Safety Performance, Economics and Constructability", Nuclear News 45 (2002) 24-32.



14. P. Boczar, "Advanced Fuel Development in AECL", Canadian Nuclear Society Bulletin 24 (2005) 17-24.
15. G. Erdtmann, "Neutron Activation Tables", 6<sup>th</sup> Ed., Kerchemie in Einzeldarstellungen, Verlag Chemie, New York, United States (1976).
16. I. Diakonov, K. Ragnarsdottir, and B. Tagirov, "Standard Thermodynamic Properties and Heat Capacity Equations of Rare Earth Hydroxides", Chemical Geology 151 21 (1998) 327-347.
17. J. Haas, E. Shock, and D. Sassani, "Rare Earth Elements in Hydrothermal Systems: Estimates of Standard Partial Molal Thermodynamic Properties of Aqueous Complexes or the Rare Earth Elements at High Pressure and Temperatures", *Geochemica et Cosmochimica Acta* 59 21 (1995) 4329-4350.
18. M. Pourbaix, "Atlas of Electrochemical Equilibria in Aqueous Solutions", Pergamon Press Ltd. Bristol, England (1966).
19. M. Kaye, and W. Thompson, "Computation of Pourbaix Diagrams at Elevated Temperatures", Royal Military College, Kingston, Ontario, Canada, (2009).
20. S. Sunder, and N. Tosello, "Leaching Behaviour of Dysprosium-Doped (U,Dy)O<sub>2</sub> LVRF Fuel Under CANDU Coolant Conditions", Proceedings of 9<sup>th</sup> International Conference on CANDU Fuel, Belleville, Ontario, Canada (2005).
21. S. Sunder, K. Horn, J. Fingas, and T. Petersen, "Solubility of Selected Lanthanide Oxides used as Neutron Poisons: Dysprosium Oxide, Holmium Oxide, and Gadolinium Oxide", Proceedings of 26<sup>th</sup> Annual Conference of the Canadian Nuclear Society, Toronto, Canada (2005).
22. S. Hebert, "Identification and Leaching of Defective Low Void Reactivity Fuel", Masters Thesis, Royal Military College, Kingston, Ontario, Canada (2009).
23. S. Sunder, and S. Wren, "Aqueous Solubility of Zirconia", Proceeding of 29<sup>th</sup> Annual Conference of the Canadian Nuclear Society, Toronto, Ontario, Canada (2008).
24. M. Piro, M. Welland, B. Lewis, and W. Thompson, "Development of a Self Standing Numerical Tool to Compute Chemical Equilibria in Nuclear Materials", Proceedings of Top Fuel Conference, Paris, France (2009).
25. G. Adachi, N. Imanka, and Z. Kang, (Eds.) "Binary Rare Earth Oxides", Kluwer Academic Publishers, Dordrecht, Netherlands (2004).

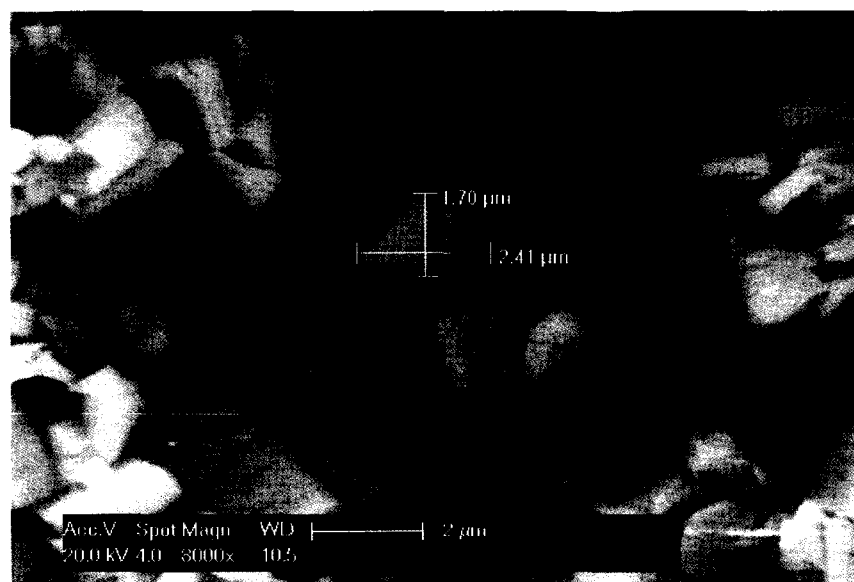
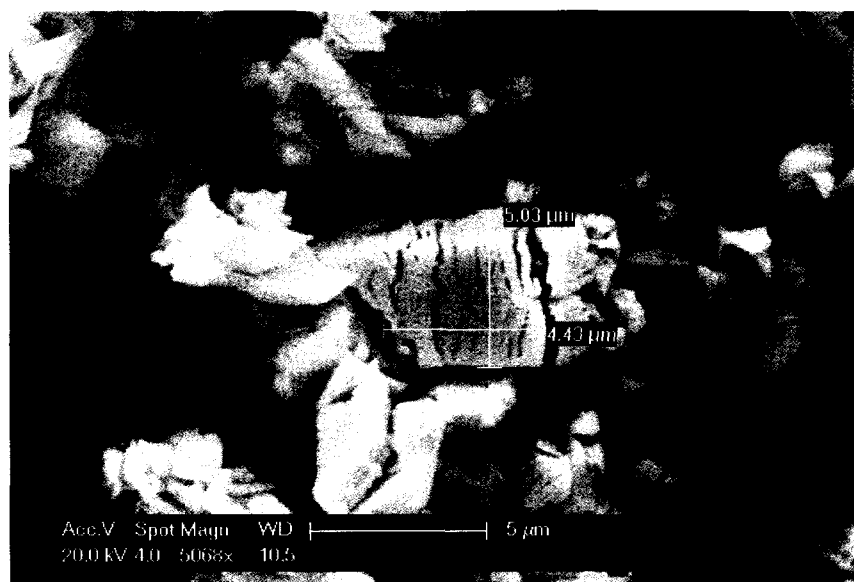
26. W. Kingery, H. Bowen, and D. Uhlmann, "Introduction to Ceramics", 2<sup>nd</sup> Ed., Wiley and Sons, New York, United States (1976).
27. Private communication, between W.T. Thompson, E.C. Corcoran and P. Tremaine June 2008.
28. C. Bale, A. Pelton, and W. Thompson, "Facility for the Analysis of Chemical Thermodynamics", Ecole Polytechnique, Montréal, Canada (2002).
29. W. Thompson, M. Kaye, C. Bale, and A. Pelton, "Pourbaix Diagrams for Multielement Systems", Uhlig's Corrosion Handbook 2<sup>nd</sup> Ed., Ed. R. Winston Reveie, John Wiley and Sons Incorporated, New York, United States (2000) 125-136.
30. L. Meites, "Handbook of Analytical Chemistry", McGraw - Hill, New York, United States (1963).
31. University of Missouri Research Reactor, "Neutron Activation Analysis", website: <http://archaeometry.missouri.edu/services.html> (2009).
32. Private communication, K. Mattson to A. Blackier, Royal Military College, Kingston, Ontario, Canada 2010.
33. D. Wagman, "Selected Values of Chemical Thermodynamic Properties", National Bureau of Standards Series 270, U.S. Department of Commerce, Washington, United States (1968-1971).
34. S. Prophet, "JANAF Thermochemical Tables", U.S. Department of Commerce, Washington, United States (1985).
35. J. Sangster, and A.D. Pelton, "Phase Diagrams and Thermodynamic Properties of the 70 Binary Alkali Halide Systems Having Common Ions", Journal of Physical and Chemical. Ref. Data 16 (1987) 509-561.
36. I. Barin, O. Knacke, and O. Kubaschewski, "Thermochemical Properties of Inorganic Substances", Springer-Verlag, Berlin, Germany (1977).
37. H. Barner, and R. Scheuerman, "Handbook of Thermochemical Data for Compounds and Aqueous Species", Wiley - Interscience, New York, United States (1978).
38. E. Vernik Jr., "Simplified Procedure for Constructing Pourbaix Diagrams", Uhlig's Corrosion Handbook 2<sup>nd</sup> Ed., Ed. R. Winston Reveie, John Wiley and Sons Incorporated, New York, United States (2000) 111-125.

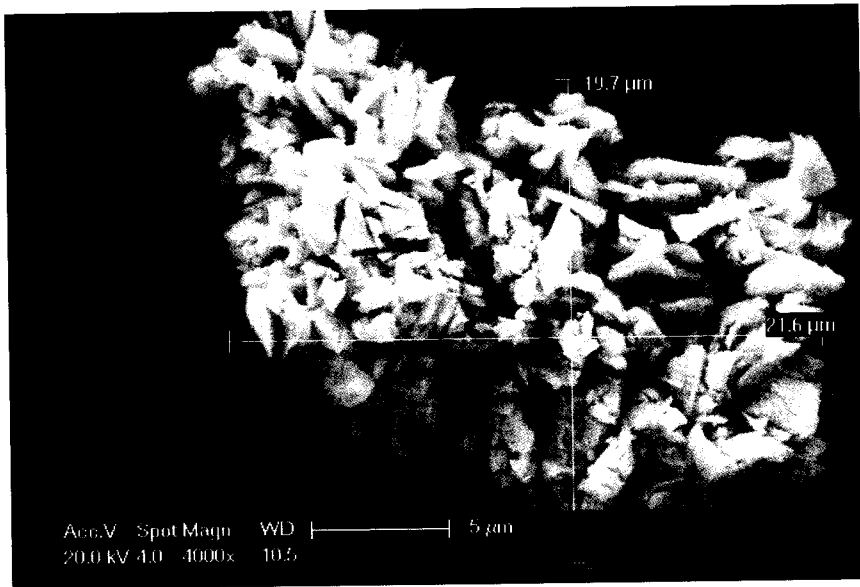
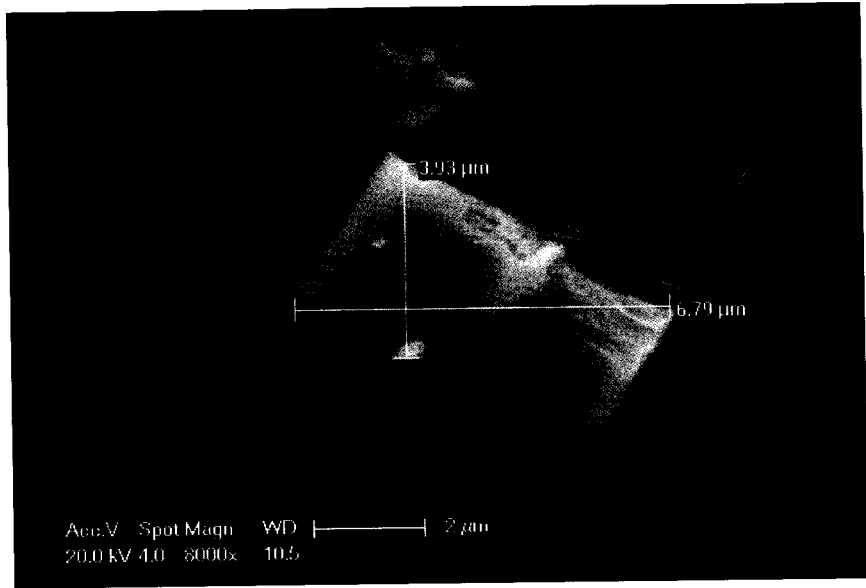
39. D. Olander, "General Thermodynamics", CRC press, Florida, United States (2008).

## APPENDICIES

## APPENDIX A. Dysprosium Oxide ( $\text{Dy}_2\text{O}_3$ ) Particle Size

A scanning Electron Microscope (SEM) was used to investigate the fine particle size of the Lanthanide oxides, specifically in this case dysprosium oxide, used in the water solubility experimentation.





## APPENDIX B. Neutron Activation Analysis Reports

### RMC ANALYTICAL SCIENCES GROUP - GROUPE DES SCIENCES ANALYTIQUES DU CMR

Royal Military College, PO Box 17000 Stn. Forces, Kingston, ON, K7K 7B4  
(613) 541-6000 ext 6684 / Fax (613) 545-8341

Client: Dr. Thompson & Dr. Corcoran  
The Royal Military College of Canada  
Dept. of Chemistry & Chemical Engineering  
Kingston, Ontario K7K 7B4  
Tel: (613) 541-6000 ext. 6510

ASG Login No: 20355  
Site: RMC, Blackier  
Client No: N/A  
Samples Received: 01-Mar-10  
Date of analysis: 02-Mar-10  
Method No: NAA  
Date Reported: 02-Mar-10  
Sheet: 1 of 1  
E-mail: Sent on 02 Mar 2010 *tn*

#### RESULTS OF NEUTRON ACTIVATION ANALYSIS

Sample ID	Dysprosium (µg/g)
Dysprosia in LiOH solution	0.31 ± 0.01

pH= 14.2  
Dy (mol·kg<sup>-1</sup>)= 1.908x10<sup>-6</sup>

The results reported here relate only to the items / materials tested.

The only reported error is that from the counting statistics only. Counting error reported at one sigma.

#### LABORATORY QA/QC

Sample ID	Dysprosium (µg/g)
Dysprosia in LiOH solution Sub-sample 1	0.310 ± 0.009
Dysprosia in LiOH solution Sub-sample 2	0.302 ± 0.008
Blank (empty 1.5 cc vial)	< 0.003
Control, Experimental Result:	42.3 ± 0.4
Control Target	40.3

Prepared By: *K. Mattson*  
Kristine Mattson,  
Nuclear Technologist, SLOWPOKE-2 Facility.  
02 Mar 2010

Authorization: *K. Nielsen*  
Kathy Nielsen,  
Director, SLOWPOKE-2 Facility.  
02 Mar 2010  
Test Report I.D. NAABlackier20355R1.xls

**RMC ANALYTICAL SCIENCES GROUP - GROUPE DES SCIENCES ANALYTIQUES DU CMR**

Royal Military College, PO Box 17000 Stn. Forces, Kingston, ON, K7K 7B4  
(613) 541-6000 ext 6684 / Fax (613) 545-8341

**Client :** Dr. Thompson & Dr. Corcoran  
The Royal Military College of Canada  
Dept. of Chemistry & Chemical Engineering  
Kingston, Ontario K7K 7B4  
Tel: (613) 541-6000 ext. 6510

ASG Login No:	20369
Site:	RMC, Blackler
Client No:	N/A
Samples Received:	8-Mar-10
Date of analysis:	8-Mar-10
Method No:	NAA
Date Reported:	8-Mar-10
Sheet:	1 of 1
E-mail:	Sent on 09 Mar 2010

*77*

**RESULTS OF NEUTRON ACTIVATION ANALYSIS**

Sample ID	Dysprosium (µg/g)
A pH ~ 10*	2.11 ± 0.02
B pH ~ 12*	1.55 ± 0.02

Dy (mol·kg<sup>-1</sup>)= 1.298x10<sup>-5</sup>

Dy (mol·kg<sup>-1</sup>)= 9.538x10<sup>-6</sup>

\* Result of duplicate analysis.

The results reported here relate only to the items / materials tested.

The only reported error is that from the counting statistics only. Counting error reported at one sigma.

**LABORATORY QA/QC**

Sample ID	Dysprosium (µg/g)
A pH ~ 10 Sub-sample 1	2.15 ± 0.02
A pH ~ 10 Sub-sample 2	2.06 ± 0.02
B pH ~ 12 Sub-sample 1	1.49 ± 0.02
B pH ~ 12 Sub-sample 2	1.60 ± 0.02
Blank (empty 1.5 cc vial)	< 0.003
Control, Experimental Result:	16.8 ± 0.2
Control Target	16.2

Prepared By: K Mattson  
Kristine Mattson,  
Nuclear Technologist, SLOWPOKE-2 Facility,  
09 Mar 2010

Authorization: K Nielsen  
Kathy Nielsen,  
Director, SLOWPOKE-2 Facility,  
09 Mar 2010  
Test Report I.D: NAABlackier20369R1



## APPENDIX C. Solubility Product Calculation for Dysprosium Hydroxide

Sample Calculations with respect to

Figure 14

$Dy^{3+}_{(aq)}$  calculation (ppm):

$$\begin{aligned} \mu g Dy^{3+}_{(aq)} &= 5.0665 g Dy_2O_{3(s)} \times (1 \times 10^6 \mu g \cdot g^{-1}) \times \left( \frac{\mu g - mol Dy_2O_{3(s)}}{372.97 \mu g Dy_2O_{3(s)}} \right) \\ &\times \left( \frac{2 mol Dy^{3+}_{(aq)}}{mol Dy_2O_{3(s)}} \right) \times \left( \frac{162.50 \mu g Dy^{3+}_{(aq)}}{\mu g - mol Dy^{3+}_{(aq)}} \right) = 4.41 \times 10^6 \mu g Dy^{3+}_{(aq)} \end{aligned}$$

$$ppm Dy^{3+}_{(aq)} = \frac{4.41 \times 10^6 \mu g Dy^{3+}_{(aq)}}{g solvent}$$

The grams of solvent depends on whether the concentration of lanthanide ion is being calculated initially or after  $LiOH_{(aq)}$  addition. The experimentation called for the 500 ml of water with 10 ml of  $HNO_3$  titrated with  $LiOH$  solution with density of  $1.05 g \cdot ml^{-1}$ .

$$g solvent = (500 g H_2O_{(l)} + 13.984 g HNO_{3(aq)}) + (x mL LiOH_{(aq)}) \cdot 1.05 g \cdot ml^{-1} LiOH$$

Initially  $x = 0$  and dysprosium concentration = 8580 ppm

At onset pH  $x = 34.00$  mL and dysprosium concentration = 8022 ppm

$K_{sp}$  calculation at onset pH:

$$Dy^{3+} (mol / L) = 8022 Dy^{3+} (\mu g \cdot g^{-1}) \cdot \left( \frac{1g}{0.001L} \right) \cdot \left( \frac{1 \times 10^{-6} g}{\mu g} \right) \cdot \left( \frac{mol Dy^{3+}}{162.50g} \right) = 4.93 \times 10^{-2} mol \cdot L^{-1}$$
$$= 4.93 \times 10^{-2} mol \cdot L^{-1}$$

$$mol \cdot L^{-1} OH^{-} (aq) = 10^{pH-14} = 10^{6.4-14} = 2.5 \times 10^{-8} mol \cdot L^{-1}$$

$$K_{sp} = [Dy^{3+} (aq) (mol \cdot L^{-1})] \cdot [OH^{-} (aq) (mol \cdot L^{-1})]^3 = 7.8110^{-25}$$

Standard Gibbs free energy calculation for dissolution of lanthanide tri-hydroxide:

$$\Delta G_{298K}^{\circ} (kJ \cdot mol^{-1}) = -RT \ln(K_{sp}) = -8.3145 J \cdot K^{-1} \cdot mol^{-1} \cdot 298.15 K \cdot \ln(7.8110^{-25}) \cdot \frac{1 kJ}{1000 J}$$
$$= 137.6 kJ \cdot mol^{-1}$$

## APPENDIX D. Modeled TGA Solid Dy Precipitate Phase Boundary

Pressure at 1 atm.

$\text{Dy(OH)}_3 = \text{DyO(OH)} + \text{H}_2\text{O}$ or $0.5 \text{ Dy}_2\text{O}_3(3 \cdot \text{H}_2\text{O}) = 0.5 \text{ Dy}_2\text{O}_3(\text{H}_2\text{O}) + \text{H}_2\text{O}$						
Units: T(K), P(atm), Energy(J), Mass(mole)						
*****						
T (K)	Delta H (J)	Delta G (J)	Delta V (l)	Delta S (J /K)	Delta Cp (J)	Keq
*****						
463	86524.8	0.0	0.380E+02	186.834	19.847	1.0132E+00

$\text{DyO(OH)} = 0.5\text{Dy}_2\text{O}_3 + 0.5\text{H}_2\text{O}$ or $0.5 \text{ Dy}_2\text{O}_3(\text{H}_2\text{O}) = 0.5 \text{ Dy}_2\text{O}_3 + 0.5 \text{ H}_2\text{O}$						
Units: T(K), P(atm), Energy(J), Mass(mole)						
*****						
T (K)	Delta H (J)	Delta G (J)	Delta V (l)	Delta S (J /K)	Delta Cp (J)	Keq
*****						
730	48453.1	0.0	0.599E+02	66.428	-22.801	1.0133E+00

## APPENDIX E. Gadolinium Solubility Product Sample Calculation

Sample Calculations with respect to the precipitation experimentation for gadolinia.

$Gd^{3+}$  (aq) calculation (ppm):

$$\begin{aligned} \mu g Gd^{3+}_{(aq)} &= 5.0059 g Gd_2O_{3(s)} \times (1 \times 10^6 \mu g \cdot g^{-1}) \times \left( \frac{\mu g - mol Gd_2O_{3(s)}}{362.5 \mu g Gd_2O_{3(s)}} \right) \\ &\times \left( \frac{2 mol Gd^{3+}_{(aq)}}{mol Gd_2O_{3(s)}} \right) \times \left( \frac{157.25 \mu g Gd^{3+}_{(aq)}}{\mu g - mol Gd^{3+}_{(aq)}} \right) = 4.34 \times 10^6 \mu g Gd^{3+}_{(aq)} \end{aligned}$$

$$ppm Gd^{3+}_{(aq)} = \frac{4.34 \times 10^6 \mu g Gd^{3+}_{(aq)}}{g \text{ solvent}}$$

The grams of solvent depends on whether the concentration of lanthanide ion is being calculated initially or after  $LiOH_{(aq)}$  addition. The experimentation called for the 500 ml of water with 10 ml of  $HNO_3$  titrated with  $LiOH$  solution with density of  $1.05 g \cdot ml^{-1}$ .

$$g \text{ solvent} = (500 g H_2O_{(l)} + 13.984 g HNO_{3(aq)}) + (x mL LiOH_{(aq)}) \cdot 1.05 g \cdot ml^{-1} LiOH$$

Initially  $x = 0$  and gadolinium concentration = 8444 ppm

At onset pH  $x = 36.00$  mL and gadolinium concentration = 7866 ppm

$K_{sp}$  calculation at onset pH:

$$\begin{aligned} Gd^{3+} (mol / L) &= 7866 Gd^{3+} (\mu g \cdot g^{-1}) \cdot \left( \frac{1g}{0.001L} \right) \cdot \left( \frac{1 \times 10^{-6} g}{\mu g} \right) \cdot \left( \frac{mol Gd^{3+}}{157.25g} \right) = 5.002^{-2} mol \cdot L^{-1} \\ &= 5.002 \times 10^{-2} mol \cdot L^{-1} \end{aligned}$$

$$mol \cdot L^{-1} OH^{-}_{(aq)} = 10^{pH-14} = 10^{6.96-14} = 9.1 \times 10^{-8} mol \cdot L^{-1}$$

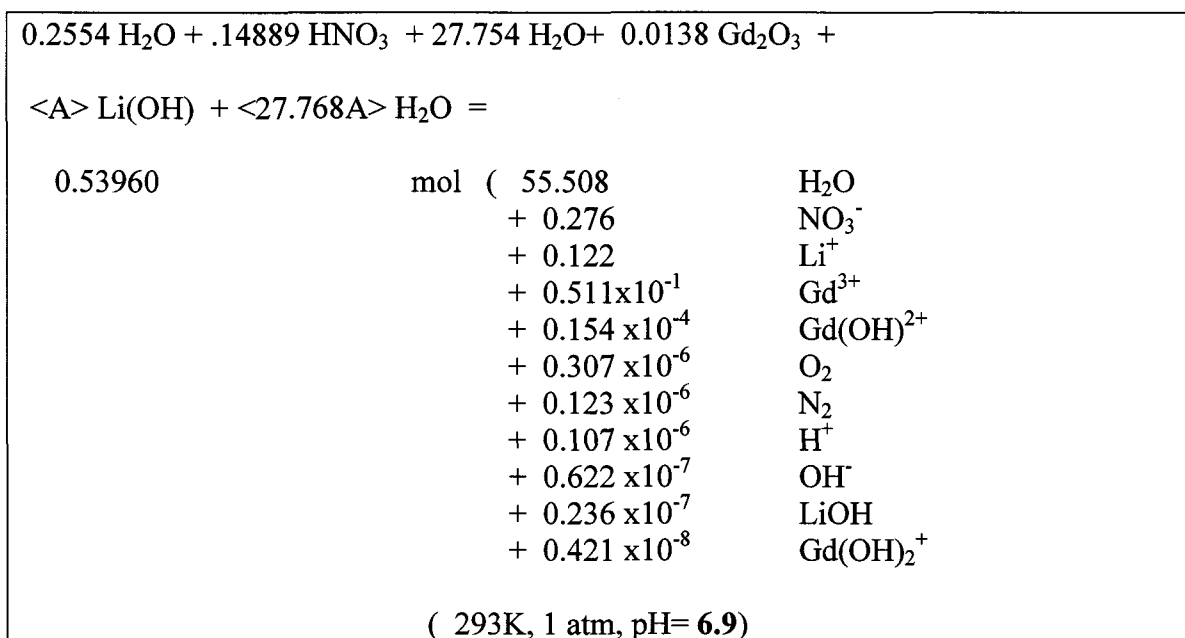
$$K_{sp} = [Gd^{3+}_{(aq)} (mol \cdot L^{-1})] \cdot [OH^{-}_{(aq)} (mol \cdot L^{-1})]^3 = 3.79 \times 10^{-23}$$

Standard Gibbs free energy calculation for dissolution of lanthanide tri-hydroxide:

$$\begin{aligned}\Delta G_{298K}^{\circ} (kJ \cdot mol^{-1}) &= -RT \ln(K_{sp}) = -8.3145 J \cdot K^{-1} \cdot mol^{-1} \cdot 298.15 K \cdot \ln(3.79 \times 10^{-23}) \cdot \frac{1 kJ}{1000 J} \\ &= 128 kJ \cdot mol^{-1}\end{aligned}$$

## APPENDIX F. Thermodynamic Computations of Gadolinium

### Thermodynamic Modelling of Gadolinium Hydroxide Solubility Product



### Modeled TGA Gadolinium Solid Precipitate Phase Boundary Calculation

Gd(OH)<sub>3</sub> = GdOOH + H<sub>2</sub>O      or      0.5Gd<sub>2</sub>O<sub>3</sub>(3·H<sub>2</sub>O) = 0.5Gd<sub>2</sub>O<sub>3</sub>(H<sub>2</sub>O) + H<sub>2</sub>O

(T,P,S1<-) (T,P,S1<-) (T,P,G1)

Units: T(K), P(atm), Energy(J), Mass(mole)

\*\*\*\*\*

T	P	Delta H	Delta G	Delta V	Delta S	Delta Cp
(K)	(atm)	(J)	(J)	(l)	(J /K)	(J)
473	1	95735.4	0.0	0.389E+02	202.061	43.858

\*\*\*\*\*

GdOOH = 0.5Gd<sub>2</sub>O<sub>3</sub> + 0.5H<sub>2</sub>O      or      0.5Gd<sub>2</sub>O<sub>3</sub>(H<sub>2</sub>O) = 0.5Gd<sub>2</sub>O<sub>3</sub> + 0.5H<sub>2</sub>O

(T,P,S1<-) (T,P,S1) (T,P,G1)

Units: T(K), P(atm), Energy(J), Mass(mole)

\*\*\*\*\*

T	P	Delta H	Delta G	Delta V	Delta S	Delta Cp
(K)	(atm)	(J)	(J)	(l)	(J /K)	(J)
813	1	23432.6	0.0	0.334E+02	28.821	-18.24

\*\*\*\*\*

## APPENDIX G. Thermodynamic Data of Species

### Thermodynamic Data for Dysprosium Compounds

Formula: Dy  
 Name: Dysprosium  
 Data stored in calories at a total pressure of 1 atmosphere  
 Formula Weight: 162.500

$$C_p(T) = \sum_{i=1}^8 C(i) X T^{P(i)} \quad (\text{J/K})$$

\*\*\*\*\*

PHASE	DH(298) (J)	S(298) (J/K)	C(i)	P(i)	C(i)	P(i)
S1	0.00	74.893600	28.2378160	0.0	-.410032000E-03	1.0
S1	-34.98	74.786399	22.9408720 340159.200	0.0 -2.0	0.757722400E-02	1.0
S1	-3389.67	66.170638	18.9116800 3358915.20	0.0 -2.0	-.371539200E-02 0.132047040E-04	1.0 2.0
S2	12590.94	83.812241	28.0328000	0.0		
L1	-6632.60	52.527220	49.9151200	0.0		
G1	290369.60	196.522480	20.7944800	0.0		

Formula: Dy2O3

Name: Dysprosium sesquioxide

Data stored in calories at a total pressure of 1 atmosphere

Formula Weight: 372.998

$$C_p(T) = \sum_{i=1}^8 C(i) X T^{P(i)} \quad (\text{J/K})$$

```
*****
PHASE  DH(298)    S(298)                C(i)  P(i)    C(i)    P(i)
        (J)      (J/K)
*****
S1     -1863101.99  149.799999           128.444616  0.0  0.192505840E-01  1.0
        -1672763.20 -2.0
L1     -1796752.12  174.903999           128.444616  0.0  0.192505840E-01  1.0
        -1672763.20 -2.0
*****
```

Formula: Dy[3+]

Name: Dysprosium Tripositive Ion

Data stored in calories at a total pressure of 1 atmosphere

Formula Weight: 162.500

$$C_p(T) = \sum_{i=1}^8 C(i) X T^{P(i)} \quad (\text{J/K})$$

```
*****
PHASE  DH(298)    S(298)                C(i)  P(i)    C(i)    P(i)
        (J)      (J/K)
*****
Aq1    -698728.00  -230.956800           20.920000  0.0
*****
```

Formula: Dy(O\*H)[2+]

Data stored in Joules at a total pressure of 1 atmosphere

Formula Weight: 179.507

$$C_p(T) = \sum_{i=1}^8 C(i) X T^{P(i)} \quad (\text{J/K})$$

```
*****
PHASE  DH(298)    S(298)                C(i)  P(i)    C(i)    P(i)
        (J)      (J/K)
*****
Aq1    -920000.00  -130.000000           0.100000000E-05  0.0
*****
```



Formula: Dy(O\*H)2[+]

Data stored in Joules at a total pressure of 1 atmosphere

Formula Weight: 196.515

$$C_p(T) = \sum_{i=1}^8 C(i) X T^{P(i)} \quad (\text{J/K})$$

```
*****
PHASE  DH(298)    S(298)          C(i)    P(i)    C(i)    P(i)
        (J)      (J/K)
*****
Aq1    -1150000.00 -30.000000     0.100000000E-05  0.0
```

Formula: Dy(O\*H)3

Name: Dysprosium Trihydroxide

Data stored in Joules at a total pressure of 1 atmosphere

Formula Weight: 213.522

$$C_p(T) = \sum_{i=1}^8 C(i) X T^{P(i)} \quad (\text{J/K})$$

```
*****
PHASE  DH(298)    S(298)          C(i)    P(i)    C(i)    P(i)
        (J)      (J/K)
*****
S1     -1409200.86  130.300000     115.000000  0.0
Aq1    -1395000.00  70.000000     0.100000000E-05  0.0
```

Formula: Dy(O\*H)4[-]

Data stored in Joules at a total pressure of 1 atmosphere

Formula Weight: 230.529

$$C_p(T) = \sum_{i=1}^8 C(i) X T^{P(i)} \quad (\text{J/K})$$

```
*****
PHASE  DH(298)    S(298)          C(i)    P(i)    C(i)    P(i)
        (J)      (J/K)
*****
Aq1    -1590000.00  170.000000     0.100000000E-05  0.0
```

Formula: Dy\*O(O\*H)

Name: Dysprosium oxide monohydrate

Data stored in Joules at a total pressure of 1 atmosphere

Formula Weight: 195.507

$$C_p(T) = \sum_{i=1}^8 C(i) X T^{P(i)} \quad (\text{J/K})$$

\*\*\*\*\*

PHASE	DH(298) (J)	S(298) (J/K)	C(i)	P(i)	C(i)	P(i)
S1	-1084000.00	120.000000	100.000000	0.0		

\*\*\*\*\*

Thermodynamic Data for Lithium Hydroxide Compound

Formula: Li\*O\*H

Name: Lithium Hydroxide

Data stored in Joules at a total pressure of 1 bar

Formula Weight: 23.948

$$C_p(T) = \sum_{i=1}^8 C(i) X T^{P(i)} \quad (\text{J/K})$$

\*\*\*\*\*

PHASE	DH(298) (J)	S(298) (J/K)	C(i)	P(i)	C(i)	P(i)
S1	-484926.00	42.821000	51.1918067	0.0	0.330869064E-01	1.0
			-1020597.21	-2.0		
S1	-495373.94	19.823822	87.0860000	0.0		
L1	-463964.00	70.764745	51.1918067	0.0	0.330869064E-01	1.0
			-1020597.21	-2.0		
L1	-474411.94	47.767567	87.0860000	0.0		
G1	-234304.00	210.549556	51.0180594	0.0	0.314355131E-02	1.0
			-525058.664	-2.0	0.687910986E-06	2.0
G1	-238714.15	198.984478	57.9406866	0.0	10248073.4	-2.0
			-38234.4865	-1.0	770.256378	-0.5
Aq1	-510300.00	7.100000	-321.473000	0.0	0.402890000	1.0
			15334800.0	-2.0		

\*\*\*\*\*

Thermodynamic Data for Gadolinium Compounds

Formula: Gd  
 Name: Gadolinium  
 Data stored in calories at a total pressure of 1 atmosphere  
 Formula Weight: 157.250

$$C_p(T) = \sum_{i=1}^8 C(i) \times T^{P(i)} \quad (\text{J/K})$$

\*\*\*\*\*

PHASE	DH(298) (J)	S(298) (J/K)	C(i)	P(i)	C(i)	P(i)
S1	0.00	67.948160	-22.8488240 3322514.40	0.0 -2.0	0.755965120E-01	1.0
S1	450.34	69.322094	23.9366640	0.0	0.861904000E-02	1.0
S1	1659.10	71.686294	19.9283920	0.0	0.121963600E-01	1.0
S2	9042.59	75.617768	28.2838400	0.0		
L1	7682.28	67.141458	37.1539200	0.0		
G1	397480.00	194.204544	27.5474560	0.0		

Formula: Gd<sub>2</sub>O<sub>3</sub>  
 Name: Gadolinium sesquioxide  
 Data stored in calories at a total pressure of 1 atmosphere  
 Formula Weight: 362.498

$$C_p(T) = \sum_{i=1}^8 C(i) \times T^{P(i)} \quad (\text{J/K})$$

\*\*\*\*\*

PHASE	DH(298) (J)	S(298) (J/K)	C(i)	P(i)	C(i)	P(i)
S1	-1819621.99	156.900000	114.490976 -1082400.80	0.0 -2.0	0.144682720E-01	1.0
L1	-1752267.99	182.004000	114.490976 -1082400.80	0.0 -2.0	0.144682720E-01	1.0

Formula: Gd[3+]  
 Name: Gadolinium Tripositive Ion  
 Data stored in calories at a total pressure of 1 atmosphere  
 Formula Weight: 157.250

$$C_p(T) = \sum_{i=1}^8 C(i) X T^{P(i)} \quad (J/K)$$

```
*****
PHASE  DH(298)    S(298)          C(i)    P(i)    C(i)    P(i)
        (J)      (J/K)
*****
Aq1    -684502.43 -205.852787    88.8305040  0.0  -418215904  1.0
                   1438877.60  -2.0
*****
```

Formula: Gd(O\*H)[2+]  
 Data stored in Joules at a total pressure of 1 atmosphere  
 Formula Weight: 174.257

$$C_p(T) = \sum_{i=1}^8 C(i) X T^{P(i)} \quad (J/K)$$

```
*****
PHASE  DH(298)    S(298)          C(i)    P(i)    C(i)    P(i)
        (J)      (J/K)
*****
Aq1    -905774.00 -105.000000    0.100000000E-05 0.0
*****
```

Formula: Gd(O\*H)2[+]  
 Data stored in Joules at a total pressure of 1 atmosphere  
 Formula Weight: 191.265

$$C_p(T) = \sum_{i=1}^8 C(i) X T^{P(i)} \quad (J/K)$$

```
*****
PHASE  DH(298)    S(298)          C(i)    P(i)    C(i)    P(i)
        (J)      (J/K)
*****
Aq1    -1127046.00 -5.000000    0.100000000E-05 0.0
*****
```

Formula: Gd(O\*H)3

Data stored in Joules at a total pressure of 1 atmosphere

Formula Weight: 208.272

$$C_p(T) = \sum_{i=1}^8 C(i) X T^{P(i)} \quad (\text{J/K})$$

\*\*\*\*\*

PHASE	DH(298) (J)	S(298) (J/K)	C(i)	P(i)	C(i)	P(i)
-------	----------------	-----------------	------	------	------	------

\*\*\*\*\*

S1	-1396000.00	126.600000	91.0950000	0.0		
----	-------------	------------	------------	-----	--	--

Aq1	-1348318.00	95.000000	0.100000000E-05	0.0		
-----	-------------	-----------	-----------------	-----	--	--

Formula: Gd(O\*H)4[-]

Data stored in Joules at a total pressure of 1 atmosphere

Formula Weight: 225.279

$$C_p(T) = \sum_{i=1}^8 C(i) X T^{P(i)} \quad (\text{J/K})$$

\*\*\*\*\*

PHASE	DH(298) (J)	S(298) (J/K)	C(i)	P(i)	C(i)	P(i)
-------	----------------	-----------------	------	------	------	------

\*\*\*\*\*

Aq1	-1569590.00	195.000000	0.100000000E-05	0.0		
-----	-------------	------------	-----------------	-----	--	--

## **CURRICULUM VITAE**

## CURRICULUM VITAE

Adam Steven Blackier

Born: Quispamsis  
New Brunswick, Canada  
June 22<sup>nd</sup> 1985

### **Education:**

- 2003: New Brunswick High School Diploma, Kennebecasis Valley High School, Quispamsis, New Brunswick, Canada.
- 2003-2004: Commenced studies in biological sciences at the University of New Brunswick, Fredericton, New Brunswick, Canada.
- 2004-2008: Received a degree of Bachelor of Engineering, Chemical Engineering, First Class Distinction, Royal Military College of Canada, Kingston, Ontario, Canada.
- 2008-2009: Graduate Studies in the field of Nuclear Engineering, Kingston, Ontario, Canada.

### **Canadian Forces:**

- 2003: Sworn into the Canadian Forces, Saint John, New Brunswick, Canada.
- 2003: Completed training in CFB Shilo, Manitoba, Canada.
- 2004-2005: Basic Officer Training Course, Saint Jean Sur Richelieu, Quebec, Canada.
- 2006: Common Army Phase Training, CFB Gagetown, New Brunswick, Canada.
- 2007: Basic Engineer Officer Course, CFB Gagetown, New Brunswick, Canada.
- 2008: Commissioned as a Second Lieutenant, Royal Military College of Canada, Kingston, Ontario, Canada.